A Silicon Photonic Circuit for Optical Trapping and Characterization of Single Nanoparticles

by

Seyed Hamed Mirsadeghi

B. Physics, Shahid Beheshti University, 2007

M.Sc. Physics, The University of British Columbia, 2010

A THESIS SUBMITTED IN PARTIAL FULFILLMENT
OF THE REQUIREMENTS FOR THE DEGREE OF

Doctor of Philosophy

in

THE FACULTY OF GRADUATE AND POSTDOCTORAL STUDIES

(Physics)

The University Of British Columbia

(Vancouver)

April 2017

Abstract

In this thesis, two slightly different silicon-on-insulator (Silicon-on-Insulator (SOI)) planar photonic integrated circuits for optically trapping and characterizing single nanoparticles are designed, fabricated, and fully characterized. These symmetric (input/output) structures are formed by etching two dimensional patterns through a 220 nm thick silicon slab atop a micrometer thick layer of silicon dioxide, and are operated in a fluidic cell at wavelengths of $\approx 1.55\ \mu$m. Each consist of two grating couplers, two parabolic tapered waveguides, two single mode ridge waveguides, two photonic crystal waveguides and a single photonic crystal slot (PCS) microcavity, designed using a Finite Difference Time Domain (FDTD) electromagnetic simulation tool. The circuits are designed to concentrate continuous wave laser light incident on the input grating coupler to a small volume within the fluidic channel of the microcavity in order to achieve a high electric field intensity gradient capable of attracting and trapping nanoparticles from the solution via optical gradient forces.

The fabricated PCS cavities exhibit Q factors > 7500 and resonant transmissions as high as $T = 6\%$, when operated in hexane and without undercutting the cavities. Due to fabrication imperfections, the cavity Q and peak transmission values were not as high as simulation predicted, nevertheless, these robust, devices were successfully used to optically trap single sub-50 nm Au nanospheres and nanorods with < 0.5 mW of laser power. Furthermore, it was found that while the particles were trapped, the transmitted laser intensity varied randomly in time, providing a simple means of characterizing the Brownian motion of the particle in the trap. The intensity variation is caused by the backaction of the dielectric object on the cavity resonance, the magnitude of which depends on the real part of the

trapped particle's polarizability tensor, and its position in the cavity. By exploiting this cavity-nanoparticle interaction, we developed a self-consistent analysis of the transmission signal of circuits that enabled us to determine the size and anisotropy of the trapped nanoparticles without any direct imaging, with nanometer sensitivity.

Preface

The initial design of the research program was primarily set by my research supervisor, Jeff F. Young. My role was primarily implementation and development of the experimental setups, measurements, modelling, and analysis used to implement the research program. Three publications arising entirely from the work within this thesis are as follows:

- S. Hamed Mirsadeghi, Ellen Schelew, and Jeff F. Young. Photonic crystal slot-microcavity circuit implemented in silicon-on-insulator: High q operation in solvent without undercutting. Applied Physics Letters, 102(13):131115, 2013 [1]

- S. H. Mirsadeghi, E. Schelew, and J. F. Young. Compact and efficient silicon nanowire to slot waveguide coupler. In 2013 13th International Conference on Numerical Simulation of Optoelectronic Devices (NUSOD), pages 3132, 19-22 Aug. 2013 [2].

- S. Hamed Mirsadeghi and Jeff F. Young. Ultrasensitive diagnostic analysis of Au nanoparticles optically trapped in silicon photonic circuits at submilliwatt powers. Nano Lett., 14(9):50045009, September 2014 [3]

The simulation and modelling results in [1, 2] are presented in Chapter 2. And the measurements and characterization in [1] is incorporated in Chapter 3. My role in these two publications was FDTD modelling, designing devices, creating their layout for fabrication, chip preparation, experimental measurement, analysis of the results, and majority of manuscript preparation and review of them. The original transmission set-up was build by Ellen N. Schelew and further development of the

data acquisition and device holding system were done by me. Ellen N. Schelew was also the main writer of the manuscript in [2]. The chip fabrication was done in collaboration with Dr. Lukas Chrostowski and University of Washington Microfabrication Facility, a member of the NSF National Nanotechnology Infrastructure Network [4]. Much of the text of these two publications are directly included into this thesis.

The simulation, measurement and modelling results in [3] are all presented in Chapter 4. My role in this publication was FDTD modelling, designing devices, creating their layout for fabrication, chip and Au solution preparation, experimental measurement, and analysis of the results. I also worked with Jeff F. Young in developing the backaction model for optical trapping in photonic crystal slot cavities, manuscript preparation, and review of it. Much of the text in this publication is also directly included into this thesis.

The simulation, measurement and modelling that are presented in Chapter 5 have not been published yet. My role in this chapter was FDTD modelling, designing devices, creating their layout for fabrication, majority of chip and Au solution preparation, experimental measurement, and analysis of the results. I also worked with Jeff F. Young in developing the more general version of backaction model for anisotropic particle trapping in photonic crystal slot cavities. Jonathan Massey-Allard also contributed in chip and Au solution preparation, Au nanorod optical trapping experiments, SEM/AFM imaging of the chips after trapping experiments, and preparing the manuscript for publishing the results of this chapter.

Table of Contents

List of Tables

List of Figures

Glossary

BOX Buried Oxide

C.O.M Center Of Mass

CMOS Complementary Metal Oxide Semiconductor

CW Continuous Wave

DI Deionized Water

FDTD Finite Difference Time Domain

FEM Finite Element Method

FWHM Full Width at Half Maximum

GPIB General Purpose Interface Bus

LPP Localized Plasmon Polaritons

MST Maxwell Stress Tensor

PAE Permanent Attachment Event

PBG Photonic Band Gap

PC Photonic Crystal

PCS Photonic Crystal Slot

PLC Photonic Lightwave Circuits

SEM Scanning Electron Microscope

SOI Silicon-on-Insulator

TE Transverse Electric

TIR Total Internal Reflection

TM Transverse Magnetic

TTES Temporary Trapping Events

Acknowledgments

First and foremost, I would like to express my gratitude to my supervisor, Dr. Jeff Young for his inspiration, guidance and continuous support during my PhD study. My special thanks to Ellen Schelew, Jonathan Massey-Allard, Dr. Charles Foell for their support throughout this work. They have been a source of friendships as well as good advice and collaboration. It was a pleasure working with you! Thanks to the rest of the Nanolab members for their help and good company during my stay in the lab, Dr. George Rieger, Dr. Mohsen Keshavarz Akhlaghi and Dr. Mario Beaudoin.

Lastly, I would like to thank my family for all their love and encouragement. For my parents, my sister and most of all for my loving, patient wife, who supported me in all my pursuits. Thank you!

Chapter 1

Introduction

1.1 Motivation

The work described in this thesis demonstrates how modern nanofabrication techniques can be used to engineer the strength of light-matter interactions to optically trap and confine single sub-50 nm dimension nanoparticles with sub-micron precision, using less than 1 mW of continuous wave laser excitation. The key challenge - routing laser radiation of a specific wavelength into a nanophotonic cavity with dimensions less than a cubic wavelength, and keeping it confined for $\sim 10,000$ optical cycles - was achieved using textured silicon planar waveguides that were immersed in a solvent bath containing a dispersion of Au nanoparticles. The basic design concepts are common to related structures designed to enhance light-matter interactions for nonlinear optics [23], single photon sources [24], and sensing applications [25–28]. The results add to a growing body of work that aims to optically manipulate, detect, and/or characterize nanoparticles in solution using the strong "*dipole*" forces exerted by confined light on small dielectric particles [3, 12, 25, 29].

The project was originally motivated by wanting to use such structures to optically trap and then permanently attach single nanoscale semiconducting nanocrystals, or "*quantum dots*" at the antinode of high quality factor cavities formed in silicon photonic circuits [30]. These quantum dots can act effectively as quantum emitters, and when resonant with microcavity modes, they can be used to produce

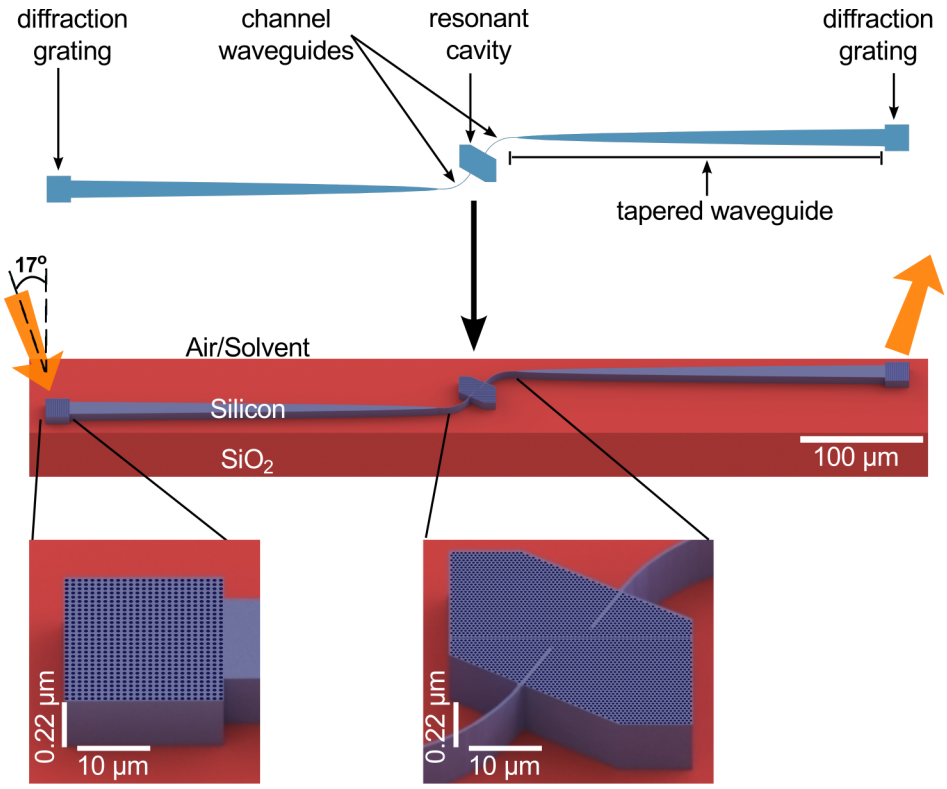

Figure 1.1: Layout of a full device designed and fabricated in this work for optical trapping and sensing experiments. It includes the diffraction grating couplers, cavity and waveguides all patterned in a 220 nm silicon slab sitting on top of SiO_2 substrate (in red). The gratings, which consist of a 2D lattice of holes etched in silicon, are separated by 680 microns. The input/output light is injected/collected at a 17° angle to the normal to grating plane. The vertical scale bar is different than the in-plane scale bar for better visibility.

non-classical, single photon sources [31–33], or as mediators of nonlinear optical processes at the single photon level, both of which are key ingredients for optically-based quantum information processing. To be resonant with silicon-based microcavities, Pb-based nanocrystals must be on the order of ~ 5 nm in diameter. The circuits described in this thesis are not currently capable of trapping such small particles, but only small improvements are necessary to realize this original goal.

The structures used to achieve this level of confinement of infrared laser light with wavelengths $\sim 1.5\ \mu$m are made by two dimensionally (2D) patterning ~ 200 nm thick planar silicon slabs supported on a thick silicon dioxide cladding layer (see Fig.1.1). The high refractive index of silicon ($n_{Si} = 3.45$) compared to silica ($n_{SiO2} = 1.45$) below, and air or solvent above ($n = 1 - 1.37$), means that light can propagate in 2D, without loss, via bound, planar waveguide modes, due to total internal reflection. 2D patterns are defined in mask layers using electron beam lithography, and transferred to the silicon slab by chemically etching through the entire slab, as shown in Fig.1.2. The patterns are designed to i) couple light from free space into and out of the bound waveguide modes via diffraction gratings, ii) further confine the bound modes to propagate along distinct paths within the slab via channel waveguides (effectively integrated optical fibers), and iii) define ultra-small, ultra-high quality factor 3D resonant cavities that are efficiently coupled to the waveguides.

Silicon was chosen as the base waveguide material because of its high refractive index, but also because many industries are rapidly leveraging decades of silicon processing expertise to develop integrated photonic/electronic chips for classical telecommunication applications [34–37]. The starting SOI wafers are relatively inexpensive [37, 38], there is a solid base of advanced, silicon-specific photonic circuit design tools [38], and several optical and electron-beam processing "*foundries*" are readily accessible to researchers [38, 39]. Successful integration of multiple optical components such as waveguides, resonators and filters, in the form of planar photonic integrated circuits, have been already demonstrated on silicon wafers [1, 39, 40] and progress is constantly being made toward replacing optical components with equivalent photonic nanostructures.

The novelty of this thesis work has to do with the design of the 3D microcavities and how they couple to previously designed channel waveguides and grat-

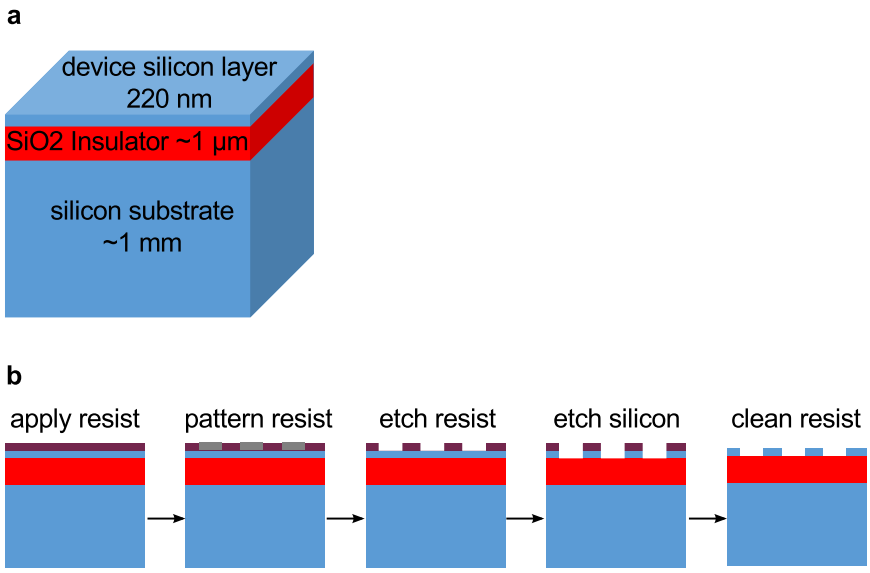

Figure 1.2: (a) Typical silicon-on-insulator (SOI) dimensions used for fabricating photonic integrated circuits. (b) Example fabrication process for creating pattern on silicon slab. Additional functionality may be achieved by lithographic integration of metal contacts, ion doping, and deposition of other materials [5].

ing couplers. While much silicon photonic work utilizes ring [15] or disk resonators [16] to confine light with high quality factors (Q: the number of optical cycles that light remains trapped in the cavities), the need for both high Q, *and* low mode volumes, motivated the use of microcavities based on 2D, in-plane Photonic Crystal (PC) concepts [1, 3].

These novel photonic circuits were successfully used to optically trap individual Au nanospheres and nanorods with dimensions < 50 nm using less than 1 mW of Continuous Wave (CW) laser power [3]. These particles perturb the dielectric environment of the microcavity significantly, shifting the resonant frequency by up to a few linewidths. This "*backaction*" leads to a nanoparticle-position dependent transmission of the excitation laser, and a corresponding change of the power coupled into the cavity mode. A detailed model of the optical forces and torques operating on the trapped nanoparticles, including the backaction, was developed and used to extract the size and shape of the trapped nanoparticles with nanometer

sensitivity, using only the variation in transmitted light intensity associated with the Brownian motion of the particles in the cavity. It is believed that this structure and analysis can be of great interest in not only the physics community but also to the biology and medicine communities for the study of single biological particles.

The rest of this chapter introduces different concepts that are exploited to conduct this research.

1.2 Silicon Photonic Integrated Circuits

Communications technology was revolutionized when optical fibers and semiconductor lasers enabled transmission of information using coded optical signals rather than electrical currents. Data processing and transmission are therefore currently done on two separate platforms: microelectronic Complementary Metal Oxide Semiconductor (CMOS) chips and optical fiber networks, respectively. Many optical network components (e.g. lenses, filters, beam splitters, etc.) have gradually shrunk in size, but until very recently, they have remained largely stand-alone, bulk elements. In late 80s, the idea of integrating multiple optical components on a small silicon chip was suggested for the first time [34–37]. The motivation was to replace separate bulky optical components with miniature optical chips that still output electrical signals to be processed using CMOS electronics. Silicon attracts most attention in this field due to its compatibility with the mature silicon integrated circuit manufacturing enterprise, having the lowest cost per unit area, the highest crystal quality of any semiconductor material, small optical absorption in near-infrared (IR), high thermal conductivity, high optical damage threshold, and high third-order optical nonlinearities [38]. Availability in the form of high quality SOI wafers is another reason for choosing silicon as an ideal platform for creating planar waveguide circuits [38]. The ultimate goal of much of the current silicon photonic circuit research and development is to successfully realize a wide range of photonic circuit elements in silicon at a relatively low cost that perform both switching and routing tasks without a need for signal conversion between optical and electrical elements [22].

There exists a huge body of work behind the development of the two fundamental building blocks of SOI-based photonic circuits: grating input/output cou-

plers, and single Transverse Electric (TE) polarized mode "*photonic wires*" [41–53]. Fig. 1.3 shows a schematic of a generic photonic circuit. Grating couplers are all essentially diffraction gratings designed so that light incident from a focused laser or an optical fiber near-normally incident on the wafer will diffract into the plane of the silicon slab where it will be guided due to Total Internal Reflection (TIR). The active area of the grating couplers is therefore on the order of 10 μm^2, and they typically incorporate some adiabatic transition to couple the diffracted beam into the single mode channel waveguides that have been optimized to have cross sections $\sim$ 200 nm $\times$500 nm (for wavelengths around 1550 nm), as shown in Fig.1.1. Etching and chemical polishing techniques have been optimized to minimize side-wall roughness on the etched silicon surfaces that define the patterned features, to the extent that losses as low as $\sim$ 0.8 dB/cm through these single mode waveguides can be achieved [51, 53, 54].

In the current work, the key operational element connected to the channel input and output waveguides is a high Q, small mode volume microcavity. Very high Q (up to several million) microcavities have been made in photonic circuits by etching smooth-edged disks or ring waveguides (see Fig. 1.10 in Section 1.4.2), with typical radii of $\sim$ 10 μm. While some optical trapping of particles has been demonstrated using such cavities [14–17], the fact that the high intensity region of the resonant cavity modes lies within the silicon means that the particles only interact with the confined light field via the evanescent fields that penetrate the solvent overlayer. Furthermore, the mode volume V of these type of resonators is typically several cubic wavelengths. These factors translate into the need for relatively high input laser powers ($\sim$ 10 mW) to trap even large (500 nm) dielectric particles [14–17].

To reduce the required power, the present work employed microcavities defined by introducing defect states within quasi-2D photonic crystals etched into the silicon, as described in the following section.

1.3 Photonic Crystal Nanostructures

As mentioned above, TIR within the 2D device layer of SOI circuits reduces the size of optical components significantly compared with bulk counterparts. It is also

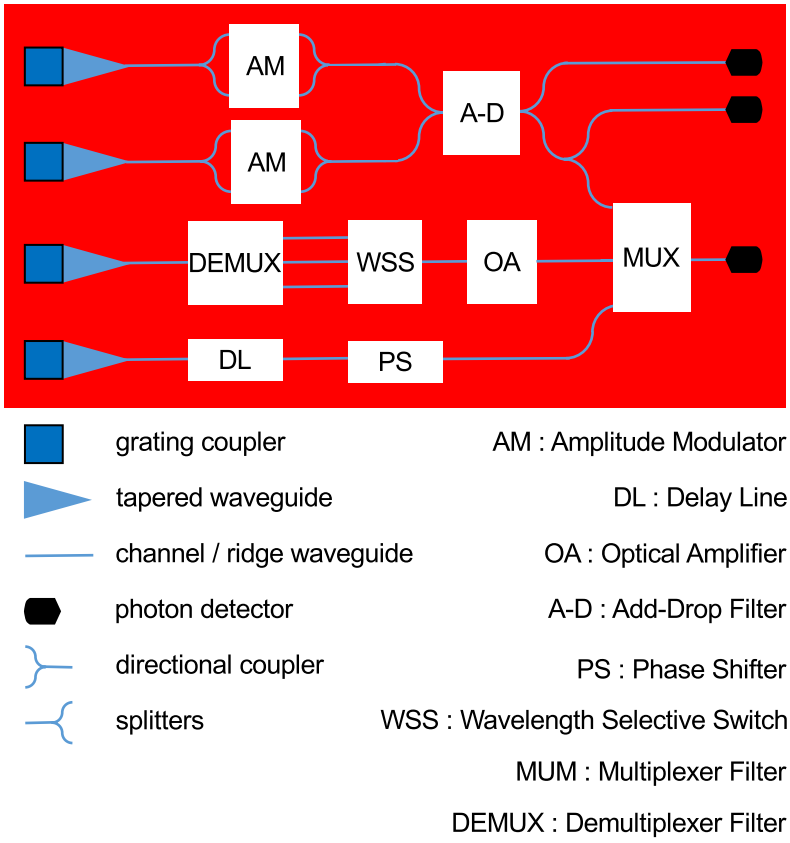

Figure 1.3: (a) Schematic of a generic SOI photonic integrated circuit consisting of different active and passive photonic elements such as grating couplers, waveguides, splitters, filters, switches, etc. The minimum size of splitters, is limited by how tightly channel waveguides may be bent before break down of TIR, which is dictated by relative indices of refraction of the waveguide and surrounding cladding.

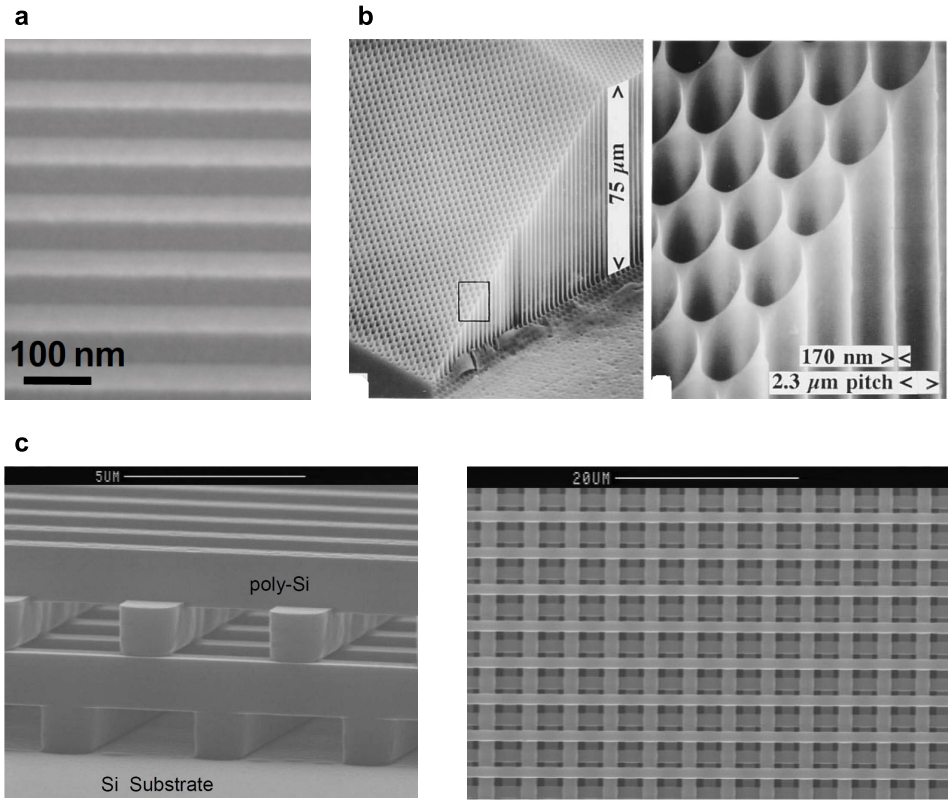

Figure 1.4: Example structures taken from the literature (not work done as part of this thesis); (a) Scanning Electron Microscope (SEM) image of one-dimensional (1D) PC made of successive layers of AlInN (darker) and GaN (brighter) (reprinted from [6]). (b) SEM image of a two-dimensional (2D) PC made of macroporous silicon lattice (reprinted from [7]). (c) SEM micrographs of a three-dimensional (3D) photonic crystal. Left image is the top view of a completed four-layer structure and the right image is the cross-sectional view of the same 3D photonic crystal. The rods are made of polycrystalline silicon (reprinted from [8]).

responsible for in-plane light confinement in channel waveguides (typically with a few hundred nanometers width and vertical walls), which are effectively optical fibers that route light in planar photonic integrate circuits.

In the 80s, a different and more powerful photon confinement mechanism was developed based on the Photonic Band Gap (PBG) concept that was first introduced separately by Yablonovich [55] and John [56]. Confinement based on the PBG effect allows for even further light confinement and therefore optical device miniaturization. John and Yablonovich showed that by creating multidimensional periodic structures (Fig. 1.4) with periods on the order of an optical wavelength and sufficiently high refractive index contrast, it is possible to artificially create a band of frequencies (PBG) within which there are no propagating solutions to the Maxwell's equations (i.e. photonic density of states of zero). These so-called PC structures are the photonic analog of an atomic lattice for electrons, which instead of obeying Schrödinger's equations, follow Maxwell's wave equations. Like electrons in atomic lattices, photons in PCs exhibit band structure and depending on the lattice type and scattering properties of the unit cell, these band structures may or may not exhibit full band gaps; a range of optical frequencies for which light propagation is prohibited in all directions for all polarizations (Fig. 1.5). By modifying the structure of PCs (e.g. their periods, refractive indices, shapes etc.) and therefore, their band-structures, it is possible to engineer the photonic density of states, which leads to various applications from controlling of spontaneous emission through the Purcell effect [55, 57] to enhancing laser efficiencies [58–60], guiding light through sharp bends [61] and propagation speed of light for nonlinear optics [62].

Complete PBG for all propagation directions can only be realized in 3D PCs with sufficient index contrast and lattice structure. For other periodic structures (e.g. 1D, 2D or "*2D planar*"), only *quasi* PBG can exist for some specific propagation direction and polarization. For instance, in Fig. 1.5, for a 2D planar PC lattice (called planar because the holes have finite depth), one can at best only achieve a quasi-PBG for TE modes propagating in the *xy* plane. Thus, although in 1D and 2D PC structures, there is no complete PBG, one can still can use these structures as a very effective means of in-plane light confinement of radiation modes with specific polarization properties.

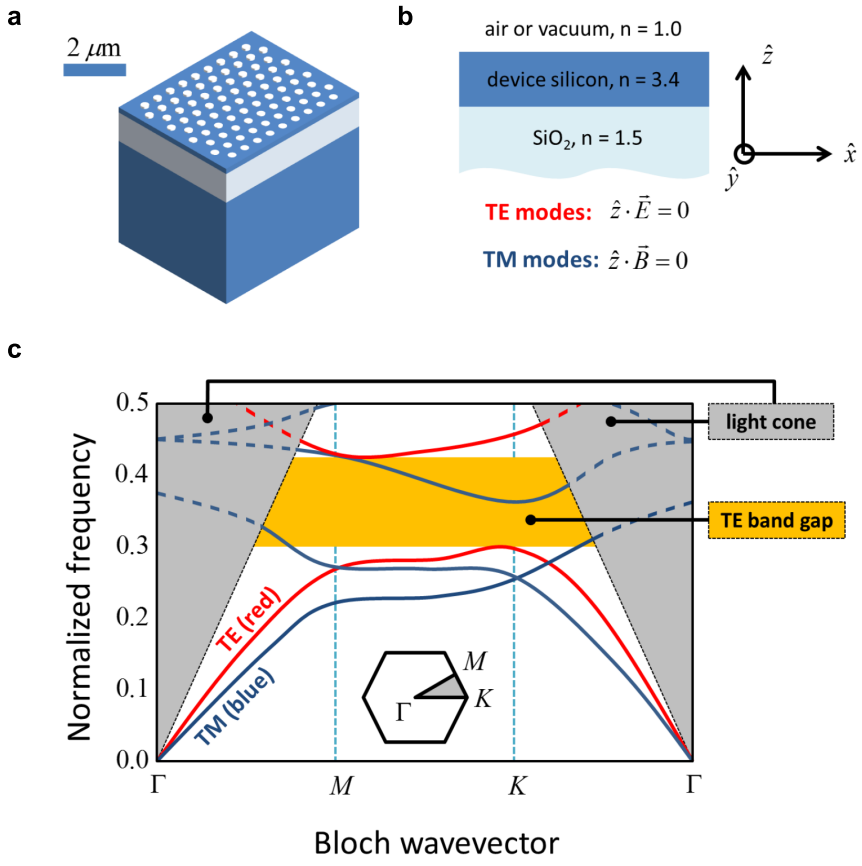

Figure 1.5: [(a)-(b)] Schematic of a 2D planar hexagonal lattice PC structure in a SOI photonic circuit with two types of propagating modes: TE (with only in-plane electric field polarization) and TM (with only in-plane magnetic field polarization). (c) Example photonic band structure for the 2D planar PC above the substrate in (a) (reprinted from [5]). The gray light-cones show the area above substrate light-line, where the TIR fails and leads to coupling of the PC modes to continuum modes and therefore to intrinsic out-of-plane diffraction losses in the PC region.

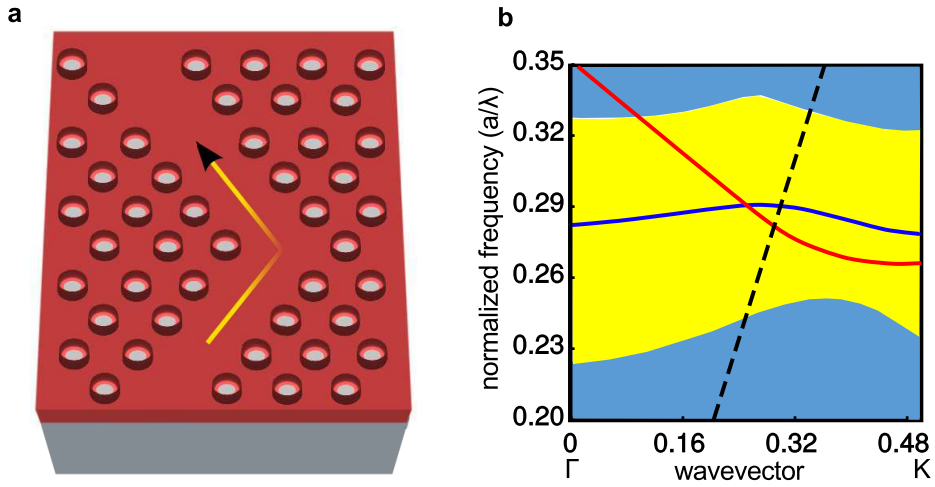

Figure 1.6: (a) Schematic of a line defect (also known as W1) PC waveguide which is created by removing a row of holes in a hexagonal lattice of holes. (b) Example band structure of a W1 waveguide showing two guided TE modes (the red has even symmetry and the blue has odd symmetry) in the projected bulk PC bandgap (yellow region).

Quasi-2D PC like the one shown in Fig. 1.5 can be used to confine light more strongly than TIR alone by introducing appropriate defects within the 2D PC uniform host crystal. Fig. 1.6 illustrates how, by leaving out a row of holes in an otherwise uniform hexagonal PC lattice, one can form 1D connected waveguides with effective bend-radii on the order of the lattice constant. There are variety of ways for introducing a linear defect into a crystal, and therefore a variety of guided modes. The only requirement is that the structure has discrete translational symmetry in the waveguiding direction [63]. By tuning the size/location of holes in the bend region, light inside a 1D waveguided TE mode, can be transmitted with over 90% efficiency per bend [64]. One remarkable property of PC waveguides is the ability to guide light primarily outside higher-index material, which shows their fundamentally different light guiding mechanism (for an example see waveguide designs in Chapter 2). In contrast with traditional waveguides that solely operate based on index guiding (TIR), in PC waveguides, in-plane light confinement can also occur strictly due to the existence of the 2D bandgap in the region surrounding the 1D defect. To form an ultra-small 3D localized cavity, one introduces a

localized defect, such as in Fig. 1.7. This particular "*L3*" cavity actually supports several modes with distinct frequencies and associated mode profiles.

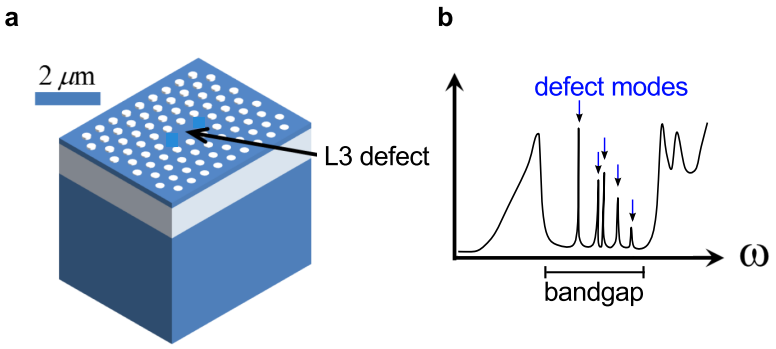

Figure 1.7: (a) Schematic of a PC L3 cavity, consisting of a defect (three missing holes) in a hexagonal lattice of holes in a silicon slab. (b) A sketch of the local photonic density of states at the cavity center.

The in-plane confinement of the defect modes is due to PBG of the PC and out-of-plane confinement is a result of TIR. But these confinement elements are not perfect in reality, which in the case of cavities, results in coupling of cavity modes to continuum modes not confined to the slab. Therefore, the energy in the cavity modes decays exponentially, which gives a Lorentzian line-shape to the cavity mode (the defect mode in Fig. 1.7b). This exponential decay can be characterized by a parameter called the "*Quality Factor*" (Q), which is related to the Lorentzian linewidth, γ, the angular resonant frequency of the cavity, ω_0 and cavity photon lifetime, τ through the following relation

$$Q = \omega_0 \tau = \frac{\omega_0}{\gamma}. \tag{1.1}$$

Referring again to Fig. 1.7, the various localized L3 cavity modes have widely ranging Q values.

The cavities act like resonators and their Q is a measure of field enhancement in these resonators. For most photonic applications that rely on light-matter interactions, cavities with higher Q are beneficial because they produce a higher field intensity for a given input laser power associated with a larger local density of photonic states. As mentioned previously, the other important factor that influences the

maximum field intensity in the cavity when resonantly exciting a particular mode is its mode volume (V), which is defined as

$$V = \frac{\int d^3\mathbf{r}\varepsilon(\mathbf{r})|\mathbf{E}(\mathbf{r})|^2}{max(\varepsilon(\mathbf{r})|\mathbf{E}(\mathbf{r})|^2)}. \tag{1.2}$$

In the above equation, $\mathbf{E}(\mathbf{r})$ is the electric field associated with the confined cavity mode [65] and $\varepsilon(\mathbf{r})$ is the dielectric constant at location $\mathbf{r}$ in the cavity. As will be shown in the following chapters, PC based defect state microcavity modes can have mode volumes less than $(\frac{\lambda}{\sqrt{\varepsilon}})^3$, in which case the peak internal field intensity is approximately Q times the incident field intensity when the Q of that mode is determined by its coupling to a single input/output waveguide channel. In contrast, the peak field intensity in ring and disk resonators is reduced in proportion to $\frac{1}{V}$.

As discussed later in this chapter, the optical forces on nanoparticles are related to the gradient of cavity electric field intensity. Therefore, both smaller mode volume and higher Q lead to larger optical forces. This is because smaller mode volume means more spatially-confined cavity modes, which increases the field intensity "*gradient*", and higher Q means more enhancement of the cavity's maximum electric field, which leads to larger electric field intensity and therefore optical force.

In this thesis, we design a cavity structure that operates at around 1.55 μm, which is the optical telecommunications wavelength. The PC in this design is formed by a 2D triangular lattice of holes drilled in a silicon slab of thickness 220 nm. The triangular lattice is selected because of its higher degree of symmetry, which creates omnidirectional PBG for TE polarized light propagating in any direction within the silicon slab. The structure of the cavity is optimized to have high-Q in fluidic medium where the optical trapping and sensing is taking place. The detail of the cavity design is described in Chapter 2.

1.4 Optical Tweezers

It has been a few centuries since Johannes Kepler hypothesized the presence of "*radiation pressure*" on objects. But it took nearly three centuries for experimental confirmation of radiation pressure by Lebedev [66] in 1901. Later in 1936 Richard

Beth [67] at Princeton University experimentally demonstrated angular momentum transfer between light and the matter. Invention of Lasers revolutionized opto-mechanics and led to a new class of tools, named "*Optical Tweezers*".

Since being established in the 1980s [68], optical tweezers [68–70] have been one of the most useful tools used to trap and manipulate the position of mesoscopic objects, giving rise to rapid progress in various nanoscience areas [71–74]. The tightly focused laser beams (Fig. 1.8a) present in these tools cause dipolar coupling of light and small particles, resulting in optical forces/torques being exerted on the particles toward the focus of the laser beam. These forces/torques, which are described in the next sub-sections, enable trapping and non-contact manipulation of micro and nanoparticles with extremely high accuracy [9] (Fig. 1.8b). For instance, laser tweezers enable following the movements, forces, and strains in molecular structures during a reaction [75]. By attaching glass or latex beads to macromolecules, it is possible to trap them at the laser focus and do high-accuracy position and force/torque measurements directly [9, 69, 72, 76–79]. Some other applications of laser tweezers in biology include measuring elastic properties of DNA [80, 81], characterizing the mechanical unfolding of proteins [82–84], and measuring the force in single myosin molecules [85]. All of these demonstrations are performed in fluidic environments, where the main force competing with the optical force is due to Brownian motion. This force, which is a function of thermal energy of particles, pushes them out of the equilibrium point in a random fashion. The overall motion of the particles depends on the temperature of the environment and the strength of optical forces. To keep the particles stably in the optical trap, laser tweezers typically have to produce trapping potential energies with minimum depth of $10k_BT$, where k_B is the Boltzmann constant and T is the temperature of the system.

1.4.1 Optical Force

Maxwell Stress Tensor

Since light radiation carries energy and momentum, it is intuitively understood that it can transfer its energy and momentum to an object placed in its path and

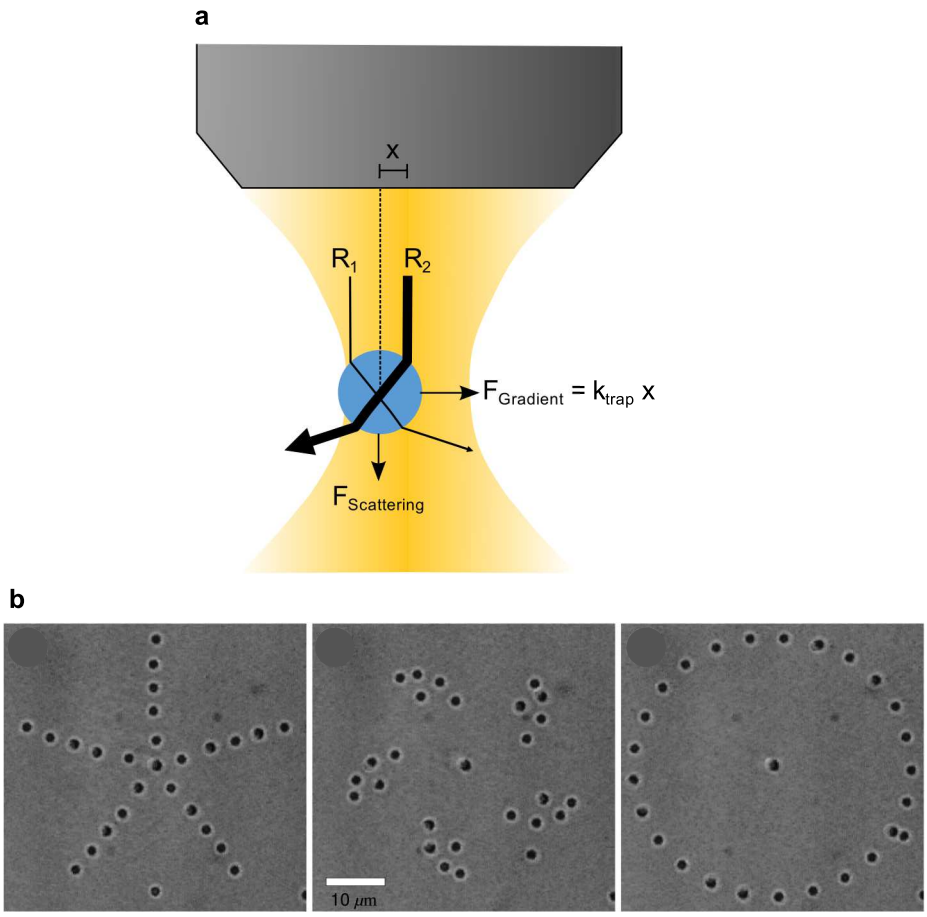

Figure 1.8: (a) Schematic focused beam of laser propagating downward that produces optical forces on a particle that has larger refractive index than its surrounding. Two rays of light (R1 and R2) are showing the light refraction in the particle. Since R2 is coming from the focal center of the beam, its intensity is stronger, and therefore it transfers larger momentum to the particle compared to R1. Therefore, the conservation of momentum dictates the particle experiences a force toward the beam focal center. This force, which is a result of laser intensity variation and in the direction of light intensity gradient, is called the gradient force. Also, both rays exert "*scattering force*" in the direction of light propagation because of momentum transfer from refracted or absorbed light. This force tries to push the particle out of the laser trap. (b) An experimental example of optical manipulation of multiple micron-size colloidal silica spheres using laser tweezers (reprinted from [9]).

hence exert an optical force on the object. If the size of a particle is much larger than the wavelength of the light (*Mie Regime*), the optical force can be understood using ray optics. When a transparent particle enters a tightly localized radiation field, the light rays will reflect and refract and this leads to a change in the light's momentum. From Newton's third law, the particle experiences the same amount of momentum change in the opposite direction. In a non-uniform field like a Gaussian beam, this force is towards higher light intensity regions (when the refractive index of the particle is higher than the medium). As illustrated in Fig. 1.8, the particle is attracted towards the region with higher intensity of light (in the direction of the gradient of light intensity) by this "*gradient force*" and pushed away from the laser focus by axial forces due to the absorption and scattering of light.

Analytical calculations of optical forces on arbitrary objects are usually very complicated, as it requires solving Maxwell's equations to find electric and magnetic fields in different media both inside and outside the objects. Therefore, optical force calculations rely on numerical methods like Maxwell Stress Tensor (MST) [86]. In this method, the total electromagnetic field distribution including the particle is self-consistently evaluated using Finite Difference Time Domain (FDTD) or Finite Element Method (FEM) solvers [87, 88], which discretize (mesh) the whole physical system and solve Maxwell's equations numerically to find electric and magnetic fields in that system. Once these fields are evaluated, the MST is integrated over a surface surrounding the particle to calculated optical forces, as explained below.

When a particle is placed in an electromagnetic field (electric field **E** and magnetic field **B**), it gets polarized and the Lorentz force (**F**) on the induced charges (with charge and current densities ρ and **J**) inside the particle (at location **r** and time t) would be [89]

$$\mathbf{F}(\mathbf{r},t) = \int [\rho(\mathbf{r},t)\mathbf{E}(\mathbf{r},t) + \mathbf{J}(\mathbf{r},t) \times \mathbf{B}(\mathbf{r},t)]dV. \tag{1.3}$$

From Maxwell's equations we can write

$$\nabla \times \mathbf{E} \times \varepsilon_0 \mathbf{E} = -\frac{\partial \mathbf{B}}{\partial t} \times \varepsilon_0 \mathbf{E} \tag{1.4}$$

and

$$\nabla \times \mathbf{B} \times \mu_0 \mathbf{H} = [\frac{1}{c^2}\frac{\partial \mathbf{E}}{\partial t} + \mu_0 \mathbf{J}] \times \mu_0 \mathbf{H} \tag{1.5}$$

and adding these two equations gives

$$\varepsilon_0(\nabla \times \mathbf{E}) \times \mathbf{E} + \mu_0(\nabla \times \mathbf{H}) \times \mathbf{H} = -\frac{1}{c^2}\frac{\partial \mathbf{H}}{\partial t} \times \mathbf{E} + \frac{1}{c^2}\frac{\partial \mathbf{E}}{\partial t} \times \mathbf{H} + \mathbf{J} \times \mathbf{B}. \tag{1.6}$$

The two terms on left hand side of Equation 1.6 can be written as

$$\begin{aligned} \varepsilon_0(\nabla \times \mathbf{E}) \times \mathbf{E} + \mu_0(\nabla \times \mathbf{H}) \times \mathbf{H} = \nabla \cdot [\varepsilon_0 \mathbf{E} \otimes \mathbf{E} - \frac{\varepsilon_0}{2} E^2 \overleftrightarrow{I}] - \rho \mathbf{E} \\ -\nabla \cdot [\mu_0 \mathbf{H} \otimes \mathbf{H} + \frac{\mu_0}{2} H^2 \overleftrightarrow{I}], \end{aligned} \tag{1.7}$$

where $\otimes$ refers to tensorial product and $\overleftrightarrow{I}$ is identity tensor. As a result, Equation 1.6 simplifies to

$$\nabla \cdot \overleftrightarrow{T} = \rho \mathbf{E} + \frac{1}{c^2}\frac{\partial (\mathbf{E} \times \mathbf{H})}{\partial t} + \mathbf{J} \times \mathbf{B}, \tag{1.8}$$

where $\overleftrightarrow{T}$ is MST and is defined as (for material floating in vacuum background):

$$\overleftrightarrow{T} = \varepsilon_0 \mathbf{E} \otimes \mathbf{E} - \mu_0 \mathbf{H} \otimes \mathbf{H} - \frac{1}{2}(\varepsilon_0 E^2 + \mu_0 H^2)\overleftrightarrow{I}. \tag{1.9}$$

In the case of non-vacuum background, ε_0 and μ_0 in equation should be replaced with those of the background medium (i.e. ε and μ). Integrating Equation 1.8 over an arbitrary volume V with surface A that encloses all charge and current densities (ρ, $\mathbf{J}$) results in

$$\oint_A \overleftrightarrow{T} \cdot d\mathbf{A} = \int_V (\rho \mathbf{E} + \mathbf{J} \times \mathbf{B}) dV + \frac{1}{c^2}\frac{d}{dt}\int_V \mathbf{E} \times \mathbf{H} dV. \tag{1.10}$$

On the right-hand side, the first term is the Lorentz force on the polarized particle (Equation 1.3) under illumination and the second term is the time variation of the field momentum. For steady state, the second term becomes zero when the time dependence of the fields is described as $e^{-i\omega t}$ which is zero when averaged over a full optical cycle [90]. Therefore, after averaging Equation 1.10 over a full optical

cycle and using Equation 1.3, we can write

$$\langle \mathbf{F} \rangle = \oint_A \overleftrightarrow{T} \cdot d\mathbf{A}. \tag{1.11}$$

Thus, to rigorously find the radiation force on a particle we should define a closed surface surrounding the particle and then integrate the MST on this closed surface. The result is the average force on the particle. To compute the optical force on a particle, only **E** and **H** on a closed surface are required, and these fields are self-consistent, meaning they are the sum of incident and scattered fields. Similarly MST can also be used to calculate the optical torque as demonstrated in Ref. [91].

Although MST is a rigorous method, for practical purposes it is computationally expensive to perform. As mentioned above for finding the optical forces, the electromagnetic fields are needed over a closed surface. This means that to find the optical forces on a particle that is in motion, all self-consistent calculations of the fields have to be done for each position of the particle. As will be discussed in the next chapter, each simulation that calculates the fields takes a few hours to run for our optical tweezers, and this makes it impractical to study the motion of a particle in out optical tweezers. In the next sub-section, an approximation is explained that can be applied to tiny nanoparticles ($<< \lambda$) and greatly reduces the computational cost of force calculation. Since the particles that we are dealing with in this research are in this category, all force calculations in this work are performed based on this approximation.

Dipole Approximation

When the size of a particle is much smaller than the illumination wavelength (less than $\frac{1}{20}$ of the wavelength according to Ref. [92]), we can assume the polarization density inside the particle's volume is uniform and only dependent on the incident field at the center of the particle. In this regime ("*Raleigh regime*"), the particle's response to the incident field can be assumed to be like a point dipole which gets uniformly polarized in the radiation field. This assumption is known as the "*Dipole Approximation*" and as shown below, it significantly simplifies and speeds up the force and torque calculations.

The radiation force on a dipole-like particle that possesses no static dipole mo-

ment and responds linearly to an external electric field with polarizability α is given in Ref. [89]:

$$\mathbf{F}(\mathbf{r},t) = (\mathbf{p}(\mathbf{r},t)\cdot\nabla)\mathbf{E}(\mathbf{r},t) + \frac{d}{dt}\left[\mathbf{p}(\mathbf{r},t)\times\mathbf{B}(\mathbf{r},t)\right], \tag{1.12}$$

where $\mathbf{F}(\mathbf{r},t)$ is the total dipole force, $\mathbf{E}(\mathbf{r},t)$ and $\mathbf{B}(\mathbf{r},t)$ are the electric and magnetic fields, and

$$\mathbf{p} = \alpha\mathbf{E} \tag{1.13}$$

is the dipole moment of the particle. If we assume the particle is moving slowly in an optical cycle, we can time average the optical force on a full cycle and by assuming time harmonic electromagnetic fields, the second term on the right side in Equation 1.12, which corresponds to the momentum of the incident light vanishes. As a result, Equation 1.12 becomes

$$\langle\mathbf{F}(\mathbf{r},t)\rangle = \langle(\mathbf{p}(\mathbf{r},t)\cdot\nabla)\mathbf{E}(\mathbf{r},t)\rangle, \tag{1.14}$$

which, considering harmonic fields of the form $\mathbf{E}(\mathbf{r},t) = \mathbf{E}_0(\mathbf{r},\omega)e^{i(-\omega t+\phi(\mathbf{r}))}$ and a complex polarizability of $\alpha = \alpha' + i\alpha''$, can be reformulated as

$$\langle\mathbf{F}(\mathbf{r},\omega)\rangle = \frac{\alpha'(\omega)}{4}\nabla(|\mathbf{E}_0(\mathbf{r},\omega)|^2) + \frac{\alpha''(\omega)}{2}|\mathbf{E}_0(\mathbf{r},\omega)|^2\nabla\phi(\mathbf{r}). \tag{1.15}$$

The first term of Equation 1.15 corresponds to the gradient of intensity, which is also known as the dipole term. This part of the force comes from the interaction between the external electric field and the induced dipole moment of the particle and acts in the direction of the gradient of electric field intensity. The second term, which corresponds to the dissipative part of the polarizability, results from transfer of momentum of light to the particle (usually known as scattering force). In the case of lossless particles or standing waves (the case that corresponds to PC cavity modes) the second term in Equation 1.15 vanishes. This is one advantage of standing waves over propagating waves, because the scattering force can move the particle out of the stable trapping point defined by the dipole term (i.e. the point with highest intensity). For this case, it is possible to define a potential energy for

the trapping force field that takes the form

$$U(\mathbf{r},\omega) = -\frac{\alpha'(\omega)}{4}\left|\mathbf{E}_0(\mathbf{r},\omega)\right|^2. \tag{1.16}$$

The depth of this potential is the figure of merit for the effectiveness of the optical trap for overcoming the random Brownian motion of the particles. As a rule of thumb, a minimum potential depth of $10k_BT$ is needed for stable trapping [29]. With the same procedure and again within the dipole approximation it is possible to derive the mechanical torque generated by optical radiation on a dipole-like particle [89], which is

$$\boldsymbol{\tau} = \frac{1}{2}Re[\mathbf{p}^* \times \mathbf{E}]. \tag{1.17}$$

To calculate the optical force and torque on a particle in the dipole approximation, we only need to know the polarizability of the particle to be trapped, and the spatial distribution of the incident electric field (not the self-consistent field), which is extremely less expensive computationally compared to the more rigorous MST method.

1.4.2 NanoTweezers

Optical tweezers – tightly focused laser beams that trap and manipulate micron-size particles [68–70] – have enabled a truly impressive array of scientific breakthroughs [71–74]. But as demonstrated in the previous section (see Equation 1.15), the trapping force is dependent on the gradient of the electric field intensity, which relies on the focusing power of the laser tweezers' microscope objective and therefore is ultimately diffraction-limited. Since a Rayleigh particle's polarizability is proportional to its volume, large laser powers are required to trap nanoscale particles. In standard optical tweezers, a 100 nm polystyrene sphere requires 15 mW [68] of laser power. This implies that for a 10 nm sphere $\sim$ 15 W of laser power would be needed [93]. Increasing the laser power to above 10 mW may easily cause photo-damage to the trapped particles (especially biological objects) and increased Brownian motion because of the heat it produces [94].

To overcome these drawbacks of conventional laser tweezers, namely cubic wavelength trapping volumes and large laser power requirements, a novel class

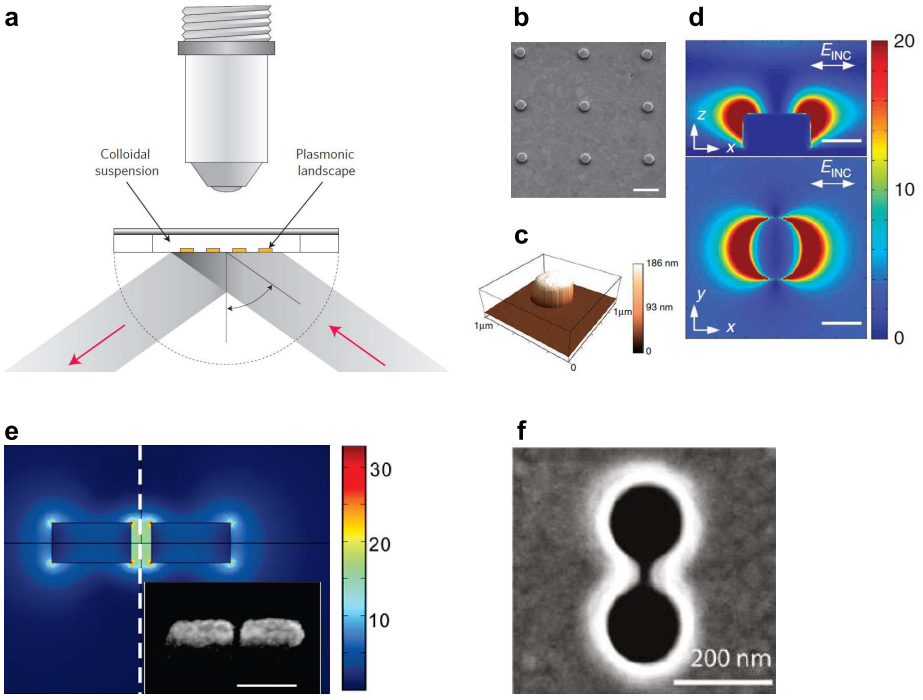

Figure 1.9: (a) Schematic of a plasmonic nanotweezers experimental set-up, in which a pattern of micrometre-sized gold structure is illuminated under the Kretschmann configuration through a glass prism. The red arrows give the direction of the incident and reflected light (reprinted from [10]). (b)-(c) SEM and atomic force microscope images of fabricated gold nanopillars. Scale bar is 1 μm (reprinted from [11]). (d) FDTD calculation of the electric field intensity distribution resulting from incidence plane wave illumination of a nanopillar at $\lambda = 974$ nm. Intensity enhancement, that is, intensity normalized to incident intensity $|E|^2/|E_{INC}|^2$, is plotted. Peak intensity enhancement is 490 times, although upper limit of colour scale is chosen to be 20 times for visualization. The scale bar is 200 nm (reprinted from [11]). (e) Electric field amplitude distribution of a nanoantenna with 80 nm arm and 25 nm gap. The inset shows the SEM image of a fabricated nanoantenna with 10 nm gap. The scale bar is 100 nm (reprinted from [12]). (f) Double-hole nanotweezers with a 15 nm tip separation used for trapping 12 nm silica spheres (reprinted from [13]).

of "*Nanotweezers*" has emerged [69, 93], which relies on strong local enhancement of the exciting laser intensity. These new types of tweezers, which are mostly plasmon-based [10] or dielectric cavity-based [95], confine light into extremely small regions and enhance its intensity, allowing for ultra-accurate and non-invasive positioning of single nano-objects at low excitation powers. Furthermore, because of their considerably smaller footprint, they enable optical trapping and manipulation of small particles on Lab-on-Chip systems at reduced costs.

The collective resonant excitations of plasmons in metallic nanostructures (known as Localized Plasmon Polaritons (LPP)) gives rise to a large electric field enhancement in the near-field of the nanostructures. Because of the small features of these nanostructures (see Fig. 1.9), their plasmonic resonances have a very large electric field gradient and thus, produce a strong optical gradient force [96]. The first experimental demonstration of metallic nanotweezers was done with micron-sized polystyrene particles with metallic nanopillars patterned on a glass substrate. The LPP of the pillars was excited by the evanescent light of a laser passing through a prism by TIR [97] (see Fig. 1.9a-d). Smaller metallic "*nano-antennas*" with different shapes have subsequently been fabricated and used to trap (Fig. 1.9e-f) 10 nm gold nanoparticles [12] and 12 nm silica spheres [13]. In another more significant demonstration [98], a single 3.4 nm Bovin serum albumin protein molecule has been trapped using double-hole nanotweezers with ~ 10 mW of incident power. The huge improvement in the size of the trapped nanoparticles in these metallic nanostructures is because of the extreme sub-wavelength concentration of the field, which gives rise to enormous field enhancements near the surface of the metal. Another benefit of these nanotweezers is their compatibility with microfluidic integration as demonstrated in Ref. [99].

A second type of nanotweezer is based on dielectric photonic microcavities (resonators) that *only* confine light down to volumes on the order of a cubic wavelength in the host dielectric, but that can have high Q factors [3]. The high Q factors can, to a large degree, offset the lesser confinement (compared to plasmonic nanotweezers), by resonantly building up a larger modal field intensity for a given CW excitation power. These dielectric cavity structures also offer the significant advantage of being easily integrated with other optical elements on Photonic Lightwave Circuits (PLC) for more complex nanomanipulation like sorting

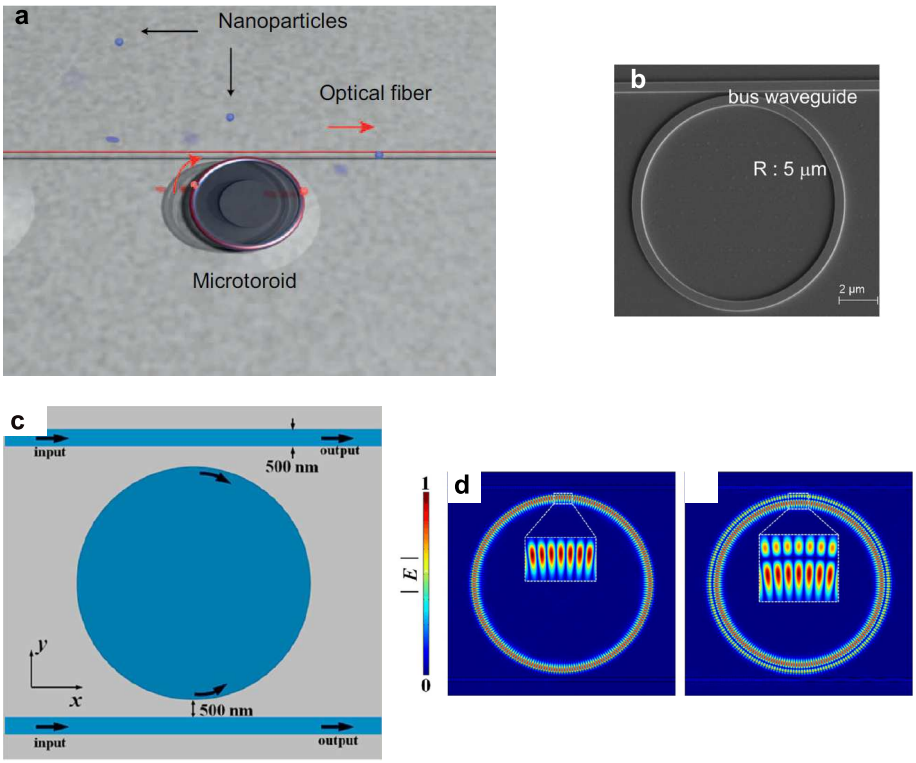

Figure 1.10: (a) Schematic of a microtoroid coupled to an optical fiber (not to scale) (reprinted from [14]). In this system, a frequency-tuned laser beam is evanescently coupled to a 90 μm diameter microtoroid by an optical fiber (red). The microtoroids have loaded Qs (i.e. Q of a cavity when connected to waveguides in a circuit) of 1×10^5–5×10^6 in water at 633 nm and can trap 5 nm silica nanoparticles. (b) SEM images of a 5 μm radius microring nanotweezers with Q factor of 860 (reprint from [15]). Polystyrene particles with diameters of 500 nm can be stably trapped and propelled along the microring resonator with speeds of 110 μm/s at 9 mW in the bus waveguide. (c)-(d) The top-view schematic of a microdisk resonator with two bus waveguides along with the normalized electric field amplitude distribution of its modes. The corresponding zoom-in-view images near the coupling gap are shown in the insets (reprinted from [16]). A 30 μm diameter, 700 nm thick SiN microdisk resonator has been demonstrated [17] to trap 1 μm polystyrene particles with $\sim$ 7 mW of input power with quality factors from 3000-6000.

and storing [15, 18–20, 100].

One group of cavity-based nanotweezers (Fig. 1.10) includes microdisks [17], microtoroids [14] and microrings [15] which confine light through TIR (also known as "*Whispering Gallery Mode*" resonators). They have Q factors from a few hundreds to several millions and can trap particles ranging from 5 nm to a few microns with about 10 mW of power [15–17]. The other main category of cavity-based nanotweezers exploit PC microcavities that were described in Section 1.3. Light in these nanotweezers is confined to a defect region in a photonic band-gap structure, where light propagation of a certain range of frequencies is inhibited. These cavities have comparable Q factors as WGM resonators but they can have much smaller mode volumes, which reduces the required power for optical trapping by increasing the light-matter interaction strength.

In 2010, the first experimental demonstration (Fig. 1.11a-b) of optical trapping using PC nanotweezers was done [18] on $\sim$ 50 nm polystyrene nanoparticles with a 1D PC resonator (also known as a "*nanobeam*" cavity). The loaded Q for this device is 2500 in water. In the same article, the ability of these nanotweezers to transport, trap, and manipulate larger nanoparticles by simultaneously exploiting the propagating nature of the light in a coupling waveguide was demonstrated. This class of optical nanotweezers lays the groundwork for photonic platforms that could eventually enable complex all-optical single molecule manipulation and directed assembly of nanoscale material [18]. Two years later, the same group developed a new 1D silicon-nitride PC nanotweezer ((Fig. 1.11c) that can trap and release quantum dots, and 22 nm polymer particles [19]. This nanobeam cavity has a Q factor of $\sim$ 5000 and mode volume of $\sim$ 4.4 cubic wavelengths, which operates with $\sim$ 10 mW of coupled power into the resonator. In Ref. [101], a 1D nanobeam cavity with Q factor of $\sim$ 2000 and mode volume of a cubic effective wavelength (i.e. the wavelength inside silicon which is the cavity material), was exploited for the auto-assembly of 1 μm dielectric particles inside an optofluidic cell designed to enable the assembly of multiple particles with different stable conformations at 0.3mW injected power. The same group in a proof-of-concept demonstration [102], used multiple coupled nanobeam cavities to create a reconfigurable nanotweezers, which upon switching the excitation wavelength between different resonances of the nanotweezers, could manipulate the orientation of the

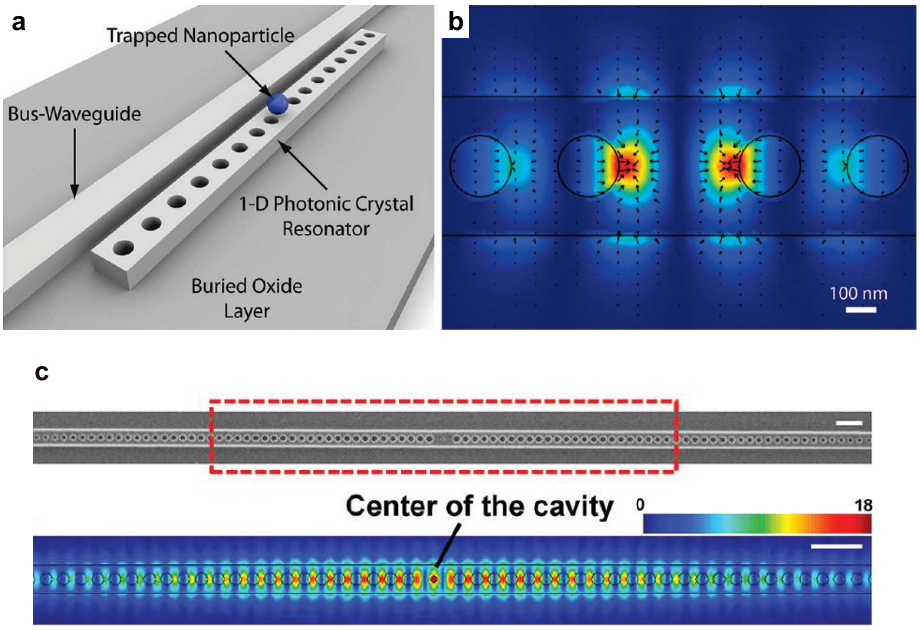

Figure 1.11: (a) Schematic of a 1D PC resonator for enhanced optical trapping. (b) Simulated electric field intensity profile of the cavity mode showing the strong field confinement and amplification within the one-dimensional resonator cavity. The black arrows indicate the direction and magnitude of the local optical forces (reprinted from [18]). (c) SEM image of a silicon nitride PC cavity along with FDTD simulation showing the electric field intensity distribution near the resonator cavity (arbitrary unit). Strong field enhancement can be seen within the small hole at the center of the cavity. Scale bars are 1 μm (reprinted from [19]).

trapped microspheres.

Although the first predictions [103, 104] about the use of PC nanotweezers for optical trapping referred to 2D PC cavities, it was not until 2013 that the first and only other experimental demonstration was published [20]. In this work, as shown in Fig. 1.12, 500nm dielectric particles were optically trapped in a cavity with Q factor of 2000 and injected power of 120 μW in the waveguide. The main advantage of this structure compared to previously discussed 1D PC nanotweezers, is the good overlap between the cavity mode electric field and the trapped nanoparticle

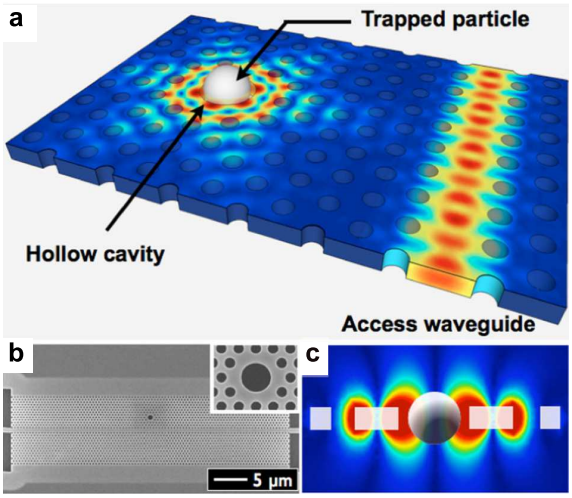

Figure 1.12: (a) Schematic of a 2D PC hollow resonator along with its simulated electric field intensity profile of the cavity mode showing the strong field confinement and amplification within hollow region. (b) SEM image of device showing the hollow cavity and the PC waveguide. (c) The side view of the hollow cavity and the profile of the field intensity showing the good overlap between the field and the trapped particle. The experimental Q factor is 2000 and the mode volume is 0.2 time cubic wavelength. For stable trapping of 500 nm dielectric particles, 120 μW of power is launched into the PC waveguide (reprinted from [20]).

(Fig. 1.12c). The work described in this thesis builds on this concept, by modifying the cavity and coupling geometries to achieve high Q values and higher trapping forces for a given coupled laser power.

1.5 Sensing and Backaction Effect

As mentioned above, nanotweezers in general (both plasmonic and dielectric cavity-based nanotweezers) generate enhanced electric fields that are confined to tiny volumes. They also possess an additional interesting feature that is not intrinsic to conventional laser tweezers, which is their resonant behavior. All of these structures operate at well-defined resonance wavelengths that are defined by the local dielectric environment where the modal light field is enhanced. A particle trapped in the

near field of a nanotweezers' mode can therefore, in general, modify the microcavity's resonant frequency by changing that dielectric environment. The influence of the particle on the resonant frequency depends in general on its polarizability and its location within the microcavity. This is a major difference compared to the physics of laser tweezers where the particle does not have a noticeable influence on the exciting laser field. This effect, which is known as "*backaction*" [94, 105, 106], complicates the dynamics of the trapping mechanism (the coupled laser power becomes dependent on the position of the particle), but it also provides a powerful means by which to easily study the dynamics of the trapped particle, as discussed below.

In Ref. [94], the authors exploited a plasmonic nanotweezers made of a nanoaperture in a metal film to trap a 50nm polystyrene sphere that has an active role in enhancing the restoring force. They demonstrated experimentally that when a particle gets near to the nanoaperture mainly by random Brownian motion, the transmittance of the nanoaperture gets influenced by the presence of the particle because of the refractive index changes it induces in the nanoaperture environment (backaction effect). As a result of this backaction effect, which in their case was an increase in the transmittance of the nanoaperture, the light intensity and therefore optical forces on the particle is enhanced thus effectively deepening the trapping potential. On the same basis, in Ref. [27] a double-hole plasmonic nanotweezers (Fig. 1.9) enabled trapping of a 20-nm biotin-coated polystyrene particle in a solution containing streptavidin. Of particular note in [27], because the backaction modifies the transmission, the dynamics of the trapped particle could be easily monitored by simply taking time-series data of the transmitted laser intensity. This makes these nanotweezers an excellent single-molecule-resolution sensor for studying biomolecular interactions and dynamics at a single molecule level [27, 28, 107].

The backaction of trapped particles on dielectric cavity-based nanotweezers has also been studied in recent years [20, 26, 95, 105, 106, 108, 109]. All of these demonstrations are based on measuring the amount of shift in the resonance of the cavities because of the trapped particles' backaction. Using perturbative calculations [105], this shift for a cavity with a spherical Rayleigh particle (smaller

than $\frac{\lambda}{20}$ [92]) inside it is predicted to be

$$\delta\lambda = \lambda_0 \frac{\alpha' |\mathbf{E}(\mathbf{r})|^2}{2\int d^3\mathbf{r}\varepsilon(\mathbf{r})|\mathbf{E}(\mathbf{r})|^2}, \tag{1.18}$$

where λ_0 is the original resonance of the cavity before trapping the particle (empty cavity resonance), α' is the real part of particle's polarizability (for spherical particles the polarizability is defined in Equation 4.2), $\mathbf{r}$ is the permittivity of the medium at location $\mathbf{r}$ and $\mathbf{E}(\mathbf{r})$ is the empty cavity electric field at the location of the particle $\mathbf{r}$. The integral at the denominator of this equation is the energy stored in the cavity which depends on the mode profile of the cavity. This relationship shows the dependence of the cavity resonance on the trapped particle's polarizability and location.

The resulting position-dependent shift of the cavity resonance gives rise to a change in the amount of energy coupled into the cavity and therefore complicates the optical trapping physics from what it would be if the intensity of the trapping field inside the cavity was independent of the particle's position. However, in analogy with the effect of backaction in the plasmonic nanotweezers, the fact that the transmission of the trapping laser depends on the position of the trapped particle means that the transmitted intensity time-series data contains a fingerprint of the particle's dynamics, and hence offers a relatively simple means of sensing the properties of the trapped particle.

Our objectives in this project are first to design an efficient 2D PC nanotweezer that produces larger trapping forces compared to previous designs and secondly to exploit them for simultaneous trapping and sensing of sub-50 nm Au nanoparticles. The designed PC nanotweezers have small mode volume (0.1 cubic wavelength), high-Q factor (up to 7000) *and more importantly* large overlap between the cavity mode profile and the trapped particles (i.e. in contrast to disk and ring resonators, the mode lives in the space outside the dielectric medium, which can be filled with solution containing the particles to be trapped), which results in extreme sensitivity to backaction of trapped particles.

In Chapter 2, the design of these devices is described. The process includes investigating the influence of various design parameters on the performance of the devices and optimizing them using a commercial FDTD Maxwell equation solver.

In Chapter 3, the fabrication process and the experimental setup for testing the fabricated devices are described in detail. Furthermore, the initial testing result on the fabricated devices is presented and compared with the simulation results to investigate the agreement between them. The results of this chapter and Chapter 2 are published in Refs. [1, 2].

In Chapter 4, the fabricated devices are used for trapping spherical gold (Au) nanoparticles and sensing the change in the refractive index of the medium. A self-consistent model is presented to analyze the backaction of the trapped particles on the optical transmission signal of the devices during trapping experiments, which led us to estimate the size of trapped nanoparticles. This work shows that transient transmission time series data alone can be used, together with a self-consistent electrodynamic model of the perturbed cavity transmission, to quantify the size of nominally spherical Au nanoparticles with nanometre sensitivity, and to quantify the fluctuation of the particle's effective polarizability while in the trap. The results of this chapter are published in Ref. [3].

In Chapter 5, the model present in the previous chapter is generalized to include anisotropic particles and then the modified model is applied to the experimental results from trapping Au nanorods. It is explained how the rotation of the anisotropic particles modifies the transmission signal of the devices and this distinct behavior is exploited to differentiate particles with different degrees of anisotropy in the optical trap. The trapping results in this chapter are to our knowledge the first experimental demonstration of trapping *sub*-50 *nm anisotropic* particles using PC cavity-based nanotweezers.

Chapter 6 is the concluding chapter. An outlook of PC nanostructures for various applications is presented and the limitations and possible improvements of our analysis are discussed.

Chapter 2

Device Design

2.1 Introduction

The present chapter focuses on designing SOI PLCs and exploits the design flexibility of PCs to integrate high Q, low mode volume (V) microcavities wherein the mode energy resides almost entirely in the background dielectric (vacuum or a solvent) with more conventional SOI-based grating couplers, and silicon channel (ridge) waveguides, where the field is predominantly in the silicon.

Such structures (Fig. 2.1) are of interest for applications where one wants to enhance the interaction of circuit-bound photons with matter that cannot be embedded within the silicon. The relevant applications for our project are optical trapping of nanoscale objects dissolved in solution using optical forces and optical sensing, where small amounts of some material in solution is detected due to its effect on the refractive index of background medium.

In the next section of this chapter, a PLC design is introduced that allows operation in fluidic medium, which is necessary for the applications discussed above. The basic elements of a PLC for confining laser light are grating couplers for coupling laser light into the silicon slab, different types of waveguides for reshaping the light wavefront and guiding it through the PLC with minimum loss, and resonators for the ultimate light confinement. Different aspects of this design that influence its performance are investigated, and in Section 2.3 some modifications are applied to the original PLC design to enhance light confinement inside the cavity and

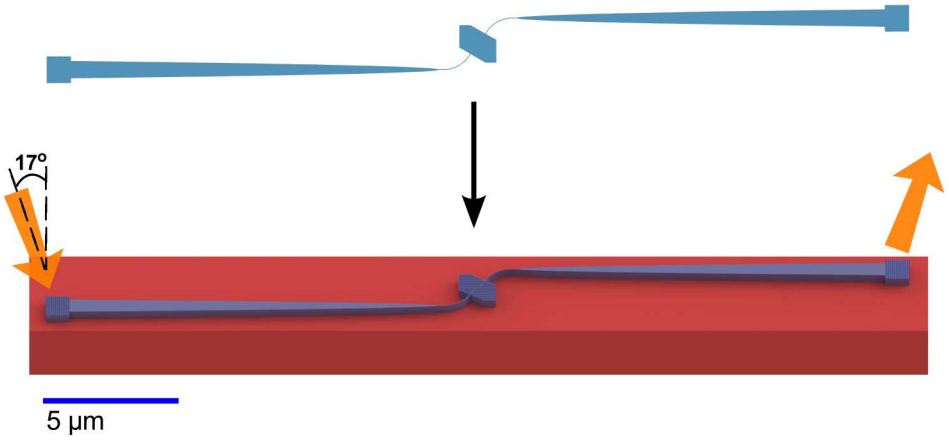

Figure 2.1: Layout of a full device SC1 including the grating couplers, cavity and waveguides sitting on SiO_2 substrate (in red). The gratings are separated by 680 microns. The input/output light is injected/collected at 17° angle to the normal to grating plane.

approach the optimal performance. The goal of the modifications is to minimize out-of-plane losses in the waveguides and increase the efficiencies of different interconnections of the PLC. To show the effectiveness of these modifications, the optical trapping force of the cavity mode on a 50 nm Au nanosphere is calculated and compared for both designs. These two designed structures are referred to as SC1 and SC2, respectively. They are studied using finite-difference time-domain (FDTD) simulation software from Lumerical Solutions [87].

All data and simulations in this thesis correspond to samples with a 220 nm thick silicon layer on top of a 3 μm thick buried oxide layer that robustly supports all circuit elements. The refractive index of the top cladding in all simulations of this chapter is assumed to be $n_{hex} = 1.365$. This is the refractive index of hexane which is a common non-polar solvent for suspending some nanoparticles (like colloidal Pb-based quantum dots). On the other hand, this number is also close to the refractive index of isopropanol ($n_{ipa} = 1.37$), a typical polar solvent for suspending another class of nanoparticles (Au, Ag nanoparticles). Therefore, the results of simulations in this Chapter are potentially applicable for trapping a wide range of nanoparticles.

2.2 SC1 Structure

The full SC1 photonic circuit that is initially designed includes a Photonic Crystal Slot (PCS) Cavity, input/output grating couplers, single mode silicon ridge waveguides, and 1D PC coupling waveguides (see Fig. 2.1). Two 2D PC grating couplers [39] are used to launch light from a tunable laser diode, via parabolic tapered waveguides, into and out of single mode silicon channel waveguides that connect to the PCS cavity region.

As illustrated in Fig. 2.1, the channel waveguides of SC1 devices are curved so that the input and output grating couplers do not sit on the same line. This makes the experimental signal measured at the output grating coupler less noisy, as the scattered light from the input grating coupler that is guided through the undercladding layer does not get detected. The design of the PCS cavity originated from "*slot-waveguide*" structures (see Fig. 2.2) developed by the authors in [21] that support propagating modes in channel waveguides wherein most of the mode profile is concentrated in the air/solvent gap between two silicon ridges. These have been used extensively in the sensor community [110, 111]. The authors in [112] showed theoretically that if such a slot waveguide was surrounded by a 1D PC on either end, a fully 3D localized mode could be trapped in a volume less than a tenth of a cubic half (free space) wavelength ($< 0.1(\lambda/2)^3$). This design assumed a slot width of only 20 nm.

It is subsequently suggested [113] a slot waveguide structure surrounded by a 2D PC that could achieve almost as small a mode volume, but for larger slot widths that should be easier to fabricate. Their cavity was defined by locally modifying just a few of the holes in the PC, nearest to the waveguide. In [114], the authors demonstrated high-Q values and strong sensitivity of resonant frequencies to the background refractive index in slot cavities defined by varying the pitch of the surrounding PC along the slot waveguide axis. These, as well as subsequent [115] high-Q PC based slot cavities, are based on "*free-standing*" structures where the underlying cladding layer is removed after the PC structures are etched into the silicon. They also required butt-coupling of the excitation source to the waveguide.

The design details of each segment of the full SC1 circuit are described in the following sub-sections.

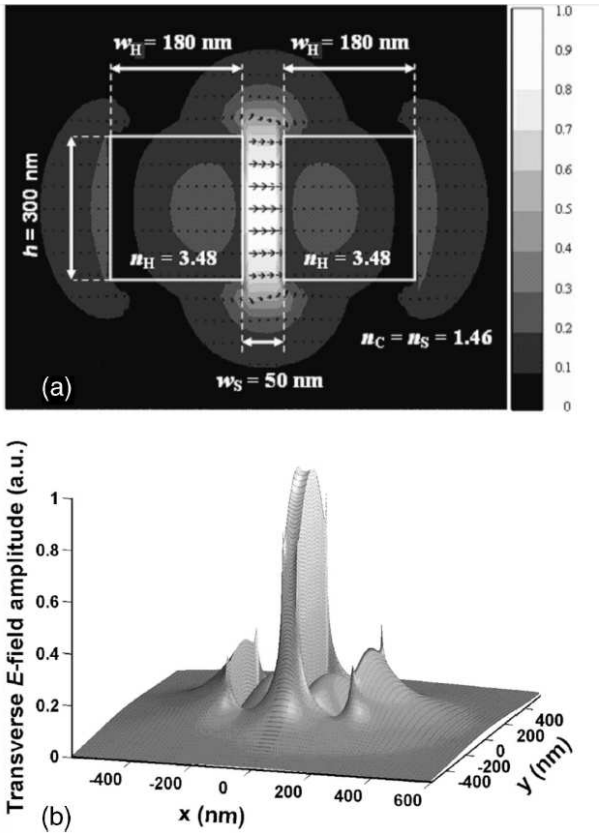

Figure 2.2: Transverse electric field profile of the quasi-TE mode in a SOI-based slot waveguide. The origin of the coordinate system is located at the center of the waveguide, with a horizontal x-axis and a vertical y-axis. n_H is the refractive index of silicon and n_C is the refractive index of SiO_2. (a) Contour of the electric field amplitude and the electric field lines. (b) 3D surface plot of the electric field amplitude (reprinted from [21]).

2.2.1 Grating Couplers and Slab Waveguides (device SC1)

The grating couplers consist of a 2D rectangular lattice of holes in a 220 nm silicon slab. This design is selected because Young's lab had experience with this type of relatively simple and efficient coupler [39]. The radius and the pitch of the grating coupler holes (see Fig. 2.3) are chosen so that the transmission efficiency of the grating coupler is a maximum at the resonant wavelength of the cavity and the incident angle required by experiment conditions. Each grating occupies an area of $\sim 20\ \mu$m $\times 20\ \mu$m and is designed for operating with *y*-polarized excitation.

The light diffracted in-plane from a grating coupler is transferred first to a tapered multimode waveguide that gradually shrinks and connects to a single mode waveguide (Fig. 2.3a). The long 300 μm parabolic shaped waveguide ensures low dissipation light transfer to the single mode channel waveguide of width 450 nm.

Using FDTD simulations, a *y*-polarized (refer to Fig. 2.3) Gaussian beam with waist diameter of 10 μm is launched into the grating coupler at a 17 degree incident angle with the *z*-axis. The source is located 90 nm above the silicon slab and its center is 5 μm away from the beginning of the tapered waveguide along the *x* axis. This *x* distance is optimized to have highest transmission efficiency for the grating coupler. The transmitted power in the beginning of the tapered waveguide and the end of single-mode channel waveguide are calculated using 2D frequency-domain power monitors (yellow lines are monitors in Fig. 2.3a). The total transmission efficiency of the whole structure as well as transmission of each of its sections is illustrated in Fig. 2.3c. The hole radius of this grating coupler is 230 nm with 795 nm and 750 nm pitches along the *x* and *y* axes, respectively. The width of the tapered waveguide at its beginning is 14 μm. The simulation region is uniformly meshed with mesh sizes of $(39.75\text{ nm}, 37.5\text{ nm}, 22\text{ nm})$ along x, y, z directions respectively. These numbers are an integer factor of the lattice pitch of the grating along the *x* and *y* directions. In the *z* direction since the structure is not periodic, the mesh size is selected based on the smallest feature size, which is the silicon slab thickness (i.e. 220 nm). These meshing considerations ensure the periodicity of the PC structures is not destroyed by discretization.

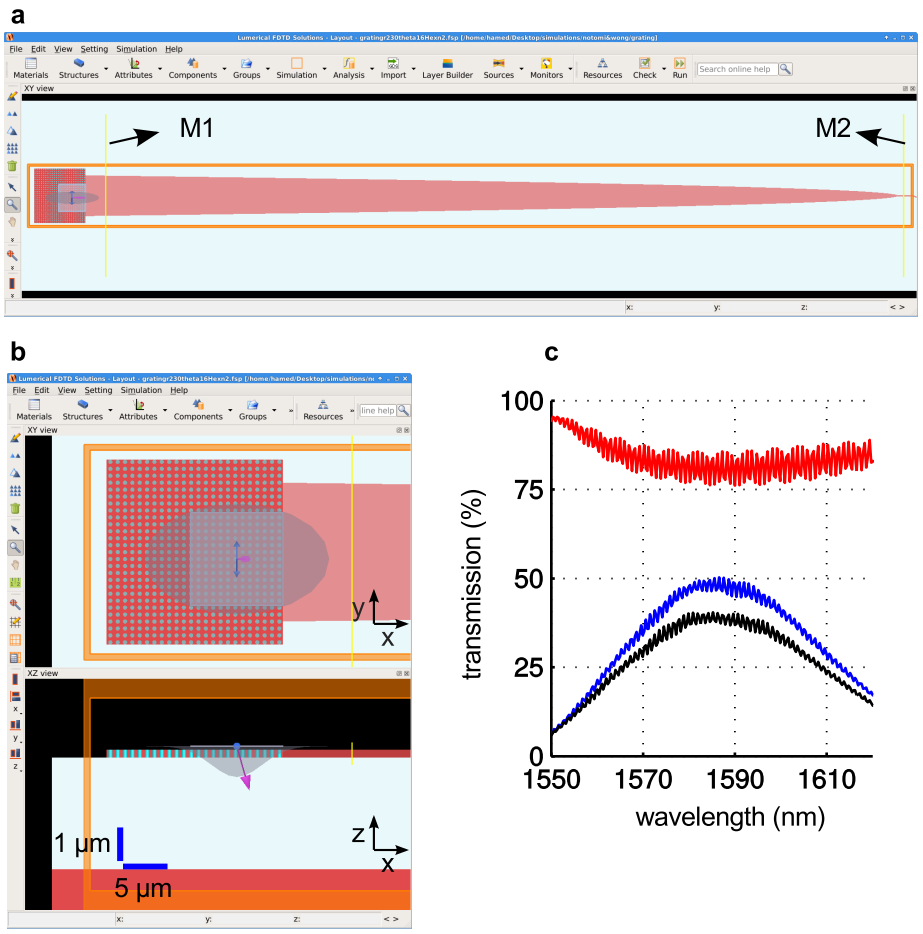

Figure 2.3: [(a)-(b)] FDTD simulation layout of the SOI grating coupler that diverts the excitation laser into a parabolic tapered waveguide connected to a single mode channel waveguide. Its polarization and injection directions are shown with pink arrows. All feature sizes are described in 2.2.1. The picture scale along *x* and *y* axes are the same but different than the *z* axis scale. (c) The transmission of this structure is calculated using two monitors (yellow lines in (a)). The blue curve is the transmission from the source up to the beginning of the tapered waveguide (monitor M1) and the black is the efficiency of the whole structure (i.e. from the source up to the channel waveguide (monitor M2). The red curve, which is the division of the black curve to the blue curve, is showing the transmission efficiency of the tapered waveguide (the structure between the two monitors).

2.2.2 Photonic Crystal Slot Cavity (SC1 device)

Here we designed a PCS cavity (Fig. 2.4) based on a design in [113, 115] that supports high-Q, small volume modes in solution without having to remove the silicon dioxide layer beneath the cavities. The background PC region comprises a hexagonal array of circular holes separated by 490 nm, and with hole radius of $r = 160$ nm, which was designed to have a TE PBG from 1495 nm to 1800 nm. To transfer laser light to the PCS cavity, the other end of single mode channel waveguide is connected via a short impedance matching region [40, 116] to W1 PC waveguides that simply omit a row of holes from the background PC.

Various defects are introduced into the background PC to excite a 3D localized mode in the center of the PC (see Section 1.3). A narrow 90 nm slot runs horizontally, through the middle of the PC, forming a distinct 1D waveguide. The W1 waveguides intersect the slot at 60 degrees (Fig. 2.4). The light in the W1 waveguides propagates primarily in the silicon, while the slot waveguide confines the light primarily in the air or solvent gap. When the position of the 3 rings of holes adjacent to the slot waveguide (different color holes in Fig. 2.4b) between the two W1 waveguides are intentionally shifted away from the slot, two 3D localized modes (Fig. 2.5a-b) are drawn out of the slot waveguide continuum [113], and these 3D localized modes are exploited in this circuit design. The 4 closest holes to the slot are shifted by $s_1 = 12$ nm, the next ring of holes (10 holes) are shifted by $s_2 = 8$ nm, and the third ring of holes (16 holes) are shifted by $s_3 = 4$ nm.

Figure 2.4b also shows how the two different waveguide types are connected via a single "*coupling hole*" (black color holes) with radius (r_c) that can vary from device to device to adjust the coupling efficiency between the 1D waveguides and the cavity. This geometry, though not fully optimized in this design, allows independent access to the slot waveguide from the ends, which may be advantageous for some applications. Also, this angled coupling between the waveguides allows for exciting both high-Q modes of the cavity which are polarized orthogonally at the cavity center. Figure 2.5a-b shows the electric field intensity distribution in the vicinity of the SC1 slot-cavity modes in hexane. Mode 1 (Fig. 2.5a) with resonance wavelength $\lambda_1 = 1567.4$ nm is more concentrated in the slot and it is mainly y-polarized and has a smaller mode volume ($V_{Mode1} = 0.1(\frac{\lambda_1}{n_{hex}})^3$). Mode 2

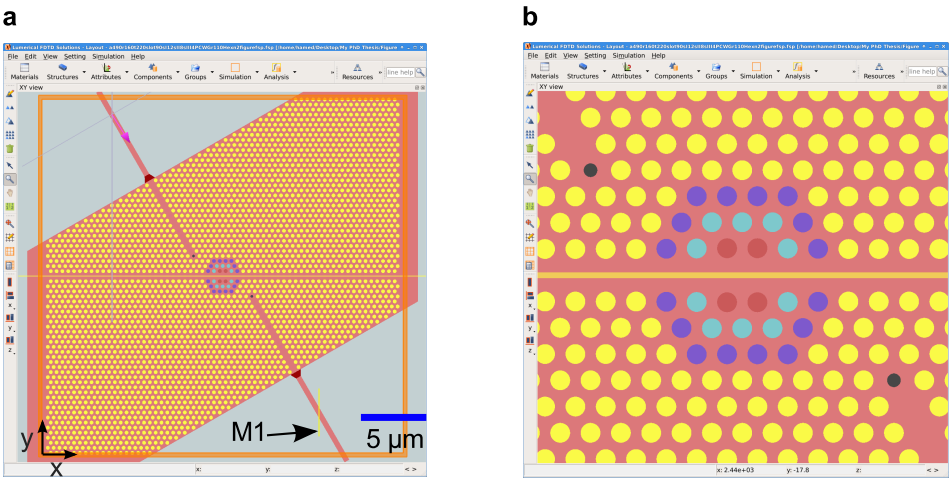

Figure 2.4: (a) Layout of a SC1 slot-cavity with input/output channel waveguides. The channel waveguides have a width of 450 nm. A mode source is used to send light into the input channel waveguide and a monitor (M1 in yellow color) is located at the output channel waveguide to calculate the transmission of the device from input to output channel waveguides (spectrum shown in Fig. 2.5c). (b) Enlarged image of the cavity region at the center of the structure. The 30 different color holes near to the slot are shifted away from it to create two defect modes. Similar color holes are shifted the same amount. The hole shifts are $s_1 = 12$ nm, $s_2 = 8$ nm and $s_3 = 4$ nm, going from inner ring of holes outward. The two smaller coupling holes at the end of PC waveguides in black color have radius $r_c = 110$ nm. The radius for the rest holes of the PC is $r = 160$ nm and the lattice period is $a = 490$ nm. The width of the slot is 90 nm.

(Fig. 2.5b) which is mainly in the four central holes of the cavity, is x-polarized at cavity center and has mode volume $V_{Mode2} = 0.4(\frac{\lambda_2}{n_{hex}})^3$, where $\lambda_2 = 1586.6$ nm. Figure 2.5c shows the theoretical transmission of the device shown in Fig. 2.4. A TE-polarized mode with well-defined power in the input silicon channel waveguide is launched towards the cavity region, and the corresponding power in the output silicon channel waveguide is calculated using a 2D frequency-domain power monitor, from which the theoretical transmission of each mode is obtained. The FDTD simulation for calculating the transmission spectra of this structure with $1240 \times 1402 \times 100$ gridpoints and using 256 processors takes ~ 40 hours to finish.

The simulation length is set to 40 ps, to obtain good resolution ($\sim$ 25 GHz) on the frequency-domain data.

2.2.3 SC1 Device Performance Discussion

The simulated resonant transmission of Mode 1 for the structure in Fig. 2.4 is 2.1%. The Q factor of this structure when the W1 PC waveguides are omitted (Q_U) is 9600 while the loaded Q (Q_L) is 7400. In the absence of losses in waveguide regions, the expected theoretical resonant transmission of this structure is $T = (\frac{Q_U - Q_L}{Q_U})^2 = 5.25\%$, which is bigger than what the FDTD simulation gives us (i.e. 2.1%). This means 60% of the power that is supposed to be transmitted to the output channel waveguide is dissipated in the waveguides and junctions. By running more simulations with power monitors at different locations, it is found that this power loss is caused by three main factors:

The first reason is evident from the W1 PC waveguide band structure shown in Fig. 2.5d. At the cavity resonant wavelengths, the PC waveguide band is located above the SiO_2 substrate light-line, which leads to coupling to continuum modes and therefore to intrinsic out-of-plane diffraction losses in the PC waveguide region. The second reason is because of out-of-plane scattering at the junction between channel and PC waveguides. In fact, nearly 33% of the injected power in the input single mode channel waveguide dissipates during traveling through the reference PC waveguide structure, as illustrated in Fig. 2.6b. In this figure, the structure consists of only channel and W1 PC waveguides with no cavity between them. Again, the first TE mode of the input silicon channel waveguide is excited and the output power is measured using power monitors. The transmission and reflection efficiencies are shown in Fig. 2.6b. The 33% power loss in this simulation is a result of scattering at the intersection of waveguides (14%) and out-of-plane scattering (19%) along the PC waveguide. The reflection is negligible at the resonance of the cavity ($\sim$ 1%).

Unfortunately, there is not much room below the light-line to be used for improving transmission efficiency through the PC waveguide section. Also, the waveguide band is almost flat below the light-line, which means slow group velocity and therefore higher losses due to scattering from rough surfaces of fabricated

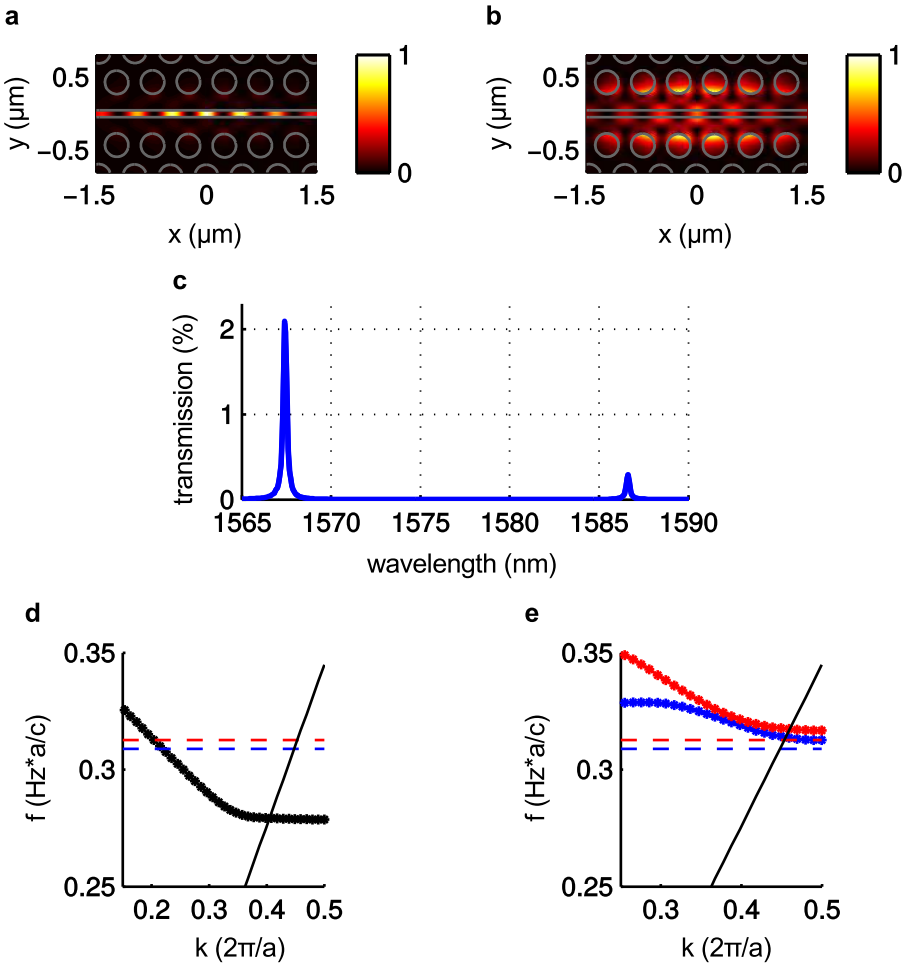

Figure 2.5: The normalized electric field intensity profile of Mode 1 (a) and Mode 2 (b) of the SC1 slot-cavity overlapped with the cavity structure. (c) The transmission efficiency of the structure in Fig. 2.4 showing two high quality modes of this cavity. The Q for Mode 1 ($\lambda_1 = 1567.4$ nm) is 7400 and Mode 2 ($\lambda_2 = 1586.6$ nm) is 8100. (d) The TE transmission band of W1 PC waveguides overlapped with SiO_2 light line (black sloped line) and two resonances of the SC1 cavity (Mode 1 in red and Mode 2 in blue color). (e) The two TE transmission bands of the PCS waveguide. The red curve has the same characteristics as Mode 1 of the cavity and blue curve corresponds to Mode 2. Again, the dashed lines are the SC1 cavity resonance modes.

devices. The other problem with such a small range of frequency is that with fabrication imperfections, it is almost impossible to achieve the target frequency.

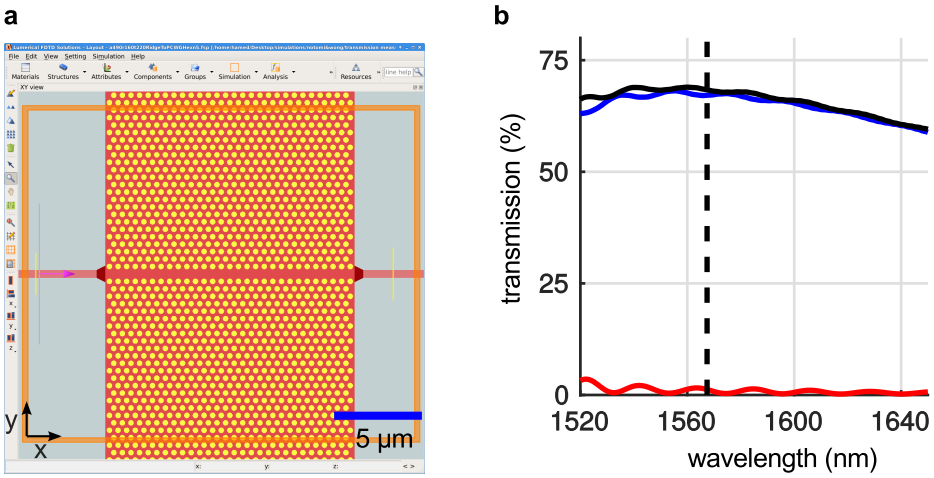

Figure 2.6: (a) Layout of the FDTD simulation for calculating the power loss in the W1 PC waveguides of the structure in Fig. 2.4. The length of the W1 PC waveguide in this simulation is 29 pitches, equivalent to the total length of W1 PC waveguides in Fig. 2.4. All feature sizes are similar to the structure in Fig. 2.4. (b) The transmission spectrum (blue), reflection spectrum (red) and the sum of them (black) for the structure in (a) calculated from input to output channel waveguide. The dashed line shows the wavelength of Mode1 of the cavity. The transmission value for the structure in (a) at Mode1 resonance is $\sim 67\%$.

The third important source of power loss is the scattering and reflection at the coupling hole at the end of the PC waveguide (see Fig. 2.7). It is found that at the resonance of Mode 1, nearly 23% of the power that passes the end of input PC waveguide reflects and dissipates around the coupling hole region. This is a large source of loss which is due to poor mode matching between the PC waveguide mode and the cavity modes. This measurement means that the overall transmission efficiency of input+output coupling holes is $(1-0.23)^2 = 60\%$, which reduces the device overall efficiency. With these fundamental losses, even by varying the coupling hole radius (see Fig. 2.4), it is not possible to get the optimized 25% efficiency required to have maximum energy in the cavity.

Despite all these sources of power dissipation, we tried to measure the func-

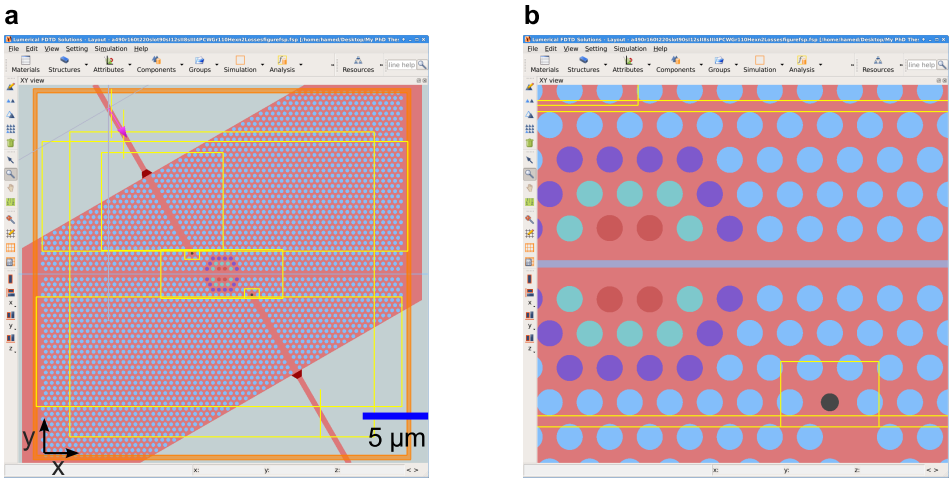

Figure 2.7: (a) Layout of the FDTD simulation for calculating the power loss in different parts of the structure in Fig. 2.4. All feature sizes are similar to the structure in Fig. 2.4 and the color of the holes are modified for better distinction from the yellow power monitors. (b) The enlarged image around one of the two coupling holes of this structure (in black color) shows the power monitor (small yellow box around the coupling hole) that measures the vertical losses occurring at this coupling hole.

tionality of the SC1 device as optical tweezers by calculating the optical trapping potentials (see Equation 1.16) generated in both modes of this cavity (see Fig. 2.8). These plots show the trapping potential energy for a 50 nm Au nanosphere produced in Mode 1 and 2 of this cavity when 1 mW (maximum power available in our experimental setup) of continuous laser power is injected into the input channel waveguide. This low laser power prevents photo-damaging of the trapped nanoparticles as often happens in more common laser tweezers.

For stable trapping, a potential depth of at least $10k_BT$ is needed [9, 29, 68], where k_B is the Boltzman constant and T is the temperature (here assumed to be 300 Kelvin). As illustrated in Fig. 2.8, the maximum potential depth of Mode 1 is $212k_BT$ and for Mode 2 this number is $17k_BT$. Therefore, even with large losses in the waveguides and inefficient coupling of this structure, both modes of this cavity theoretically produce large enough optical force to confine and trap a 50nm Au particle at mW-level laser power. For Mode 1, this calculation suggests that only

0.05 mW of power in the input channel waveguide is required to trap such particles. The main reasons for producing such strong traps at low laser power, peculiar to these particular PCS cavities, are the small volume of the modes (especially Mode 1 of the cavity) and the fact that the high intensity part of the cavity modes is outside the silicon slab and is therefore directly accessible by nanoparticles in the solution.

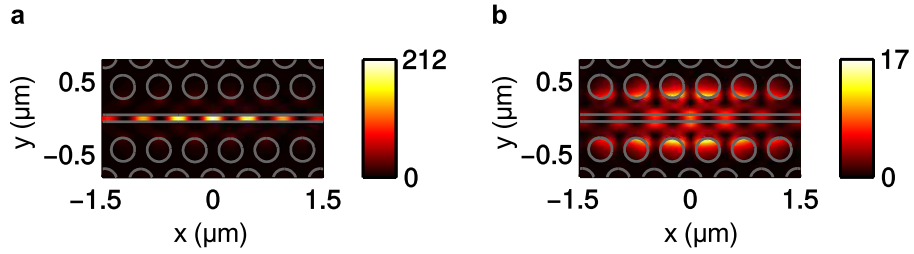

Figure 2.8: The optical trapping potential (absolute value) of the SC1 cavity (see Fig. 2.4), calculated for Mode 1 (a) and Mode 2 (b) on a 50 nm diameter Au nanosphere. The injected power in the input channel waveguide (the top waveguide in Fig. 2.4a) is 1 mW. The unit of the colorbar is in k_BT.

2.3 SC2 Structure

Although the SC1 design in the previous section has a promising ability to produce enough optical force for trapping 50 nm Au particles, it has low transmission efficiency, which limits the trapping potential of this device especially, for trapping sub-10 nm particles like semiconductor quantum dots. The ability to trap these small light sources precisely at the cavity anti-node would be very useful for building low-threshold single quantum dot lasers[24] or controlling spontaneous emission of single quantum dots for cavity quantum electrodynamics[23]. To increase the optical trapping forces, an improved PCS cavity-based design, named "*SC2*", was created, which is schematically illustrated in Fig. 2.9. The goals in designing SC2 are first to enhance the unloaded cavity Q-factor (hence reduce out-of-plane energy loss in the cavity region) and then increase the coupling efficiency of different parts of the device. All these improvements are performed for Mode 1 of the cavity as its better light confinement produces stronger optical forces compared

to Mode 2. To enhance the PCS cavity Q, some feature sizes in the PCS cavity structure are modified. And to increase coupling efficiencies for cavity Mode 1, angled coupling in the SC1 design is replaced with a butt-coupling geometry. Additionally, to further improve the SC1 design, a new grating coupler is included SC2 devices that offers larger bandwidth and slightly higher transmission. During the design process, it is attempted to avoid partially etching the silicon slab or underetching the device undercladding, which keeps the fabrication process simple with only a single lithography/single etch step.

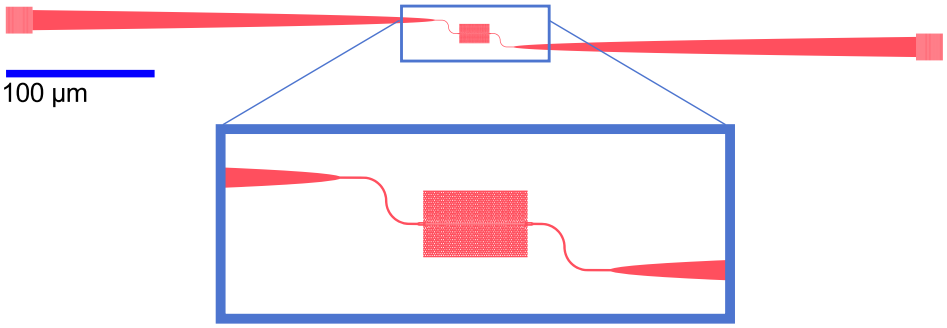

Figure 2.9: Layout of the full SC2 device including the grating couplers, cavity and waveguides. The channel waveguides are curved with radius of 5 μm.

2.3.1 PC Slot Cavity Q Factor Enhancement (SC2 devices)

By simulating slot cavities with different sets of cavity hole shifts, it is found that reducing the shift of the holes increases the Q factor of the unloaded cavity. Therefore, the hole shifts in the SC1 structure get halved to $s_1 = 6$ nm, $s_2 = 4$ nm, $s_3 = 2$ nm in SC2 devices. The minimum shift is held at 2 nm for an easier fabrication process. Since reducing the hole shift increases cavity effective refractive index and hence the resonance wavelength of the cavity, we modified the radius of the background PC holes as well as the width of the slot to keep the cavity resonance nearly the same as the SC1 cavity. The reason is to keep the resonance in the middle of our laser working range (1520 nm to 1630 nm). The hole radius of the SC2 PC is reduced by 10 nm to 150 nm and the pitch of the PC lattice is kept at the same value of 490 nm. The slot width is 100 nm for this design.

The theoretical Q of Mode 1 of SC2 cavity, when no waveguide is connected to it, is 18500, as shown in Fig. 2.10. This number is increased compared to the Q of SC1 cavity (9600 for Mode 1), which means less vertical loss in the new cavity design.

2.3.2 Photonic Crystal Slot (PCS) Waveguide Optimization (SC2 device)

As discussed in 2.2.3 the losses in the W1 PC waveguides are limiting the transmission of SC1 devices due to vertical losses. Therefore, in SC2 devices, we attempted to find a better way of loading the cavity. Since Mode 1 is mostly concentrated in the slot and its shape is basically a perturbed version of the PCS waveguide mode, it is expected that a butt-coupled geometry through the PCS waveguides would be a more efficient way of exciting cavity Mode 1. Therefore in the SC2 design, we exploited the PCS waveguides to couple light into cavity Mode 1.

To be able to guide light in PCS waveguides, the nearest row of holes next to the slot are moved away from the slot in SC2 design. By shifting the nearest row of holes away from the slot, it is possible to shift down the PCS waveguide mode into the bandgap and transfer light through it. The amount of side-shift is determined by considering two factors: i) The group velocity of the mode which determines the scattering loss in the PCS waveguide, ii) the mode profile matching between the PCS waveguide mode and Mode 1 of the cavity which influences the coupling strength between the modes. It is found a hole shift of 40 nm is a good compromise of both factors. Larger shifts lead to worse mismatch between mode profiles, and smaller shifts result in slow group velocities, which cause higher scattering losses. Figure 2.11 shows the band structure of PCS waveguides (shown in Fig. 2.14 with three different side-shifts for the first row of holes) compared to a W1 PC waveguide. Reducing the amount of hole shifts gives rise to shifting up the PCS waveguide band, which means the cavity resonance (black dashed line) will intersect the PCS waveguide band at its flat end. This shallow slope of the PCS waveguide mode causes higher scattering losses.

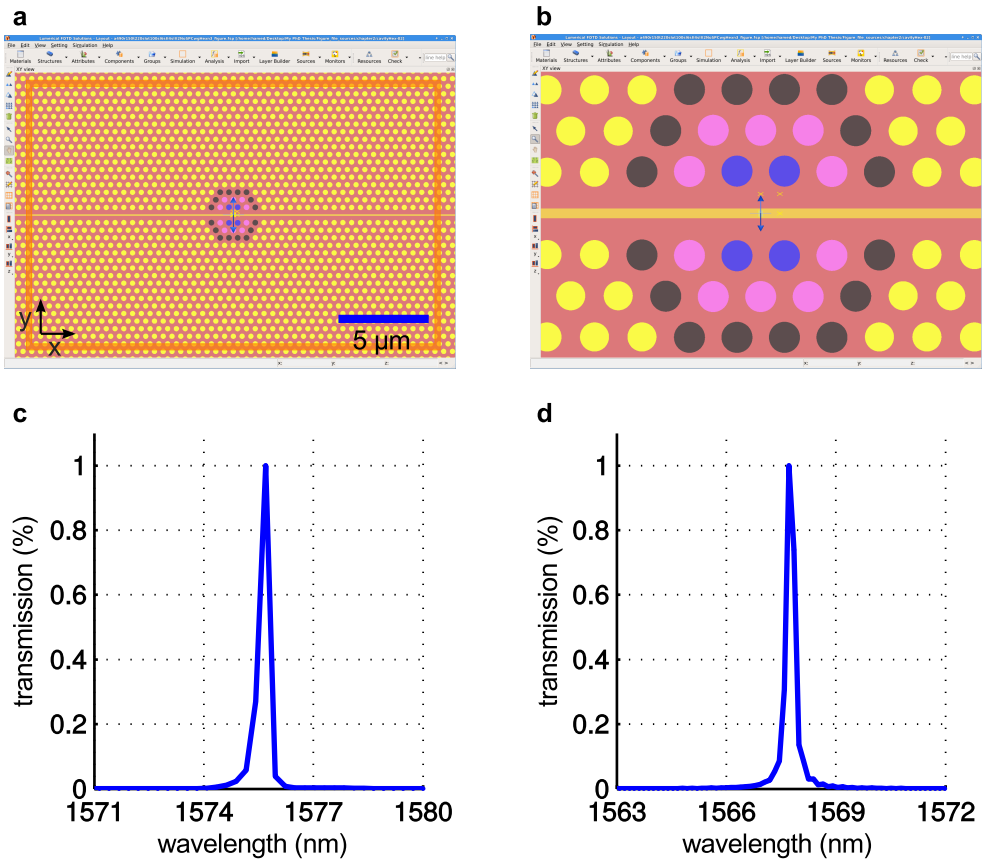

Figure 2.10: [(a)-(b)] The FDTD simulation layout showing the size of the simulation region (orange rectangle) and the location of *y*-polarized electric dipole source (double-side blue arrow). The yellow crosses are the point time monitors to record the decay of the cavity electric field in time domain. The radius of the holes is $r = 150$ nm, the slot width is $s = 100$ nm and the cavity hole shifts are $s_1 = 6$ nm (black color holes), $s_2 = 4$ nm (pink color holes) and $s_3 = 2$ nm (blue color holes). The Fast Fourier Transform (FFT) of the electric field of mode 1 measured by time monitors for SC2 (c) versus SC1 (d) cavity design. The cavity is unloaded and is sitting on BOX layer (3 μm thick SiO_2 on top of a millimeter thick silicon) and hexane is the upper cladding. The *Q*-factor of Mode 1 for SC2 cavity design (c) is 18500 while for SC1 cavity design (d) is 9600. The mode volume of Mode 1 in SC2 structure is $V_{Mode1} = 0.14(\frac{\lambda_1}{n_{hex}})^3$, while in SC1 structure was $V_{Mode1} = 0.1(\frac{\lambda_1}{n_{hex}})^3$.

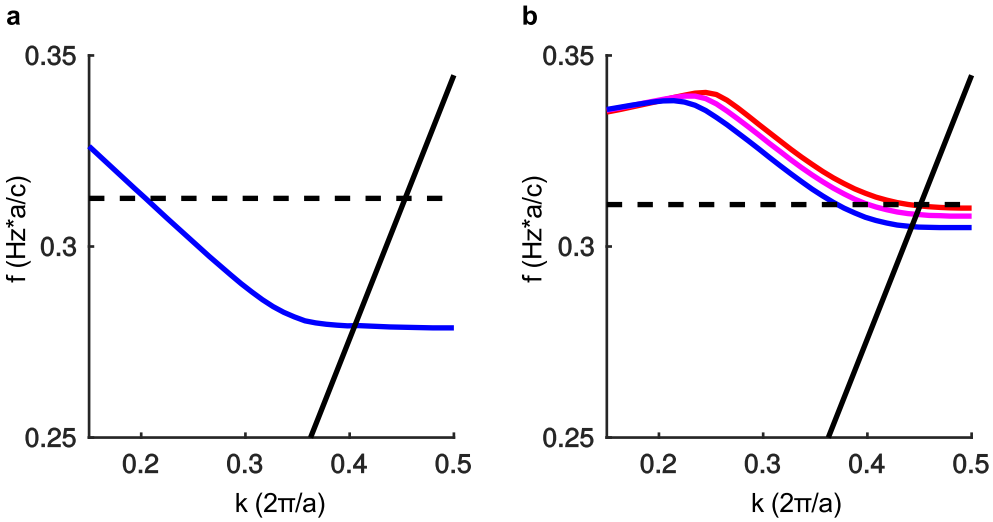

Figure 2.11: (a) Transmission band structure of the W1 PC waveguide calculated using 3D FDTD simulations (PC hole radius of 160 nm). The solid black line is the light-line for SiO_2 under-cladding and the dashed line is the resonance of mode1 of the initial design (i.e. Fig. 2.10d). (b) Transmission band structure of a PCS waveguide with hole radius of 150 nm and slot width of 100 nm. The first row of holes adjacent to the slot are shifted by 15 nm (red), 25 nm (pink), and 40 nm (blue) from their lattice point to lower the waveguide band frequency so that it intersects with the cavity mode to guide light in/out of it. Again, the solid black line is the light-line for SiO_2 under-cladding. But the dashed line is the resonance of mode1 of the improved cavity (i.e. Fig. 2.10c).

2.3.3 1D Nanowire to Slot Waveguide Adapter (SC2 device)

Since ridge or nanowire waveguides are most often used for routing signals in photonic circuits, it is important and nontrivial to efficiently couple light from them into slot-style waveguides. The challenge is rooted in the effective index and mode profile mismatch between typical nanowire and slot waveguide modes.

Several proposed designs for efficient coupling between nanowire and slot waveguide modes include structures in which tapers delocalize the mode from the nanowire and the evanescent fields are coupled into the slot [117–120]. High transmission efficiencies ($\sim$ 97%) have been achieved with tapered structures [117, 118] which are approximately 10 μm in length.

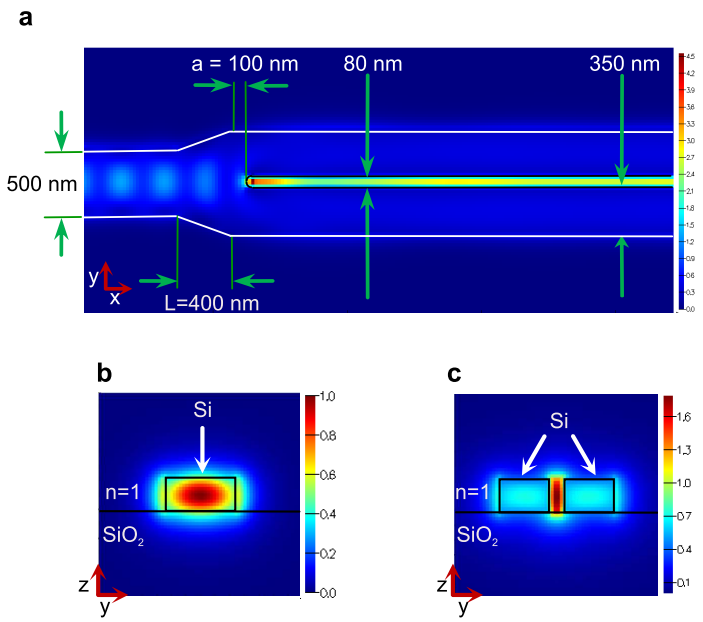

Figure 2.12: (a) The proposed nanowire to slot waveguide structure is outlined in white along the outer extremities and in black along the slot. The intensity profile at $\lambda = 1550$ nm is plotted along the $z = 0$ plane for a coupler with $L = 400$ nm, and $a = 100$ nm and coupling efficiency 92%. For positive (negative) a, the slot end is outside (inside) of the tapered region. Mode intensity profile is plotted for (b) the fundamental silicon nanowire mode, and (c) the lowest order slot waveguide mode at $\lambda = 1550$ nm.

Here, we propose a *compact* Y-branch nanowire-to-slot waveguide coupler that has smaller footprint (< 500 nm in length) and has $> 90\%$ efficiency for both forward and reciprocal coupling, both in air and solvent, over a bandwidth of ~ 200 nm.

The structure shown in Fig.2.12 is designed to efficiently couple light between the fundamental transverse electric (TE) mode of a 500 nm wide nanowire waveguide (this is wider than 450nm, which is used in SC1 devices, to increase the coupling efficiency to the slot waveguide) in a 220 nm silicon slab and the lowest order TE slot waveguide mode of two 350 nm wide dielectric slabs, separated by an 80 nm wide slot. The silicon nanowire is linearly expanded over length L out to the

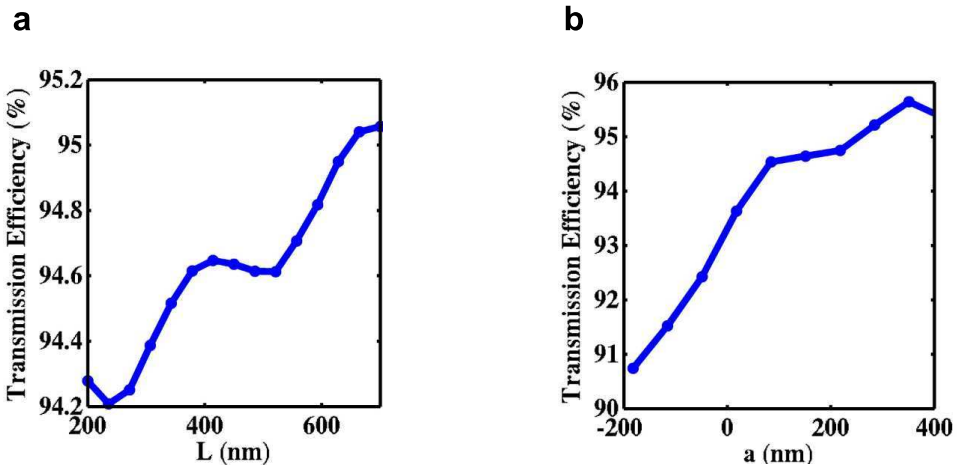

Figure 2.13: The transmission is plotted as a function of (a) the coupler length L (with $a = 100$ nm), and (b) the position of the slot end a (with $L = 400$ nm), for $\lambda = 1550$ nm.

two dielectric slabs. The slot is truncated with a circular end cap, positioned a distance a away from the slot waveguide end. The silicon slab lies on top of silicon dioxide, and is immersed in either air or hexane with refractive index 1.365 at 1.55 μm.

The structure is studied using FDTD simulations. The nanowire TE-polarized mode is launched and the transmission through the cross-section of the slot waveguide is monitored. To determine the coupling efficiency of light into the lowest order slot waveguide mode, the overlap integral between the transmitted field and the slot mode profile is calculated. The nanowire and slot waveguide mode intensity profiles in the cross-section plane are plotted in Fig. 2.12(b) and (c), respectively.

The width of the two dielectric slabs of the slot waveguide are chosen such that light is primarily coupled into the mode shown in Fig. 2.12(c), and there is minimal coupling to other slot waveguide modes, which have lower concentration of light in the slot region.

The structure is optimized based on the transmission from the nanowire to the slot waveguide, as measured by the monitor. Figure 2.13(a) shows that the transmission varies slowly as a function of the taper length for $L = 200$ to 700 nm and $a = 100$ nm. A coupler length of 400 nm yields a transmission efficiency of $> 94\%$,

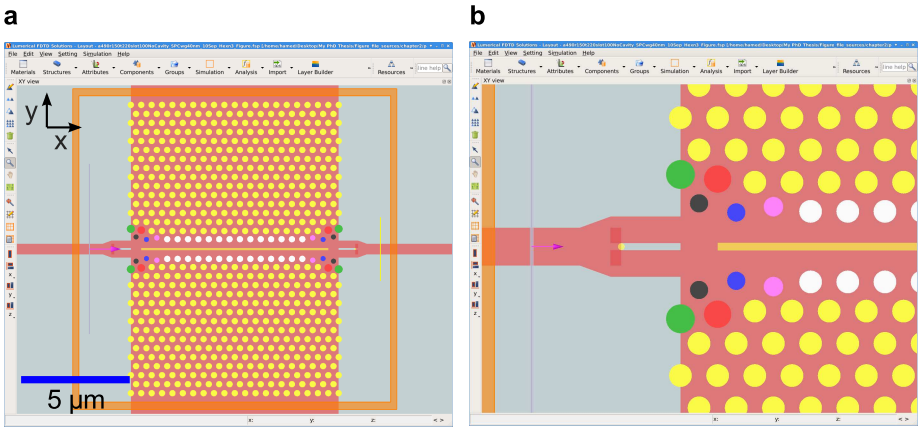

Figure 2.14: [(a)-(b)] The simulation layout of the optimized PCS waveguide in SC2 structure that offers higher transmission efficiency (no cavity exists in this simulation). The colored holes (other than yellow and white holes) have been modified to reduce insertion loss. The radius of the holes (r) and their distance from slot center (y) are optimized using FDTD simulations. For black holes $r = 120$ nm, $y = 570$ nm, blue holes $r = 120$ nm, $y = 450$ nm, pink holes $r = 128$ nm, $y = 526$ nm, green holes $r = 190$ nm, $y = 950$ nm, and red holes $r = 180$ nm, $y = 890$ nm. The rest of the nearest holes to the slot are shifted away from the slot by 40 nm with respect to their lattice point to make the PCS waveguide. All holes on the edge of the silicon slab will show up as half circles after fabrication (see Fig. 3.4d-e). The refractive index of these holes is the same as the background refractive index (n_{hex}), therefore having full holes on the silicon edge instead of half-holes does not change the simulation results.

and offers a desirable balance between efficiency and footprint. The transmission is further investigated by adjusting the position of the slot end, a, as plotted in Fig. 2.13(b). The transmission for a coupler that is 500 nm long ($L = 400$ nm and $a = 100$ nm) is 94%, and the coupling efficiency of light into the lowest order slot waveguide mode is 92% at $\lambda = 1550$ nm. The reciprocal coupling efficiency, for light propagation from the slot waveguide mode to the nanowire waveguide mode is also found to be 92% for the same coupler design. To simulate a solvent environment, as might be used in sensing or trapping applications, the background index of refraction, n, was changed from air to hexane ($n = 1.365$) and the new coupling

efficiency at 1550 nm is found to be 94%. The coupling efficiency is found to be $> 90\%$, over a 200 nm bandwidth centered at $\lambda = 1550$ nm, for both forward and reciprocal couplings in air and hexane.

To reduce the insertion loss from this adapter to the PCS waveguide in SC2 structure, the slot width of the Y-branch is increased to 90 nm and the *y*-coordinate and radius of 10 PCS waveguide holes (Fig. 2.14) have been modified. The radii and y-coordinates are optimized using FDTD simulations. The optimization of the radii and *y*-coordinates of the holes are done for one hole at a time to reduce the simulation time and the structure is symmetrical across the slot. The 3D FDTD simulation time for optimizing multiple design parameters has power-law dependence on the number of parameters to be optimized. Therefore, it is not practical to optimize the radius of all PCS waveguide holes simultaneously to find the least-power-dissipating design. As illustrated in Fig. 2.14, the order of optimization is black, blue, pink, green and finally red color holes.

Figure 2.15 shows the transmission efficiency of the optimized structure (a) is 14% higher compared with the case without any hole radii and location changes (b). More importantly, the transmission of the optimized structure (a) is significantly improved as opposed to the structure without the Y-branch adapter and hole modifications (c). The PCS waveguide transmission at the cavity resonance is increased from 19% to 59% indicating the benefit of Y-branch adapter and hole modifications. It is important to note that to obtain higher transmission efficiency in the optimized structure, the slot in the Y-branch is not connected to the slot in PC. A distance of 1 pitch (490 nm) was found to offer highest transmission.

Comparing this waveguide-only (no cavity) net transmission of 59% with that obtained in the corresponding SC1 design (Fig. 2.6), there is no net benefit. The reason is the difference of the adapting parts in the two designs. The improvement in the PCS waveguide transmission gets hindered by the lower transmission efficiency between the Y-branch adapter and PCS waveguide. Therefore, there is still no real advantage in the transmission efficiency of the waveguides in SC2 geometry. The real advantage in this SC2 configuration described in the next sub-section, when the transmission of the whole SC2 structure (waveguides plus cavity) is simulated.

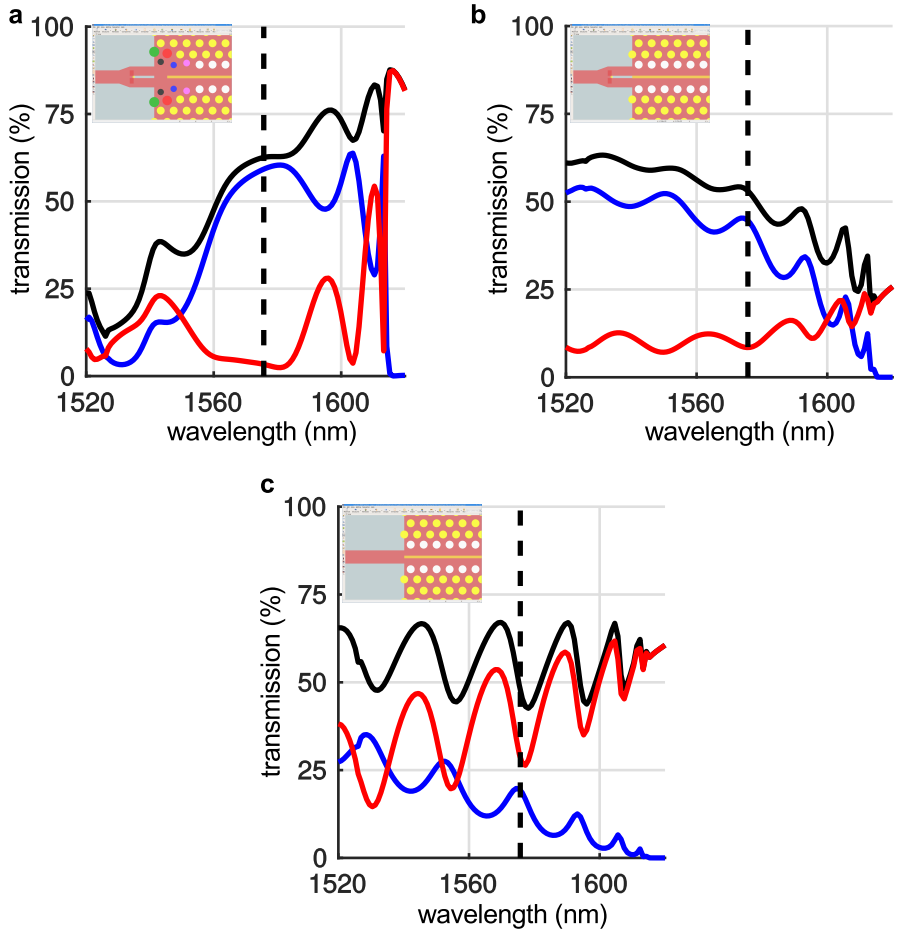

Figure 2.15: (a) Simulated transmission (blue), reflection (red) spectra, and the sum of them (black) calculated at the input and output channel waveguides of the structure in Fig. 2.14. (b) Simulated transmission (blue), reflection (red) spectra, and the sum of them (black) for the same structure without modification of the radii and location of the 10 holes at the entrance and the exit of PCS waveguide. (c) Simulated transmission (blue), reflection (red) spectra, and the sum of them (black) for the same structure as (b) without the Y-branch. The black dashed-line in these three figures is the resonance of Mode 1 of the modified cavity (Fig. 2.10c). The transmission of the improved structure in (a) at the cavity resonance is increased from 19% to 59% by using the Y-branch adapter and modifying the holes.

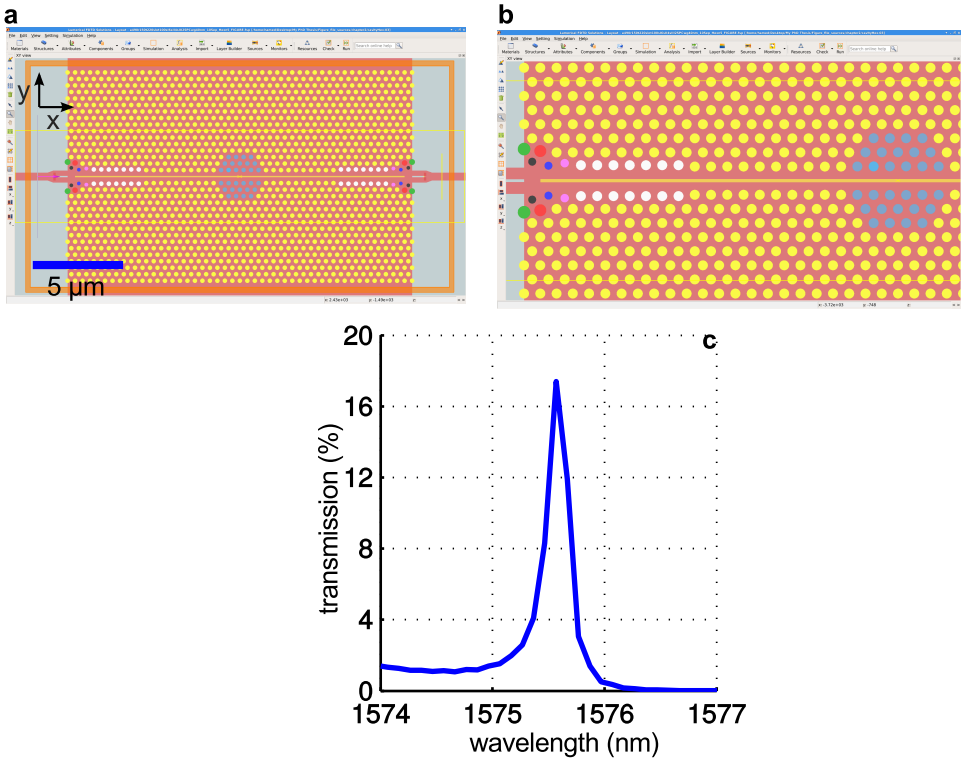

Figure 2.16: [(a)-(b)] Simulation layout for optimized SC2 PCS cavity. The holes in the PCS waveguide region have the same size and location as Fig. 2.14. There are 10 un-shifted holes in between the PCS waveguides and the cavity region (blue color holes at the center). The cavity hole shifts are $s_1 = 6$ nm, $s_2 = 4$ nm, $s_3 = 2$ nm. The hole radius for the regular PC holes is 150 nm. Slot width is 100 nm and the Y-branch adapting part between the single mode and PCS waveguide is explained in Fig. 2.12 except for the change of slot width to 90 nm. (c) The transmission efficiency of the full SC2 structure calculated using power monitor at the output channel waveguide. The Q of this loaded cavity is 8400 and its maximum transmission (although not completely resolved) is 17.5%.

2.3.4 SC2 Device Performance Discussion

Figure 2.16c shows the transmission efficiency of the SC2 structure including the cavity. This plot tells the real advantage of the butt-coupling structure over the original SC1 design (i.e. Fig. 2.4), which is due to better coupling between the PCS waveguides and the cavity mode. The peak transmission efficiency of SC2 in Fig. 2.16c is 17.5%. Considering the loaded and unloaded Q factor of SC2 cavity design, the transmission through the cavity is approximately $T = (\frac{Q_U - Q_L}{Q_U})^2 = (\frac{18500-8400}{18500})^2 = 30\%$. Therefore, knowing the efficiency of the waveguides in SC2 design (i.e. 59%), one can estimate the coupling efficiency from the PCS waveguides to the cavity. This number for SC2 design is $\sqrt{\frac{17.5\%}{30\% \times 59\%}} = 98\%$, which means only 2 percent of the power that reached the end of the input PCS waveguide is dissipated and reflected in the coupling region between the input PCS waveguide and the cavity. This number is significantly lower compared to the 23% lost in each of the coupling holes of SC1 design, which confirms the effectiveness of the butt-coupled geometry. Both the cavity Q factor and the transmission peak have been enhanced for the SC2 design and the optical trapping potential profile of the SC2 cavity illustrated in Fig. 2.17 quantifies the improvement in the trapping ability of this design.

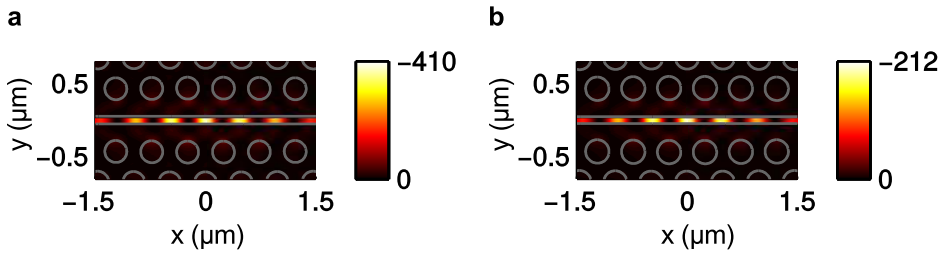

Figure 2.17: (a) The trapping potential calculated for Mode 1 of SC2 cavity in Fig. 2.16 on a 50 nm diameter Au nanosphere. (b) The optical trapping potential of mode 1 of SC1 cavity design described in Fig. 2.4 on a 50 nm diameter Au nanosphere. The injected power in the input channel waveguide for both figures is 1 mW and the unit of the colorbar is in $k_B T$.

2.3.5 1D Grating Coupler (SC2 device)

To slightly increase the amount of coupled power into the PCS cavity, a new 1D grating coupler has been designed for the SC2 structure using the optimization method described in [121, 122], which has three benefits: 1) because of its 1D structure, its optimization can be done using 2D FDTD simulations, which are much faster than full 3D simulations, 2) it gives rise to a few percent higher transmission efficiency and 3) its operation bandwidth is larger than the SC1 grating coupler design, which is useful for some applications. The optimized parameters and the corresponding transmission spectra are shown in Fig. 2.18.

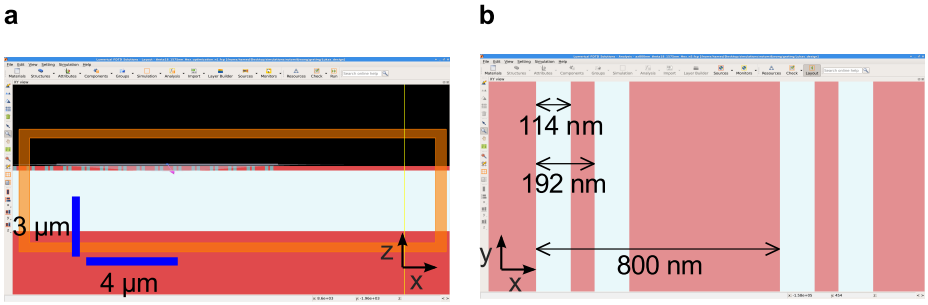

Figure 2.18: (a) 2D FDTD simulation layout for optimization of 1D double-tooth grating coupler. Instead of having partly etched trenches, a double-tooth geometry is chosen for easier fabrication. The optimization parameters are the teeth spacing (t), the period (a) and trench width (w). All three parameters are optimized at the same time within reasonable amount of simulation time. (b)The optimized values are $t = 192$ nm, $a = 800$ nm, $w = 114$ nm as shown in the figure.

2.4 Conclusion

In conclusion, we have reported the design of two different silicon-based photonic integrated circuits (SC1 and SC2) consisting of a PCS cavity, waveguides and grating couplers, operating at telecommunication wavelengths in a fluidic medium. The structure was designed to offer a robust means to enhance electric field intensity and hence light-matter interactions at a precise location inside a fluidic medium, while minimizing fabrication complexity and maximizing ease-of-use.

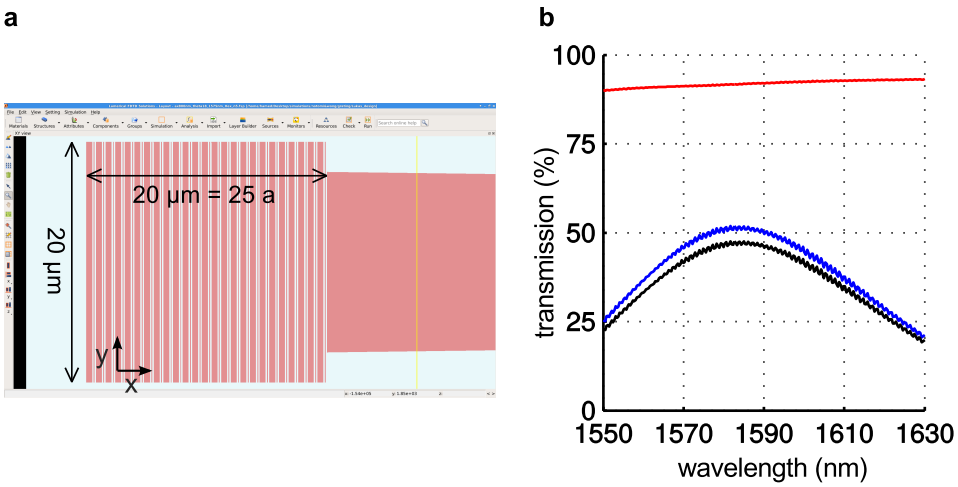

Figure 2.19: (a) Final optimized double-tooth grating design (for SC2 devices) connected to a tapered waveguide. The grating area is 20 μm $\times$ 20 μm. (b) The transmission efficiency of optimized double-tooth design from a Gaussian focused source to the beginning of the tapered waveguide (blue). The peak transmission value is 52% and FWHM is 75 nm. The excitation angle with normal to silicon surface is 18°. The transmission from tapered waveguide to the channel waveguide is shown in the black curve. Dividing the two curves gives the transmission efficiency of the waveguides that is improved compared to the red curve in Fig. 2.3c thanks to better wavefront shape matching between the double-tooth grating and the waveguides.

3D FDTD simulations demonstrate that such circuits, exhibit Q factors > 7500 and mode volumes as small as $V \sim 0.1(\frac{\lambda}{n})^3$, with resonant transmission as high as $T \sim 17\%$ (from input channel waveguide to output channel waveguide), when operated in hexane. These structures theoretically have the ability to easily trap 50 nm Au particles with modest coupled power of 1 mW (the maximum power our laser can deliver) in the channel waveguide. In fact, for the improved SC2 design, Mode 1 produces theoretically provides the required $10k_BT$ trapping potential for particles as small as 15 nm in diameter with just 1 mW of coupled laser power. A summary of the performance of the two designed devices are presented in Table 2.1.

The SC2 design shows improved performance, compared to the SC1 structure,

Table 2.1: Summary of the transmission efficiency of different parts of SC1 and SC2 designs for the Mode1 of the PCS cavity. The second column shows the peak transmission efficiency of grating couplers. The third column is showing the FWHM of the grating couplers. The fourth column summarizes the transmission of the reference devices in Fig. 2.6 and Fig. 2.14. The fifth column is the coupling efficiency from the end of the input PC(S) waveguides into the PCS cavities.

Design name	GC peak transmission (%)	GC FWHM (nm)	Channel to PC/PCS to channel WG transmission (%)	PC/PCS WG to cavity transmission (%)	Unloaded Q	Loaded Q
SC1	50	50	67	77	9600	7400
SC2	52	75	59	98	18500	8400

thanks to its butt-coupled geometry and higher Q factor. The main advantage of the butt-coupled geometry is the better matching between the mode profiles of the PCS waveguides and the cavity. It is possible to further improve light confinement in these structures by modifying the PCS cavity structures. For example, by shifting more than 3 rings of holes around the cavity center and optimizing their sizes and locations, it is possible to create more gradual perturbation to the PCS waveguide modes thus causing less vertical loss in the cavity. Also, if the fabrication limitation allows it, reducing the slot width causes more field-enhancement in the slot as discussed in [112] and [21].

Chapter 3

Device Characterization And Sensing Application

3.1 Introduction

The first part of this Chapter describes the photonic chip layouts, chip fabrication process and the transmission set-up used for measuring the transmission of devices detailed in Chapter 2. This is followed by a comparison of the experimental and simulated transmission spectra of a few fabricated devices.

3.2 Chip Layout

The chip layouts for fabricating photonic chips are generated using Mentor Graphics software and exported in "*.gds*" format to University of Washington Microfabrication Facility, a member of the NSF National Nanotechnology Infrastructure Network [4], for fabrication. In the following two sub-Sections, the layout of two chips, on which all measurements in this thesis are done, is described in detail. In creating layout files, different device feature sizes are bracketed over a certain range. This design strategy guarantees that despite the unavoidable fabrication imperfections, at least a few devices will possess the expected feature sizes and operate as expected. The first chip layout is based on the SC1 device described in Chapter 2 and the second chip layout contains SC2 structures.

Table 3.1: The feature sizes for SC1 devices that are used in chip EB312 layout.

Grating coupler hole radius (nm)	PC hole radius (nm)	slot width (nm)	coupling hole radius (nm)
$230, 250, 270$	$150, 160, 170$	$70, 90, 100$	$80, 110, 140$

3.2.1 Chip EB312 Layout (SC1 design)

In the chip layout demonstrated in Fig. 3.1, the grating couplers are similar to the ones illustrated in Fig. 2.3 (i.e. with 795 nm and 750 nm pitches along x and y axis) and the cavity structure is similar to Fig. 2.4 (i.e. with pitch size of 490 nm). The four bracketed features that are varied across this chip layout are summarized in Table 3.1.

These features each have 3 different possible values, resulting in a total of $3^4 = 81$ devices for this chip layout. These 81 devices are grouped into 9 arrays of 3×3 devices with each given a row and a column label. The devices in each of these 9 groups have the same radius for grating coupler and photonic crystal cavity holes. In each group of 9 devices, the slot width and coupling hole radius vary along that group's column and row device axes, respectively (see Fig. 3.1). Going from one group of devices to another, the grating coupler hole radius varies along the group row axis while the PC hole radius varies along the group column axis. The group row and column number are located on the left side of each group (see Fig. 3.1b-d). The labels are formed from two column of squares; the number of squares in the left column specifies the group row number while the number of squares in the right column specifies the group column number. For example, the label of the group shown in Fig. 3.1c is row 4 and column 1. In this thesis each specific device is referred to in the following format; "*chip name + R + group row number + C + group column number + (device row number, device column number)*". For example the device in the top-left corner of the group shown in Fig. 3.1c is referred to as "*EB312R4C1(3,1)*" and the device just below it is referred as "*EB312R4C1(2,1)*".

Other than the 9 groups of devices described above, the chip also includes 3 groups of reference devices that were designed for measuring the waveguide

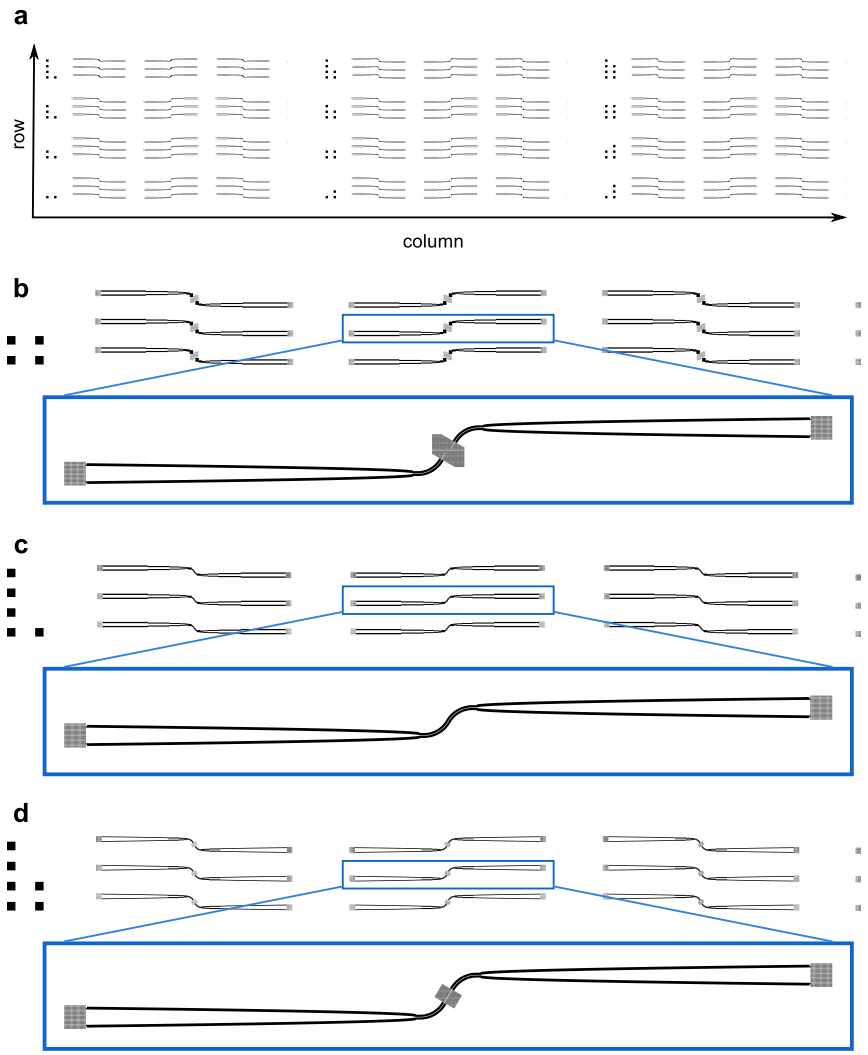

Figure 3.1: (a) Layout of the Chip EB312 based on SC1 designed described in Chapter 2. There are 12 groups of 3×3 devices on this chip. The row and column label of each group is located on the left side of the group. (b) Group EB312R2C2 consists of devices that are full SC1 structures. (c) Group EB312R4C1 consists of devices with no photonic crystal in between the channel waveguides. (d) Group EB312R4C2 consists of devices that have only grating couplers, tapered, channel and photonic crystal waveguides without any PCS cavity in between them.

transmission efficiencies (i.e. no PCS cavities exist in these devices). Group EB312R4C1 (Fig. 3.1c) contains devices with only a channel waveguide between two tapered waveguides. The grating coupler hole radius varies along the device row axis but there are no features bracketed along the device column axis of this group. The other two groups EB312R4C2 and EB312R4C3 are identical (see Fig. 3.1d) and each of them consists of 9 devices each with a W1 photonic crystal waveguide but without the usual cavity in the middle. In these two groups, the grating coupler hole radius varies along the device row axis and the photonic crystal hole radius varies along the device column axis. The length of the photonic crystal waveguides are identical to the length of input plus output photonic crystal waveguide in a full SC1 device.

3.2.2 Chip EB485 Layout (SC2 design)

This chip (Fig. 3.2) is based on the improved SC2 design described in Chapter 2. Since the double-tooth grating coupler is periodic in one-dimension (1D), it can be simulated with relatively good accuracy in 2D FDTD simulations, which are very short. Therefore, optimizing this structure to find best performance can be done quickly. As a result, instead of bracketing over all 3 feature sizes of this grating coupler (i.e. period (a), tooth spacing (t) and tooth width (w)), which requires fabricating many devices and increased fabrication costs, all three parameters were optimized at the same time to find 3 grating designs that operate with 3 different central frequencies. Using FDTD simulations and following the same steps as described in Chapter 2, all three grating parameters are simultaneously varied for optimized operation at three wavelengths of 1550 nm, 1575 nm and 1600 nm. These wavelengths are selected based on previous fabricated devices that demonstrated that fabrication imperfections (mainly in the size of the grating coupler features like hole diameter, etc.) may cause up to a 40 nm mismatch between the central wavelengths of simulated and fabricated grating couplers. Therefore, these three different grating designs maximizes the likelihood that at least one set of grating parameters would work in the range of the excitation laser (1520 nm - 1630 nm). The incident laser angle with the normal of the grating coupler plane is kept at 18° in designing all three gratings.

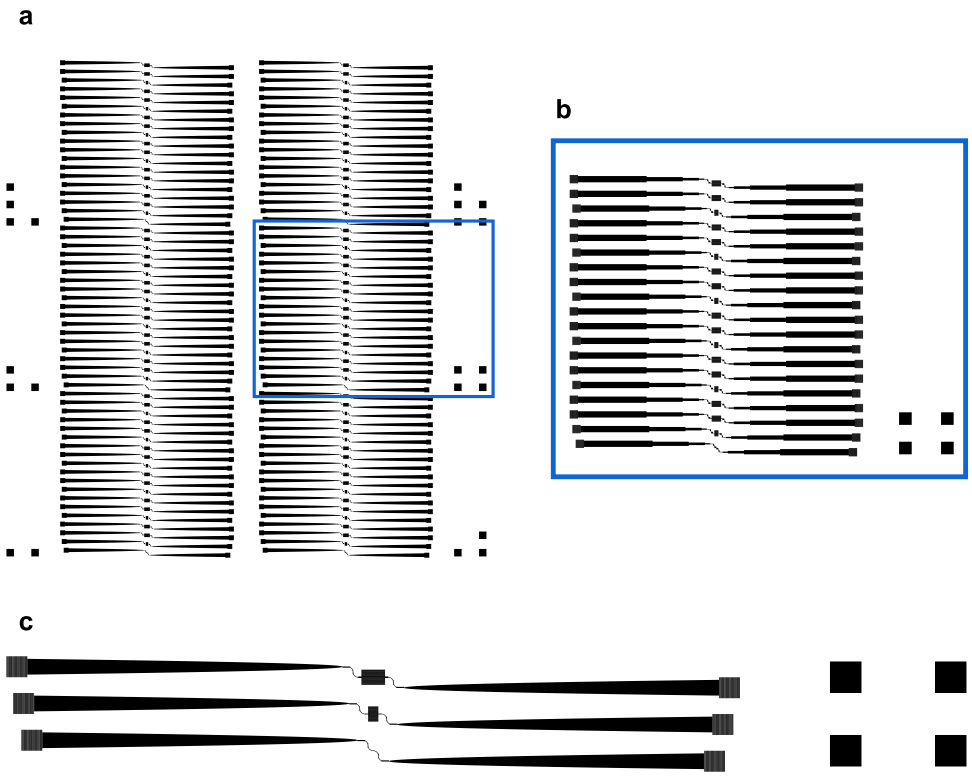

Figure 3.2: (a) Layout of the Chip EB485. There are 6 groups of 19 devices on this chip. In each group there are 12 SC2 devices along with 7 reference devices that do not have cavity in them to let us test the efficiency of other elements of SC2 photonic circuit. (b) Zoomed out layout of group EB485R2C2. The 4 squares on the right side of the devices are showing the label of the group. (c) The layout of the first 3 devices of group EB485R2C2, which show two reference devices for measuring the transmission of the grating couplers and waveguides and one full SC2 device that include PCS cavity.

Table 3.2: The feature sizes for SC2 devices that are used in chip EB485 layout.

Double-tooth grating coupler parameters (nm)			PC hole radius (nm)	Slot width (nm)	PCS waveguide length (pitch)
a	*t*	*w*			
793	204	124	140, 150, 160	90, 100	9, 10
800	192	114			
803	223	120			

The grating parameters and three other bracketed features corresponding to the cavity region are shown in Table 3.2. The 3 grating coupler designs, 3 photonic crystal hole radii, 2 slot widths and 2 different lengths of PCS waveguides yield 36 devices in the chip layout. For the devices with photonic crystal hole radius of 150nm, the radii of the modified holes at the entrance of the PCS waveguides are the same as described in Fig. 2.14. However, when the radius of the regular photonic crystal holes changes to 140 nm or 160 nm, the modified hole radii vary with the same relative percentage change. Similarly, when the slot width is 100 nm, the width of the slot in the Y-branch is 90 nm (see Fig. 2.16) but when the slot width changes by 10% to 90 nm the Y-branch slot width changes with the same percentage amount to 81 nm. Since the total length of the photonic crystal lattice is kept fixed, by changing the PCS waveguide length, the distance between the end of the PCS waveguides and the cavity varies. This allows control of the coupling between the cavity and PCS waveguides which determines the loaded cavity Q factor.

Figure 3.2 shows that Chip EB485 has 6 groups with 19 devices in each of them. Each group is identified with a label that shows its group row and column number (similar to EB312 chip). The right and left half of chip EB485 are identical. Devices in one group have the same grating coupler parameters and these parameters vary from one group to the other. Each specific device on this chip has a name in the format "*chip name + R + group row number + C + group column number + n + device number counted from bottom of a group*". For instance, the third device from the bottom of the group shown in Fig. 3.2b, is named "*EB485R2C2n3*".

The first device in each group (i.e. device n1) does not have a photonic crystal

and is for measuring the transmission efficiency of the grating couplers and tapered and channel waveguides. There are another 6 reference devices in each group (n2, n5, n8, n11, n14, n17) that do not have any cavity in between PCS waveguides for measuring the PCS waveguide transmission efficiency. Devices n2, n5 and n8 in each group have similar slot width (90 nm) but different photonic crystal hole radii. Similarly, devices n11, n14 and n17 have the same slot width (100 nm) but varying photonic crystal hole radius. In between each of these 6 reference devices, two full devices (i.e. devices that have cavities) exist which have identical feature sizes except for the length of their PCS waveguides. The common feature sizes of these two full devices are identical to the reference device (i.e. the device with a PCS waveguide by no cavity) underneath them. For example, devices n3 and n4 have the same slot width and photonic crystal hole radius as device n2 and in the same way devices n6 and n7 have the same slot width and photonic crystal hole radius as reference device n5. To summarize, in total each group has 12 full SC2 devices, which, along with the other 2 groups in their column, account for all 36 combinations of feature sizes.

3.2.3 Fabrication

The photonic chips are fabricated [4] using a 100 keV JEOL JBX-6300FS electron beam writing system. ZEP-520A resist (Nippon-Zeon Co. Ltd.) for chip EB312 and hydrogen silsesquioxane resist (HSQ, Dow-Corning XP-1541-006) resist for chip EB485 served as the etch mask. It is absolutely crucial to set the shot pitch[4] for the electron beam lithography at most equal to the minimum hole shift in the cavity region (i.e. 4 nm for SC1 design and 2 nm for SC2 design). Otherwise the cavity will not appear in the final fabricated photonic crystal. The beam current for patterning these chips is 1 nA. Etching was done using an Oxford PlasmaLab System 100 with chlorine gas. The complete circuit requires only one lithography step and one etch step.

Figure 3.3 shows the grating coupler and cavity region of a SC1 device on chip EB312 (layout in Fig. 3.1), while Fig. 3.4 shows some of the devices that were fabricated on chip EB485 with the layout shown in Fig. 3.2. The radius of the photonic crystal holes are within 7 nm of the designed values. Before using the fabricated

chips, they are rinsed with various organic solvents (acetone, methanol and isopropanol (IPA)) to remove any leftover resist residue from their surface. If some resist remains after rinsing, the chips can be illuminated with UV light for a few minutes and then rinsed with acetone to completely remove them. Thereafter, it is often necessary to clean the chip again to ensure optimal operation especially after experiments where the chip surface is exposed to sources of organics and nanoparticles (i.e. after trapping experiments). Depending on the experiment, more aggressive cleaning processes are needed such as Piranha [1] and Aqua Regia [2]. Piranha is required for cleaning heavy organic contamination and Aqua Regia is necessary for dissolving Au particles. Although it is possible to remove organic contamination with the less aggressive "*RCA*" cleaning method [3], due to the fact that RCA results in oxidization of the silicon slab which can blue-shift cavity resonances by up to about ~ 7 nm, a combination of Piranha and Aqua Regia (less than a nanometer blue shift for each run) is recommended instead.

3.3 Measurement Setup

3.3.1 Liquid Cell

To perform measurements in a highly volatile fluidic medium, a leak-free demountable liquid cell (Harrick Scientific Products [4]) (Fig. 3.5) is used to immerse the silicon chip in solution. Specifically, hexane is more challenging to use than other

[1] For Piranha etch, H_2SO_4 is slowly mixed into H_2O_2 with $5:1$ ratio in a **glass** container. The container is placed on a hotplate until its temperature reaches 100°C. Then the chips are placed into the solution with a pair of **Teflon** or **stainless steel** tweezers for 15 minutes, maintaining the temperature between 100°C and 110°C. Once finished, the container is removed from the hotplate and the chip is removed and rinsed with Deionized Water (DI) water. Piranha etch is an extremely dangerous process and needs proper training and safety equipment to perform.

[2] After Piranha etch, if the sample was used for trapping with Au particles, the Aqua Regia process is necessary to clean the Au particles stuck on the chip surface. The Aqua Regia preparation involves mixing two strong acids; nitric acid (HNO_3) into hydrochloric acid (HCl) with $1:3$ molar ratio. The reaction is very exothermic and produces poisonous vapors which require proper ventilation and strict safety protocols during usage. Chips covered with Au nanoparticles are soaked in Aqua Regia for 5 seconds and rinsed with DI water afterwards. It is important to not leave the chip in Aqua Regia for more than a few seconds to minimize silicon oxidization which will affect the performance of the devices on the chips.

[3] http://www.nanofab.ubc.ca/processes/cleaning/rca-1-si-wafer-cleaning/

[4] http://www.harricksci.com/ftir/accessories/group/Demountable-Liquid-Cells

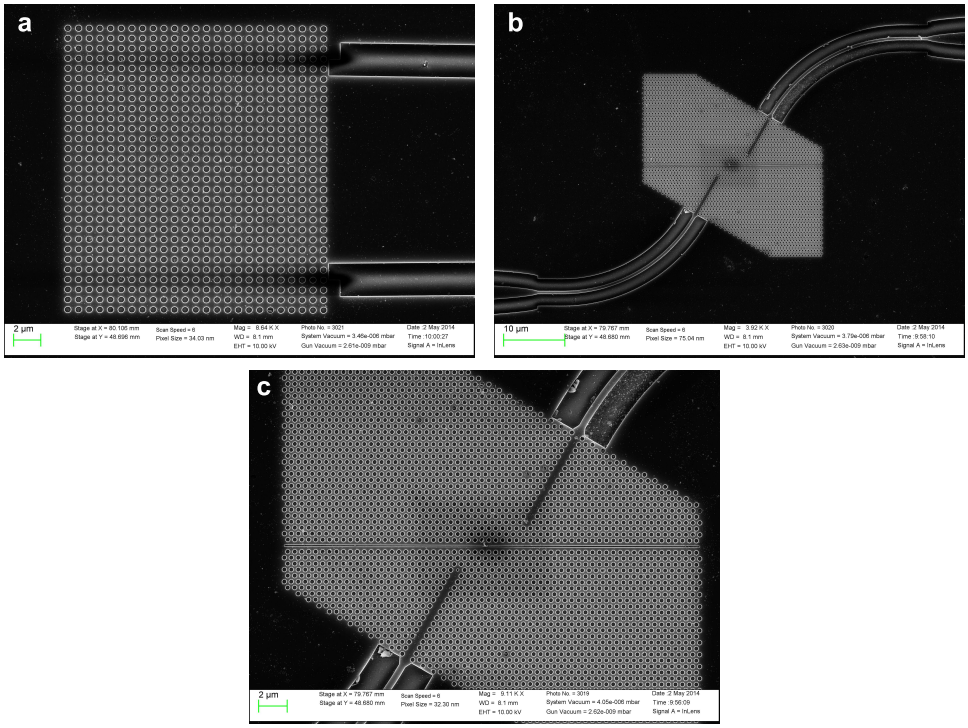

Figure 3.3: SEM image of a fabricated (a) grating and [(b)-(c)] cavity on chip EB312. Blackened areas are due to electron-beam-induced carbon deposition on the chip during SEM imaging.

solvents because it is highly volatile and also much more reactive to different types of sealant (like tapes, vacuum grease, rubber cement, etc.). Therefore, using the typical glass cuvettes with loose fitting Teflon caps was neither appropriate nor safe for optical measurements of the chip in solvents like hexane. Figure 3.5b shows all different parts of the liquid cell used for the measurements presented in this thesis. The photonic chips are placed in between the quartz windows, where two 1 mm spacers are located to create a small volume for immersing the chip in solution. Another benefit of that liquid cell is the possibility of doing experiments in a flow condition by connecting Teflon tubes and syringes to the cell. This setup would enable measurements with time-varying concentration of nanoparticles in the future. Using the same cleaning procedure as above, the glass windows and the caps of this cell are cleaned after each round of experiments that result in contamination.

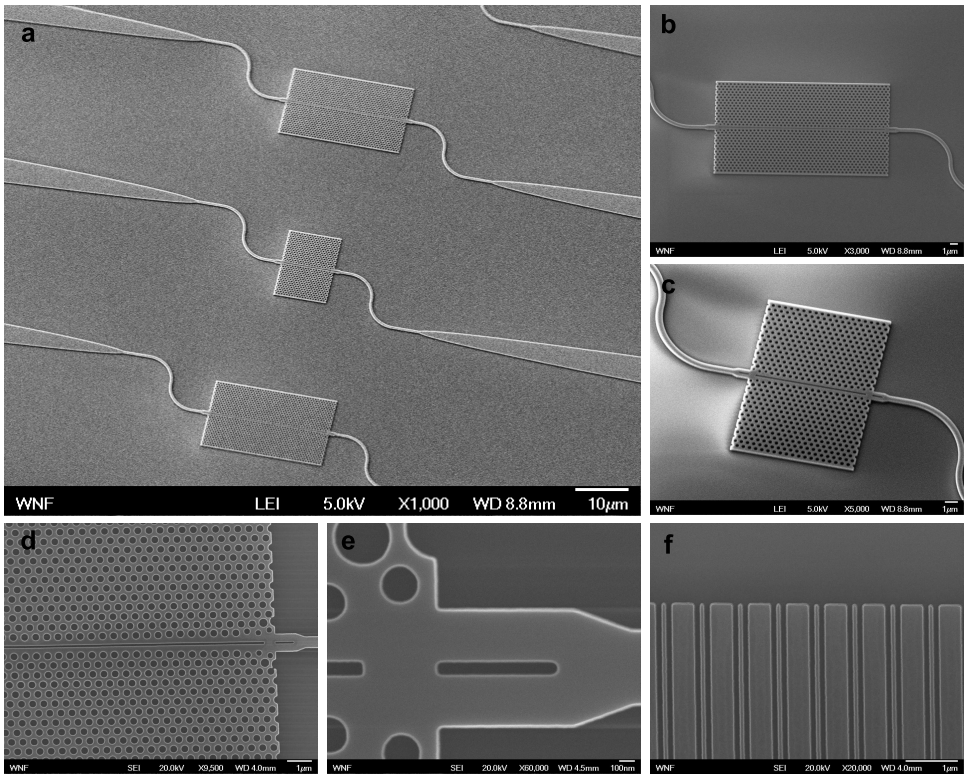

Figure 3.4: (a) SEM image of the fabricated chip EB485 [4]. (b) Picture of a full SC2 device, (c) a device without a cavity in between PCS waveguides, [(d)-(e)] adapting parts and (f) a double-tooth grating coupler.

3.3.2 Transmission Setup

The experimental setup, which was mainly built by Ellen Schelew [22] for device transmission measurements, is shown in Fig. 3.6. The chips containing devices are placed inside the liquid cell and the cell is mounted on top of a rotation stage. The position of the cell is adjusted using x-y translational stages to place it at the center of the rotation stage. The devices are excited using a tunable diode laser (Newport TLB-6600 Venturi) with the wavelength range of 1520 nm to 1630 nm and a maximum power of 9.5 mW. The laser source is guided through an optical fiber (blue line in Fig. 3.6) into an optical system consisting of a polarizer and a

[5]http://www.harricksci.com/ftir/accessories/group/Demountable-Liquid-Cells

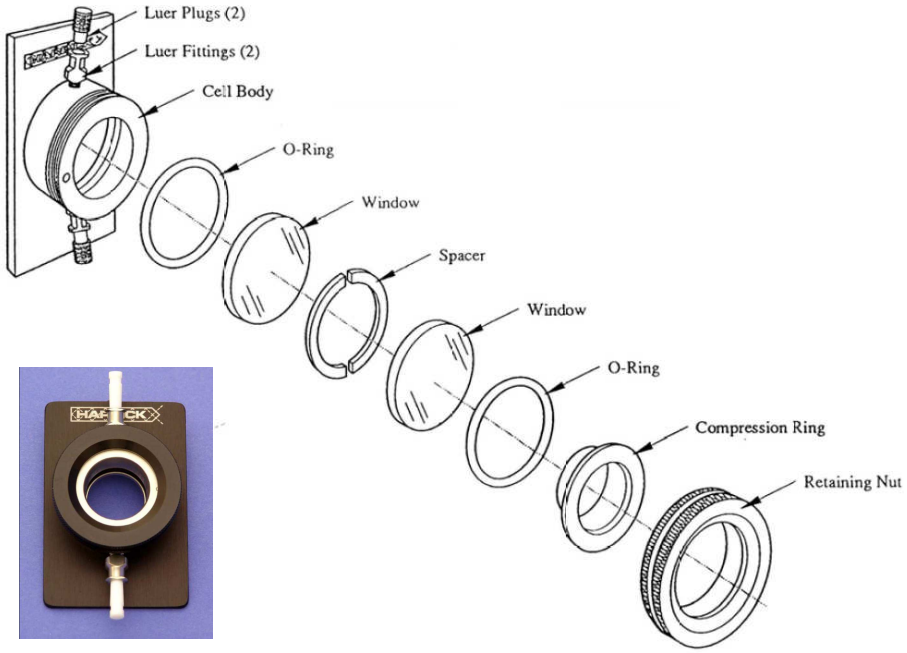

Figure 3.5: The structure of the liquid cell (Harrick Scientific Products [5]) used for immersing the chips in a liquid medium (reprinted from manufacturer's website), composed of a pair of quartz glass window separated by two half-ring Teflon spacers between which the photonic SOI chip is placed during measurements. Once assembled the volume between the windows is filled with solution.

set of lenses that focuses laser light on the devices in the cell. The optical system is also sitting on a concentric rotation stage. This rotation stage along with the cell's own rotation stage enable us to control the angle between the incident and transmitted beam. The focused laser light is incident on the input grating coupler of a device and the transmitted light gets out-coupled from the output grating coupler toward an elliptical mirror that focuses the output light on its second focal point, where an InGaAs photodiode power meter (Model 818-IG from Newport Inc.) is located. The power meter can be swapped with a ElectroPhysics Microviewer (Model 7290A) CCD camera for imaging and alignment purposes. The reflected light from the elliptical mirror is redirected using a second flat mirror and passed

through a cross-polarized polarizer that filters the unwanted scattered light from chip surface. The elliptical mirror has focal lengths of 15 cm and 150 cm, which results in 10$\times$ magnification. The devices are at the first focus (15 cm distance) of the elliptical mirror and the magnified image of the devices, which is formed on a CCD camera, is at the second focus (150 cm distance). The light path is shown by orange dashed lines in Fig. 3.6. A Labview [123] program operates the laser and records the data via a General Purpose Interface Bus (GPIB) controller from the power meter. For measuring transmission spectra, it sweeps (rate of 100 nm/s) the laser through a 10 nm range of wavelengths and upon receiving the trigger signal from the laser, which indicates the start of the sweep, the program starts recording output of the power meter (sampling rate of 10 kHz)to create the transmission spectra.

3.4 Experimental Characterization

After receiving the fabricated chips, the transmission efficiencies of different devices were measured. The results of the transmission measurements are summarized in the next two sub-Sections. The first sub-Section summarizes measurements corresponding to devices on chip EB312 which are based on the SC1 design while the following sub-Section details the chip EB485 measurements which are based on the SC2 design. All of the experimental characterization in this Section was performed when the chips were immersed in pure hexane.

3.4.1 Chip EB312 Measurements

The first test for a newly fabricated chip is measuring the transmission spectra of devices with no photonic crystal in between grating couplers. This step determines whether the grating couplers are operating in the laser range or not. Figure 3.7 shows measurement of three nominally identical devices versus the simulation result. It is clear that the three devices are performing similarly in terms of peak transmission, central wavelength and bandwidth. But the agreement between simulation and experiment is poor as demonstrated by the $\sim$ 35 nm difference between the simulated and measured central wavelength. This suggests that systematic size differences exist between the fabricated grating couplers and their original design.

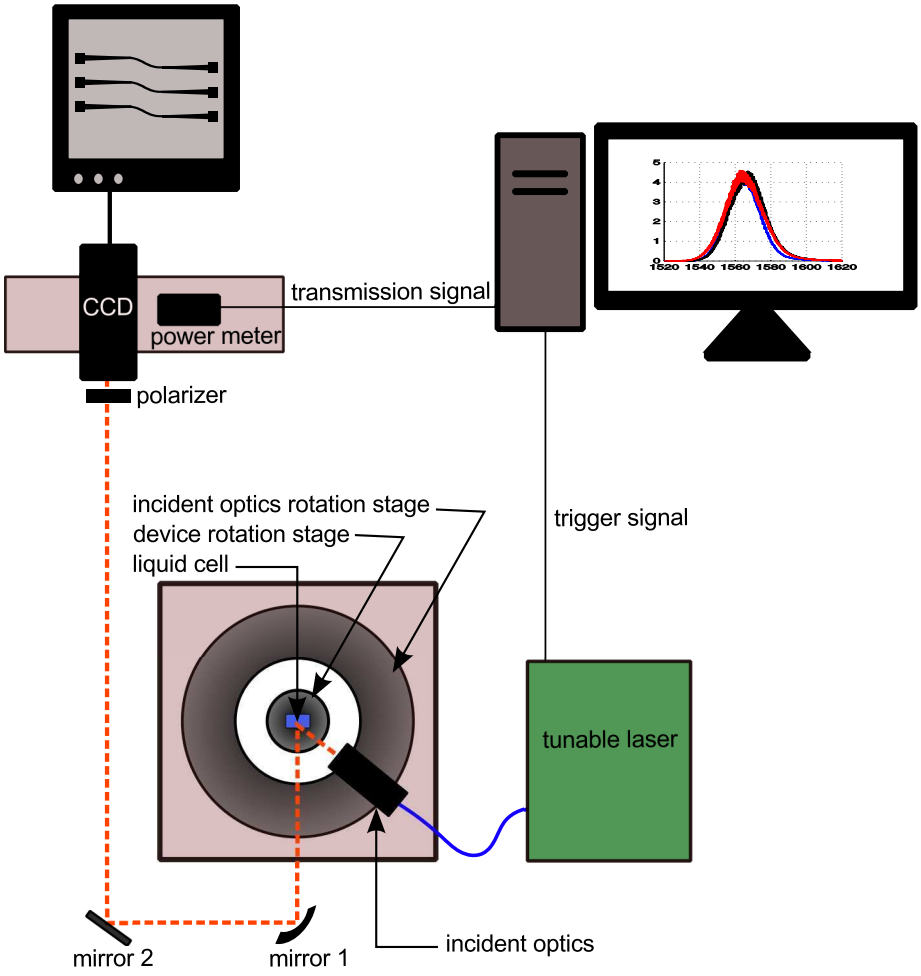

Figure 3.6: The top-view of the experimental setup used for transmission measurements and optical trapping experiments. The rotation stages allow the angle between the incident light and the surface of the chip to be varied, which is necessary for optimal coupling to grating couplers at different wavelengths. The excitation optics include a polarizer and two plano-convex lenses held in a lens tube. One of the lens collimates the laser beam coming out of a single mode optical fiber (blue line in the figure) and the second lens focuses it on the chip. This one-to-one focusing system results in focusing the laser light to the same size as the beam at the output of the single mode optical fiber ($\sim$ 10 μm).The detailed description of this experimental setup is explained in Ref. [22].

After measuring hole radius of some of the fabricated grating couplers using SEM images, it was discovered that the grating couplers radii are $\sim$ 15 nm smaller than the designed values. This is consistent with a subsequent FDTD simulation of a grating coupler with 15 nm smaller radius, which shows a 40 nm red shift in the central wavelength of grating coupler spectra (Fig. 3.7b).

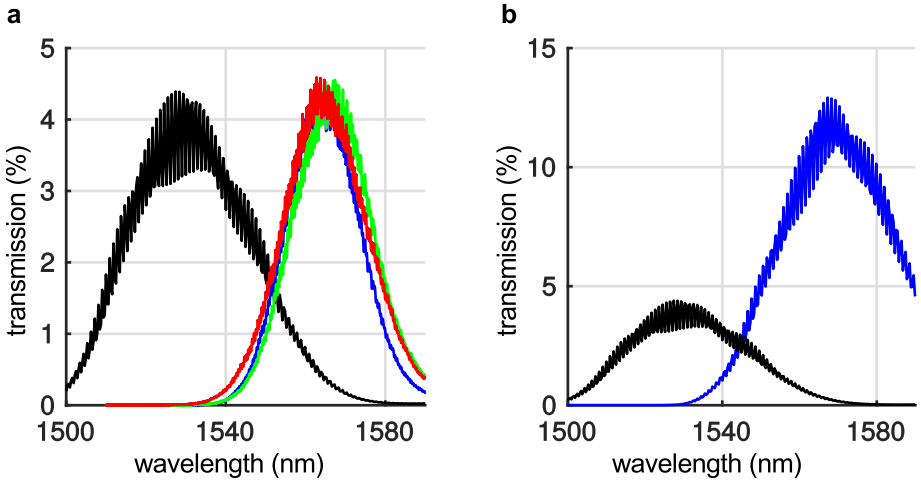

Figure 3.7: (a) Simulation (black) versus experimental transmission efficiency of device EB312R4C1(2,1) (green), EB312R4C1(2,2) (blue), EB312R4C1(2,3) (red). These transmission are from input grating coupler to output grating coupler through the channel waveguide. The incident angle of the laser with the grating surface normal is 18° for both simulation and experiment. (b) Black curve is the same curve as in (a) and the blue curve is the simulated transmission spectra when the radius of the grating holes is reduced by 15 nm to 135 nm.

The Fabry-Perot reflections between input and output grating couplers create a periodic modulation of the transmission spectra which can be seen as fluctuations at the transmission peak in Fig. 3.7. The period of these fluctuations is $\sim$ 0.5 nm, which agrees very well with the $\sim$ 650 μm distance from input to output grating coupler. Also, the amplitude of these Fabry-Perot fringes is small relative to the peak of the transmission spectra, which is advantageous for having fairly uniform transmission values during operation in a short range of wavelengths.

The next step in characterization of the chip is measuring the transmission

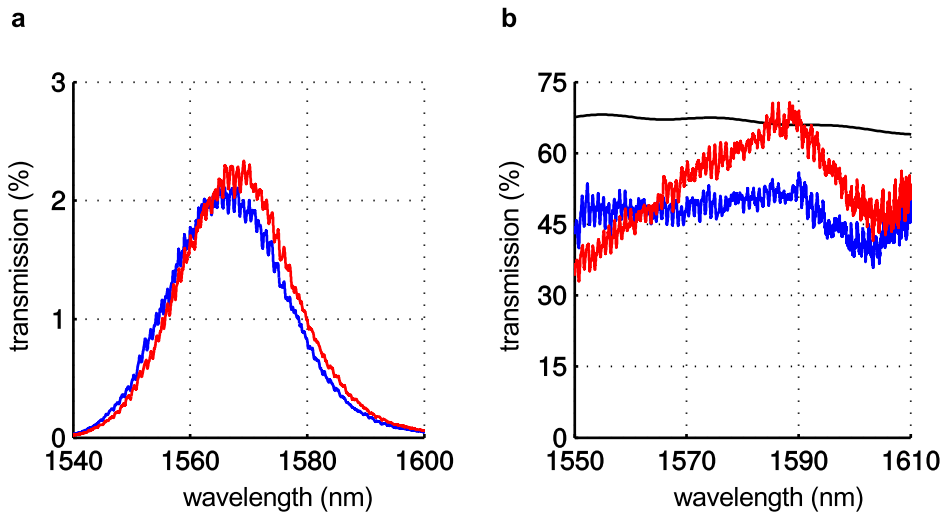

Figure 3.8: (a) The experimental transmission spectra of two nominally identical devices that have photonic crystal W1 waveguide without any cavity in between them. The blue curve is for the device EB312R4C2(2,2) while the red is for EB312R4C3(2,2). These transmission values are for the full devices (i.e. grating couplers and photonic crystal waveguides). (b) Simulation (black) versus experimental transmission spectra (blue and red) from input channel waveguide through the photonic crystal W1 waveguide to the output channel waveguide. These experimental curves are the result of dividing transmissions in (a) by the transmission of device EB312R4C1(2,1) (green curve in Fig. 3.7).

spectra of devices with a photonic crystal W1 waveguide but no cavity in them. Figure 3.8 (a) shows two experimental transmission spectra of this type of device, which are performing similarly. By dividing the transmission of these devices by the transmission of devices in Fig. 3.7, the performance of the photonic crystal W1 waveguides can be studied separately. When the spectra are divided, the Fabry Perot fringes in the spectra of the grating coupler reference devices is filtered out so the only the Fabry Perot effect of the photonic crystal waveguide devices is included in the division result. Figure 3.8 (b) shows that the fabricated devices are $\sim$ 20% less efficient compared to what the FDTD simulation predicted and suggests some size differences exist between fabricated and designed features. SEM images of the photonic crystal holes in this chip confirm that the fabricated devices

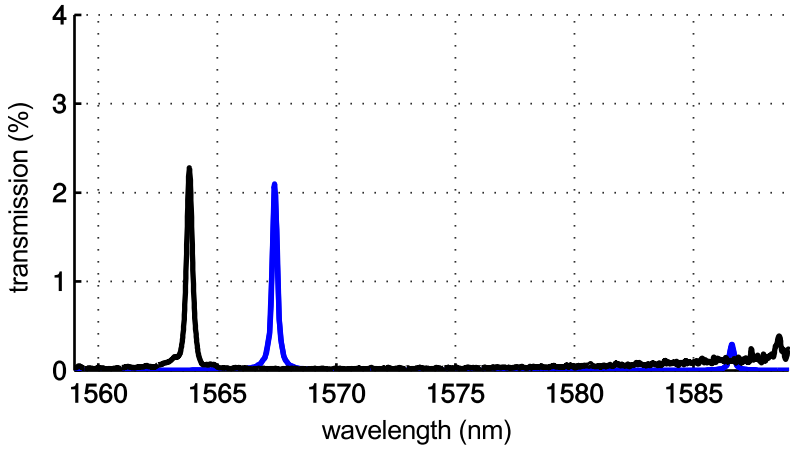

Figure 3.9: Resonant transmission spectra from input to output ridge waveguides through slot-cavity for device EB312R22(2,2) in Table 3.3. The simulation curve is in blue and the experimental curve is in black.

have on average 7 nm smaller PC hole radii compared to the designed values.

Finally, Fig. 3.9 shows the experimentally measured transmission spectrum through a full-structure device (EB312R22(2,2)), in hexane, on an absolute scale (left curve). To make a correspondence with simulated transmission from input ridge waveguide to output ridge waveguide (through the cavity), these cavity transmission spectra are normalized by the transmission measured through identical reference devices where the entire PC region is replaced by a simple continuation of the ridge waveguide (i.e. devices in Fig. 3.7). The agreement between the experimental and simulated spectrum for this device is one of the best among all measured full device on this chip. Table 3.3, summarizes the measured and simulated parameters for 5 different full-structure devices (absolute transmission data only for 3 of the 5). Devices EB312R22(1,2), EB312R22(2,2) and EB312R22(3,2) differ only in the radius of the coupling hole. Both EB312R22(1,2) and EB312R22(2,2) yield good agreement with the simulations, while all parameters for device EB312R22(3,2) are noticeably different, indicating the presence of fabrication imperfections. EB312R22(2,2), EB312R22(2,1) and EB312R22(2,3) differ only in the width of the slot, and the predicted shift and change in Q value are in good agreement between experiment and simulation.

Table 3.3: Summary of the results from simulations and transmission measurements on 5 different devices. All of these devices are on chip EB312. The transmission values are from input channel waveguide to output channel waveguide. r_c is the nominal radius of the coupling hole at the end of W1 photonic crystal waveguides that controls the coupling of the waveguides to the cavities. s is the nominal width of the slot waveguide.

Device	s(nm)	r_c(nm)	Simulation			Experiment		
			λ (nm)	Q	$T(\%)$	λ (nm)	Q	$T(\%)$
R22(1,2)	90	80	1567.8	5640	4.8	1564.3	3800	3.1 $\pm$ 0.4
R22(2,2)	90	110	1567.8	7390	2.1	1563.9	6100	2.3 $\pm$ 0.3
R22(3,2)	90	140	1567.8	8480	0.49	1564.8	4400	0.29$\pm$ 0.08
R22(2,1)	80	110	1596	8900	–	1595.4	7650	–
R22(2,3)	100	110	1535.4	4720	–	1545.2	4400	–

These Q values are higher than those reported for cavities operating in solvents in Refs. [101, 114, 124] despite not having removed the silicon dioxide undercladding. Simulations suggest that by undercutting these cavities, the *intrinsic* (*i.e.* stand-alone, unloaded) Q value of the cavity in hexane should increase from 10×10^3 to 25×10^3 as compared to the hexane-over-SiO_2 structure studied here. As discussed in detail in Section2.2.3, the transmission values are limited partially by the fact that the W1 photonic crystal waveguide modes lie above the light line in these samples, and because the single-variable-hole coupler between the W1 waveguide and the slot waveguide causes excess scattering.

3.4.2 Chip EB485 Characterization

Chip EB485 consists of the improved SC2 structures and its characterization results are presented in this sub-Section. Similar to the previous chip, characterization starts with devices that only possess grating couplers and waveguides. Figure 3.10 shows the measurement for device EB485R2C2n1 versus the FDTD simulation

result. In this device the photonic crystal section is replaced with a channel waveguide to test the performance of the grating couplers and the tapered and channel waveguides. It is clear that this device is performing differently than the simulations due to differences between the fabricated and designed feature sizes. There is $\sim$ 20 nm difference between the central wavelength of the simulated spectra as compared with the experimental result and the peak transmission value is smaller by 50% in the fabricated device. However, the experimental peak transmission value of this double-tooth design is nearly 3 times higher than the previous grating design (Fig. 3.7), while keeping the Fabry-Perot reflection amplitude relatively small. Also, because the separation between input and output grating couplers is similar to SC1 device types, the Fabry-Perot fringes have similar wavelength spacing.

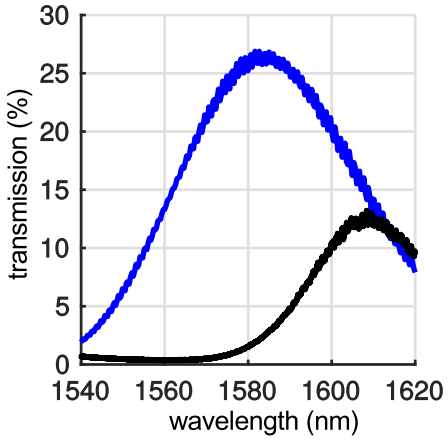

Figure 3.10: Simulation (blue) versus experimental (black) transmission from input grating coupler to output grating coupler through channel waveguide, for device EB485R2C2n1. The incident angle is 18°.

Next, devices with grating couplers, slab waveguides and PCS waveguides without cavities are tested. In Fig. 3.11, the performance of the PCS waveguide is tested. The overall shape of the measured spectra is in good agreement with the expected simulation result, however it is shifted by $\sim$ 13 nm, again due to differences between the fabricated and designed feature sizes. Although the double-branch adapter dissipates power in the butt-coupled configuration (see Chapter 2),

because of lower losses in the PCS waveguide the overall experimental transmission of the butt-coupled PCS waveguide is slightly improved compared with the previous PC W1 design (Fig. 3.8). This transmission efficiency comparison is based on the transmission at the cavity resonance wavelengths of Mode 1 of the two designs (i.e. Fig. 3.9 for SC1 design and Fig. 3.12a for SC2 design).

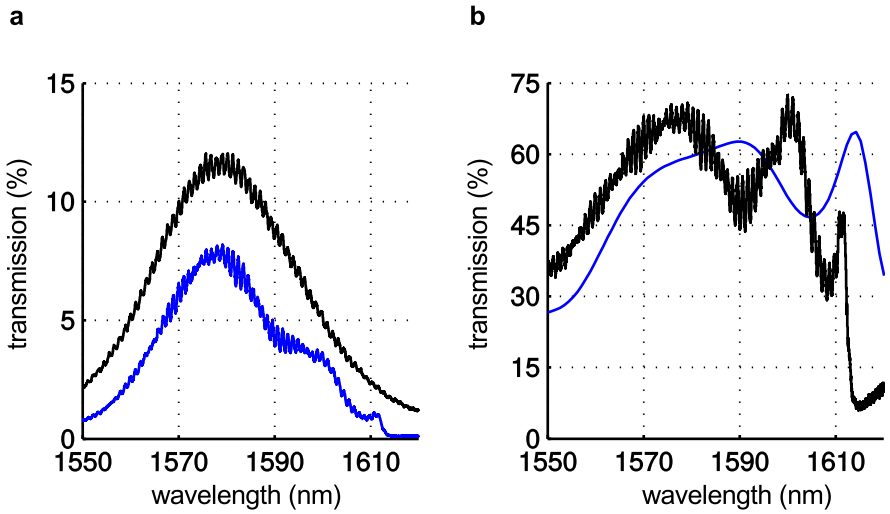

Figure 3.11: (a) Experimental transmission efficiencies for devices EBEB485R1C1n1 (black) and EB485R1C1n5 (blue) measured at 19° incident angle. EB485R1C1n1 is a device with no photonic crystal region, which allowed the efficiency of the grating couplers to be measured and EB485R1C1n5 includes the PCS waveguide in addition. By dividing the blue curve by the black one (Fabry Perot oscillations of the black spectrum are filtered out during division), it is possible for us to find the transmission of this PCS waveguide. The result is the black curve in (b). (b) Simulation (blue) versus experimental (black) transmission from input channel waveguide through PCS waveguide to output channel waveguide. The photonic crystal hole radius is 150 nm and the slot width is 90 nm.

Finally, the full SC2 devices with cavities are tested. The transmission of device EB485R1C1n6 is shown in Fig. 3.12a. As can be seen, the resonance of the cavity (the small peak on the low energy side of the spectrum) is very close to the band edge of the PCS waveguide and the peak resonance transmission value of this

device is 6%. This is significantly lower than simulation result (blue curve) and the resonance is shifted by ~ 15 nm compared to the simulation. The experimental spectra have some Fabry-Perot oscillations with periodicity of ~ 1 nm, which perfectly matches the distance between PCS cavity and output grating coupler. These oscillations do not appear in the simulation result as the simulated structure only includes channel waveguides and the PCS cavity.

Despite the fact that the experimental resonance transmission efficiency of this SC2 device is higher than all SC1 devices in Table 3.3, the expected enhancement (Fig. 2.16c) was not achieved. The reason lies in the amount of side-shift for the holes at the cavity center. The three rings of holes in the SC2 cavity design are shifted by a third of the shifts in the SC1 cavity design. Smaller shifts result in resonance wavelengths that are very close to the edge of the photonic crystal bandgap. This makes the device performance especially sensitive to the fabrication imperfections in the EB485 chip, as is shown in Fig. 3.12b. This figure shows some devices for which the cavity transmission peak is adversely influenced by the imperfections in the fabrication process. This issue affected most of the fabricated devices, which highlights the fabrication challenges for this type of cavity with such small hole shifts. Due to this limitation, it is recommended to fabricate future devices with the same cavities but larger hole shifts while maintaining the butt-coupled geometry to preserve the higher transmission efficiency of the grating couplers and PCS waveguides. More importantly, the PCS waveguide has a major advantage as discussed in Chapter 2; its coupling to cavity Mode 1 is better due to the similarity in their mode profiles.

3.5 Conclusion

In conclusion, the fabrication and characterization of silicon-based photonic integrated circuits consisting of PCS cavities, waveguides and grating couplers, operating at telecommunication wavelengths in a fluidic medium, have been reported. The structures, whose designs are described in the previous Chapter, offer a robust means to enhance electric field intensity and hence light-matter interactions at a precise location inside a fluidic medium, while minimizing fabrication complexity and maximizing ease-of-use. Both 3D FDTD simulations and the experimental

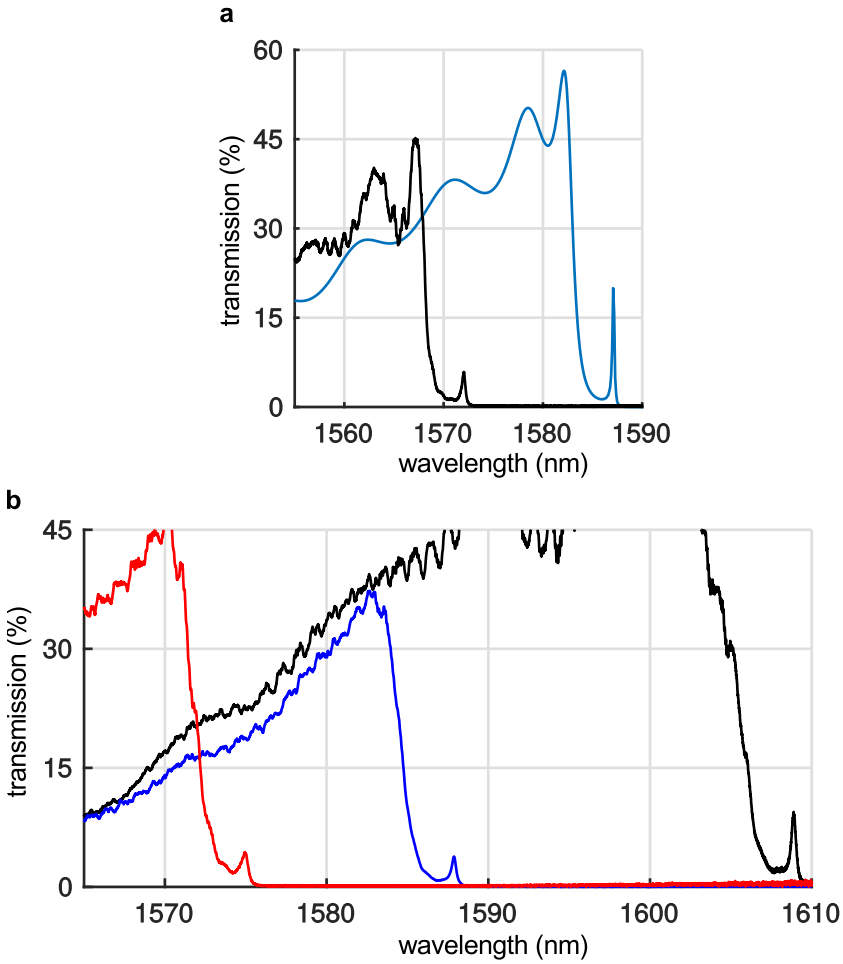

Figure 3.12: (a) Resonant transmission spectra from input to output ridge waveguides through the slot-cavity for device EB485R1C1n6. The simulation curve is blue and the experimental data are plotted in black. The photonic crystal holes are 150 nm with slot width of 90 nm. The Q value of the fabricated device is 4400 as compared to 7400 from simulation. The peak resonant transmission efficiency for the fabricated device is 6% as apposed to the simulated value of 17%. (b) Experimental transmission spectra of three SC2 devices: EB485R1C1n3 (black), EB485R2C1n7 (blue), and EB485R1C1n7 (red).

transmission measurements demonstrate that such circuits, which are fabricated in a single lithography/single etch process without having to undercut the cavity, exhibit Q factors > 7500 and resonant transmissions as high as $T \sim 6\%$, when operated in hexane. Using a butt-coupled configuration improved the design notably by increasing the transmission efficiency of all major parts of a full device. However due to the fabrication imperfections, the cavity Q and peak transmission was not as high as simulation predicted. Their performance could be improved by i) using the original (12 nm, 8 nm, 4 nm) hole shifts for the SC1 cavity and preserving the butt-coupling geometry to have both high-Q and high transmission efficiencies and ii) by using a different cladding layer thickness to increase the grating coupling efficiency.

Chapter 4

Optical Trapping And Sensing Using Photonic Crystal Slot Cavities

4.1 Introduction

In this chapter, we focus on the capabilities of SC1 PCS cavities as high-sensitivity nanotweezers, which not only can trap tiny sub-50 nm Au nanospheres with very low laser power but also enable us to deduce the size of the trapped nanosphere with nanometer sensitivity without using fluorescent particles and/or ancillary imaging apparatus [95, 101, 106].

In the first part of this chapter, the high sensitivity of the PCS cavity resonant frequency is demonstrated by measuring the peak transmission frequency in two different solvents (namely, hexane and acetone) with different refractive indices. In the second part, these devices are immersed in a solution of Au nanospheres and it is found that when ≥ 0.1 mW of resonant CW laser power is launched into the input waveguides, the temporal behaviour of transmitted light through the cavities oscillates in a random fashion when individual nanoparticles are drawn into the cavity region by the large gradient forces associated with the built-up optical power in the cavity. By modelling the time-series data with numerical simulations of

how a small dielectic particle shifts the resonant frequency of the cavity mode depending on where in the cavity it is located, it is shown that the size of the particle can be determined with roughly single nanometre sensitivity.

4.2 Refractive Index Sensing

The fundamental ingredients for achieving large, 3D local field enhancements of CW light from 1D waveguides - critical coupling of the 1D waveguide with the 3D microcavity, small 3D mode volume, and relatively high-Q value, including the waveguide coupling - also imply that the cavity mode resonant frequency can shift by a significant fraction of its linewidth when the dielectric environment inside the cavity is perturbed. By measuring the resonant frequency, one can determine the background refractive index in the cavity. PCS cavities are specifically suited for this kind of sensing application as their electric field mode profiles are mainly concentrated outside of the silicon slab which allows the particles to maximally interact with the strongest intensity region of the cavity mode.

This Section describes how the resonant frequency of Mode 1 of SC1 cavities depends on the solvent refractive index. Figure 4.1 shows the Mode 1 spectra for two devices measured in hexane ($n = 1.365$) and acetone ($n = 1.346$). In both devices, the cavity resonance wavelength red shifts by ~ 7 nm in the large index environment, consistent with simulations. The largest shift in nm per unit variation in refractive index (sensitivity) observed in chip EB312 is 370 nm RIU^{-1} (RIU refers to Refractive Index Unit), for device EB312R22(2,2). This is less than that reported for some samples in Ref. [114] because their structures are undercut, and because they have larger slot widths. Using EB312R22(2,2) cavity Q value, sensitivity, and our signal to noise ratio (SNR) of 33 dB with 0.8 mW excitation power launched into the input ridge waveguide, the detection limit (DL) [125] of these structures is estimated to be 2.3×10^{-5} RIU. This is comparable to other photonic crystal sensors [114, 124, 126, 127] based on undercut cavities. Despite the fact that the Q values of our devices, reported in Table 3.3 are lower than Refs. [128, 129], these devices have larger sensitivity as a result of shifting the field maximum from inside the silicon slab into the fluid. The fact that our samples require no undercutting means that they are remarkably robust: we have cleaned and reused the same chip

over 20 times, over a period of 2 years.

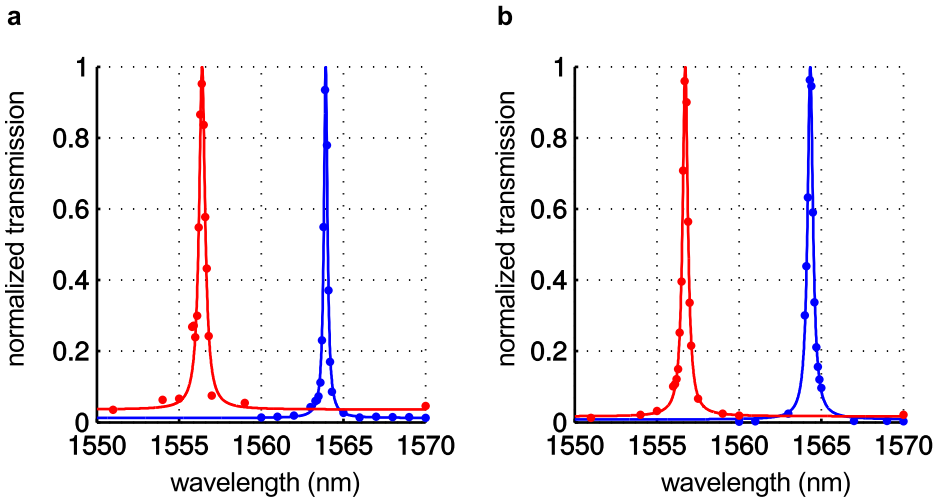

Figure 4.1: Normalized resonant transmission spectra, fitted with a Fano lineshape, for (a) device EB312R22(1,1) and (b) EB312R22(1,2) in hexane (blue) and acetone (red). In figure (a) $Q_{hexane} = 5450$, $Q_{acetone} = 5700$ and for figure (b) $Q_{hexane} = 3980$, $Q_{acetone} = 4100$.

4.3 Optical Trapping Of Au Nanospheres

4.3.1 Experiment Setup

The experiment setup for optical trapping is the same as transmission measurement setup depicted in Fig. 3.6. The only difference is that the laser wavelength is kept fixed around cavity resonance (instead of sweeping in the case of measuring transmission spectra) and the output of the power meter is recorded by the computer to create transmission time-series. The data used in Fig. 4.3 of this chapter was sampled at 1 kHz, while all of the remaining data shown or used for analysis was sampled at 250 kHz.

The optical trapping reported here employs SC1 devices in which photonic crystal (PC) slot microcavities are integrated with single mode channel waveguides and grating couplers in a 220 nm thick silicon layer supported on a SiO_2 cladding layer (SOI). These devices are located on chip EB355. This chip has exactly the

same design as chip EB312 which is fully described in Chapter 3 and the specific device used to collect the data shown here is EB355R1C1(2,2) with the following nominal feature sizes; the diameter of the PC holes is 300 nm, the slot width is 90 nm, the grating coupler holes are 460 nm in diameter, and the coupling holes have a diameter of 220 nm.

Instead of hexane, the devices are immersed in an Isopropyl alcohol (IPA) solution containing polyvinylpyrrolidone (PVP)-encapsulated Au particles (with PVP layer thickness of $\sim 2-4$ nm) of mean Au diameter ~ 50 nm (14% standard deviation), and a mean hydrodynamic diameter of ~ 80 nm, at a concentration of 1.1×10^{11} mL^{-1} (as reported in the data-sheet from nanoparticle manufacturer [130]). IPA is chosen for dispersing Au nanoparticles (NanoComposix Inc.) because of its low absorption at ~ 1.6 μm (most cavity resonances are at wavelengths from 1.53 μm to 1.63 μm when immersed in IPA) and the good stability of PVP-coated Au particles in it.

4.3.2 Trapping Experiment

A schematic of a full SC1 device and its Mode 1 profile is shown in Fig. 4.2, which clearly illustrates that the confined electromagnetic energy is concentrated almost exclusively in a small volume within the slot (solution filled) region of the microcavity [113, 115]. This concentration of the electric field in the solvent, rather than the silicon, distinguishes these cavities from some other planar-waveguide-based three dimensional (3D) microcavities recently used to trap $\sim$ micrometer diameter polystyrene beads [101, 106].

When the CW optical power in the input channel waveguide is ~ 0.75 mW the resonant transmission through the cavity fluctuates as shown in Fig. 4.3a. During the first ~ 230 s, the laser is turned on and off six times, and after each turn-on, there is a period when the transmission is relatively stable at $\sim 90\%$, after which it abruptly starts to fluctuate with large amplitude. The fluctuations are due to perturbations of the cavity resonance frequency when a PVP-coated Au particle is trapped in the vicinity of the mode antinodes (backaction). Since the transmission returns to its nominal, empty-cavity value after turning off and on the laser in these six instances, they are referred to as Temporary Trapping Events (TTES). The sev-

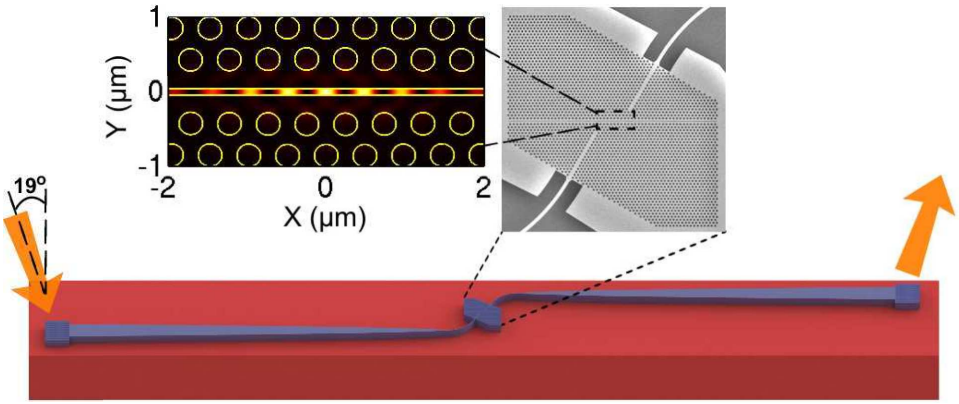

Figure 4.2: The full SSC1 photonic circuit [1] used for trapping is illustrated schematically at the bottom (lateral dimensions to scale). It includes an input and an output grating coupler at each end that symmetrically connects to the photonic crystal microcavity region at the center, through single mode channel waveguides, as shown in the scanning electron microscope (SEM) image at the top, right. The calculated electric field intensity profile of the cavity mode excited in these experiments is also shown at the top, left.

enth off/on cycle that occurs near ~ 250 s is different, because the transmission prior to turning off the laser is relatively constant, and it does not return to the empty-cavity value after turning on the laser. This is due to a Permanent Attachment Event (PAE) occurring at ~ 230 s. Figure 4.3b shows the transmission spectra measured just before and just after the trapping sequence shown in Fig. 4.3a. The almost rigid redshift, and relatively small change in linewidth after a particle has become permanently attached to the microcavity, quantifies the backaction effect on the transmission. The amount of the shift is proportional to the real part of the Au particle's polarizability, and the electric field intensity of the mode at the location of the particle. For a fixed incident power and initial detuning, Δ_0, from the peak empty-cavity transmission, the range over which the transmission fluctuates during any given TTE depends on the particle's polarizability, as it explores the cavity under the influence of Brownian forces.

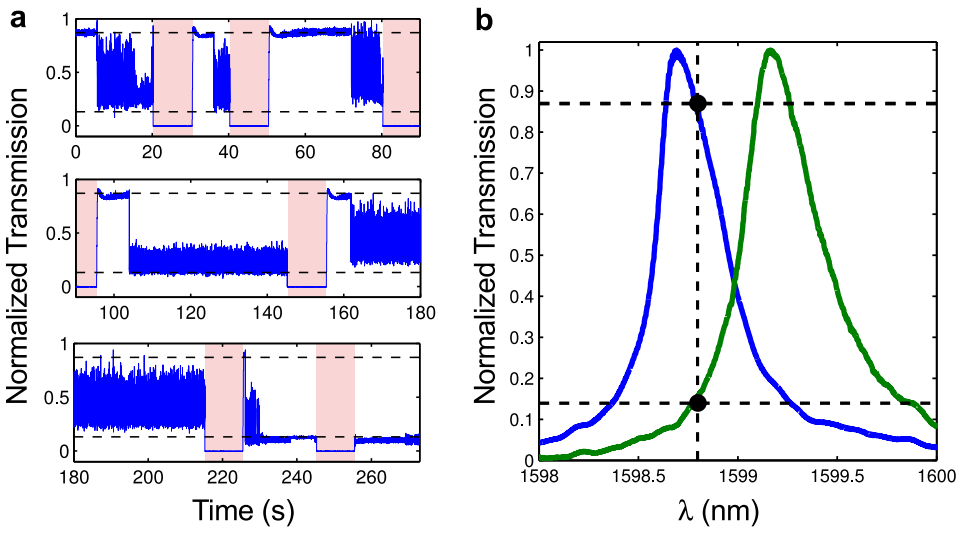

Figure 4.3: (a) Normalized transmission time series from a device with an initial empty-cavity Q factor of ~ 4500 when the laser is tuned close to the peak transmission in the empty-cavity state (black vertical dashed line in (b)), and the guided power in the input channel waveguide is ~ 0.75 mW. The shaded regions indicate when the laser is turned off to release the transiently trapped particles. (b) The transmission spectrum before any trapping events (blue) and after permanently attaching an Au particle (green), both obtained at a power of ~ 0.75 mW. The black circles and horizontal dashed lines show the nominal transmission values at the trapping laser wavelength corresponding to the empty cavity and the cavity with a permanently attached Au particle, as also indicated by the dashed lines in (a).

4.3.3 Time-series Analysis

For the purpose of quantifying the dynamics of the particles during TTEs, it is convenient to work at lower laser powers for which no PAEs occur. Figure 4.4 shows several examples of TTEs obtained with 0.3 mW of power in the input waveguide, for two different initial detunings of the trapping laser. Qualitatively similar transmission dynamics were observed for many similar devices, for injected optical powers ranging from 0.2 mW to 0.4 mW. For a fixed power and initial detuning, a diverse set of TTEs are always observed: in time series data, distinct TTEs are most obviously identified by the minimum value of the fluctuating transmission,

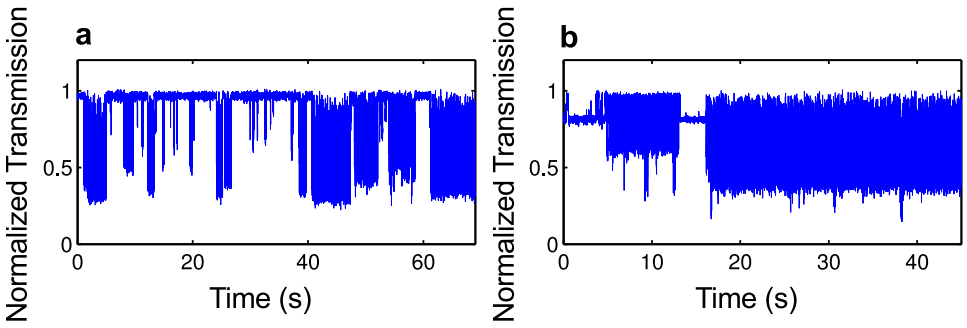

Figure 4.4: (a) The transmission of the cavity when the laser is tuned to $\sim$ 97% of the empty-cavity peak transmission on the red side. (b) The transmission of the same device under the same conditions but with the laser tuned to $\sim$ 82% of the empty-cavity peak transmission (on the red side).

but also sometimes by its maximum value when the mode resonance is not swept through the laser frequency as the particle moves about in the cavity. These distinct TTEs likely correspond to situations when a single particle is temporarily trapped in the vicinity of the cavity, but eventually escapes and is replaced, or is knocked out by a different particle.

Histograms of the fluctuating transmission provide a more detailed description of the dynamics associated with distinct TTE, and can actually be used to define them: for a "*distinct TTE*", histograms generated using any sub-interval are essentially identical to the histogram generated using the entire interval. Figures 4.5b and 4.5c show two experimental histograms (in red) corresponding to the distinct TTEs identified in Fig. 4.5a.

To simulate the histograms of the transmission data, the presence of an Au particle at a position $\vec{r}_p$ in the vicinity of the mode of interest is assumed to rigidly and adiabatically red shift the empty-cavity spectrum by an amount $\delta\lambda_c(\vec{r}_p)$ (although not exact, Fig. 4.3b shows that this is a reasonable approximation). Assuming the particle size is small compared to the length over which the mode intensity varies (typically $< \frac{\lambda}{20}$ [92]), and that its impact on the mode shape can be treated pertur-

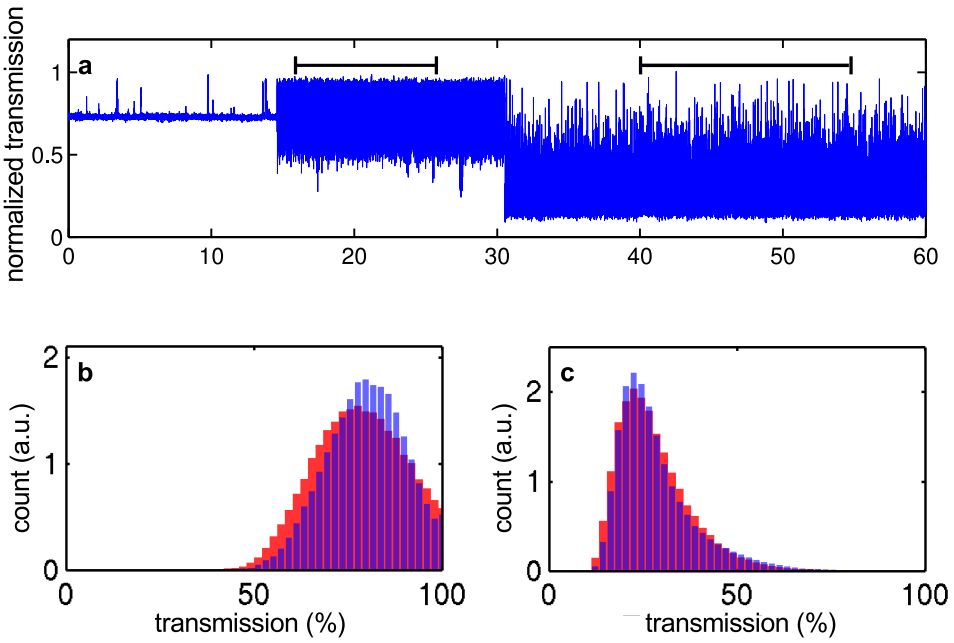

Figure 4.5: (a) A transmission time series obtained at an input power in the waveguide of 0.3 mW at a red detuning set at 73% of the empty-cavity peak transmission. (b) Experimental (red) histogram of the time series data in the range indicated by the left horizontal bar in (a), and the simulated histogram (blue), using a mean particle diameter of 24.8 nm. (c) Experimental (red) histogram of the time series data in the range indicated by the right horizontal bar in (a), and the simulated histogram (blue), using a mean particle diameter of 30.0 nm. The y-axes of both histograms are re-normalized and therefore their units are arbitrary. The total count number for (b) is 2.5×10^6 and for (c) is 3.75×10^6.

batively, $\delta\lambda_c(\vec{r}_p)$ can be approximated as [131]

$$\frac{\delta\lambda_c(\vec{r}_p)}{\lambda_c} = \frac{\alpha'_{Au}\left|E(\vec{r}_p)\right|^2}{2\int \varepsilon(\vec{r})\left|E(\vec{r})\right|^2 d^3\vec{r}}. \tag{4.1}$$

The integral in the denominator is taken over the mode excited in the cavity region (which is well defined for these high-Q modes). The $E(\vec{r}_p)$ in the numerator is the electric field at the location of the particle, and the shift is independent of excitation power due to the normalization. α' is the real part of the particle polarizability in

a background medium with dielectric constant ε_m and for a spherical particle with volume V_p,

$$\alpha = 3V_p\varepsilon_0\varepsilon_m\frac{\varepsilon_p-\varepsilon_m}{\varepsilon_p+2\varepsilon_m}, \tag{4.2}$$

where ε_p is the dielectric constant of the particle.

The cavity resonance shift can also be numerically calculated more precisely using an FDTD electrodynamic solver. As shown in the next sub-Section, comparison of these full FDTD simulations with Equation 4.1 suggest that the factor of 2 in the denominator of Equation 4.1 should be replaced with 1.5, but otherwise Equation 4.1 provides the correct behaviour for different $\vec{r}_p$ and α_{Au}.

To test Equation 4.1, a full FDTD simulation of the cavity is performed as follows. The simulation region, which includes a slot-cavity, an Au particle and an electric dipole source for excitation, is enclosed with perfectly-matched boundary layers. The mesh sizes are non-uniform to make the simulations run faster and more efficiently: a ~ 5.5 nm mesh is used around the spherical Au particle while a ~ 22 nm mesh is used elsewhere. The simulation time is set to 20 ps. Figure 4.6 compares this full FDTD-calculated (black data) shift of the cavity resonance ($\delta\lambda\,(\vec{r}_p)$) for a range of Au particle sizes (Fig. 4.6a) and positions (Fig. 4.6b) in the cavity, with that obtained using Equation 4.1 with the empty-cavity mode profile (blue line). While the agreement is reasonable, it can be significantly improved by scaling the expression in Equation 4.1 by a factor of $2/1.5$ (red curve). While the linewidth of the resonance also changes slightly due to the particle's presence, the effect is much smaller than the shift, and it is neglected in the current analysis (see also the experimental data in Fig. 4.3).

The next part of the modelling involves self-consistently determining the effective optical potential experienced by a particle at a position $\vec{r}_p$, including the backaction. The empty-cavity transmission spectra are not typically Lorentzian, or symmetric, so the experimentally measured transmission spectrum at the trapping power, in the absence of trapped particles, is numerically fit using 8 Gaussians, as shown in Fig. 4.8c. This defines the normalized transmission function, $T(\Delta)$, where Δ is the detuning of the laser wavelength from the cavity resonance. In the presence of a particle at position $\vec{r}_p$, Δ is the initial detuning of the laser wavelength with respect to the empty cavity resonance (Δ_0) minus $\delta\lambda\,(\vec{r}_p)$, as calculated using

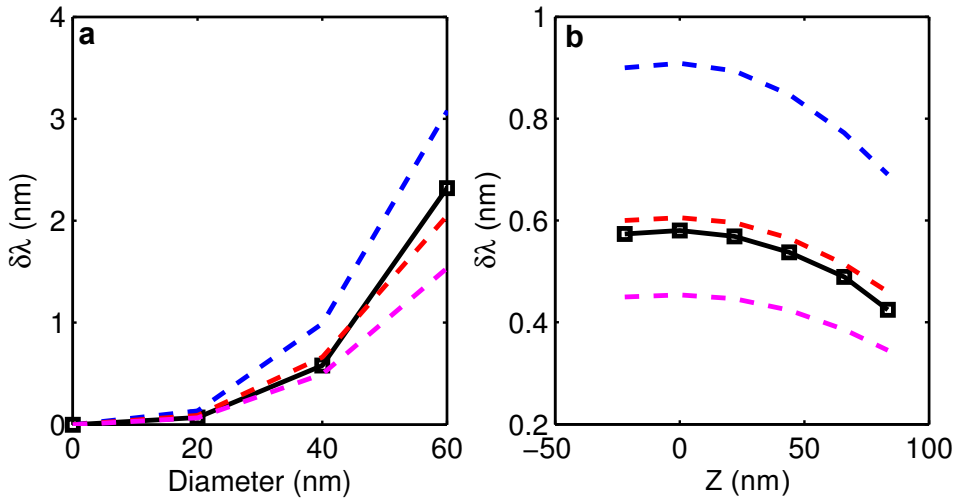

Figure 4.6: (a) A graph of the cavity resonance wavelength shift versus Au particle diameter at the center of the cavity ($\vec{r}_p = (0,0,0)$). (b) A graph of the resonance shift versus the position of a 40 nm diameter Au particle along the z axis at ($x = y = 0$). For both figures, the solid black line shows the full-FDTD simulation results and the dashed color lines are the approximated resonance shifts from Equation 4.1 scaled by three different factors; blue, red and magenta correspond to scaling Equation 4.1 by 2, 2/1.5 and 1, respectively.

Equation 4.1 with the $2/1.5$ scaling factor included.

For a given incident power and initial detuning, the force on a particle at position $\vec{r}_p$, that includes the backaction of the particle on the cavity resonance, is calculated as follows (all these steps are summarized in the flowchart diagram in Fig. 4.7);

1. The $\delta\lambda\,(\vec{r}_p)$ is estimated using the scaled version of Equation 4.1 and the field intensity profile obtained from a full FDTD simulation of the empty-cavity region excited by a guided mode incident in the channel waveguide (example in Fig. 4.8a).

2. $\delta\lambda\,(\vec{r}_p)$ is then subtracted from Δ_0 to find the total detuning, $\Delta(\vec{r}_p)$, of the laser wavelength from the shifted cavity resonance (example in Fig. 4.8b).

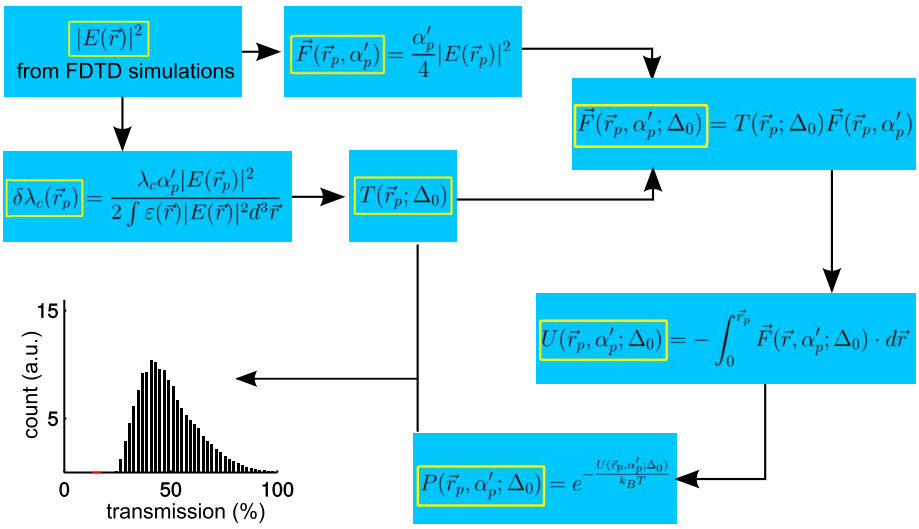

Figure 4.7: This diagrammatic representation illustrates the workflow of modelling a TTE histogram for a given particle size and laser detuning. The initial electric field intensity is calculated using FDTD simulator and the rest of the modelling steps are performed using MATLAB programming. The yellow boxes show the output of each simulation step.

3. The relative transmission at each $\vec{r}_p$ is calculated by mapping $\Delta(\vec{r}_p)$ to the normalized transmission spectrum of the cavity shown in Fig. 4.8c. The resulting function is $T(\vec{r}_p;\Delta_0)$ (example in Fig. 4.8d).

4. The empty-cavity optical gradient force is calculated using the first term of Equation 1.15 from Chapter 1 with empty cavity electric field intensity found from FDTD simulations. For the simulations reported here, it was assumed that $\varepsilon_m=(1.37)^2$ and $\varepsilon_p=-97.4+11.2i$ corresponding to the medium (IPA) and Au dielectric constants, respectively. There is also, in general, a "*radiation force*" associated with directionally-differential absorption of radiation by the particle, but this is negligible in resonantly excited cavities where the fields are essentially standing waves.

5. The empty-cavity force field is multiplied by $T(\vec{r}_p;\Delta_0)$ to obtain the final force field that now takes into account the backaction of the particle.

6. After finding the trapping force field, the trapping potential ($U(\vec{r}_p)$) of a

particle located at $\vec{r}_p$ is determined (example in Fig. 4.8e) by

$$U(\vec{r}_p) = -\int_0^{\vec{r}_p} \vec{F}(\vec{r}) \cdot d\vec{r}. \tag{4.3}$$

The reference point of the integral is selected to be the center of the slot ($\vec{r} = (0,0,0)$), but the resulting histograms are insensitive to the starting point or path of integration.

7. Given the full trapping potential profile, the probability distribution for the time spent by the particle at a given position (example in Fig. 4.8f) is estimated [132] using

$$p(\vec{r}_p) = e^{-\frac{U(\vec{r}_p)}{k_B T}}. \tag{4.4}$$

8. Equation (4.4) along with $T(\vec{r}_p;\Delta_0)$ are used to calculate the histogram of the device transmission by adding the probability of the points that share the same transmission value.

9. As discussed in the following paragraph, in order to explain the experimentally measured transmission histograms, it is also necessary to average several such simulated histograms over a narrow Gaussian distribution of polarizabilities.

Figures 4.9b and 4.9c compare the measured and simulated histograms for the several-second-long TTE identified in Fig. 4.9a. The calculated histogram in Fig. 4.9b is generated using a single particle polarizability corresponding to an Au diameter of 33.8 nm, which is the value one might simply estimate based on the minimum transmission value achieved during the relevant TTE, using Equation 4.1. The much better agreement between simulated and experimental histograms shown in Fig. 4.9c, is obtained by averaging over a range of polarizabilities with a 3% standard deviation about a mean value of 32.6 nm. The significantly improved agreement obtained by averaging over particle polarizability is a general result observed in all TTE simulations. There are at least two possible physical phenomena that might be contributing to this requirement to average over a range of polarizatiblities. Transmission electron microscope images of the particles indicate they are not spherical, so Brownian rotation of a trapped particle in the polarized field of the

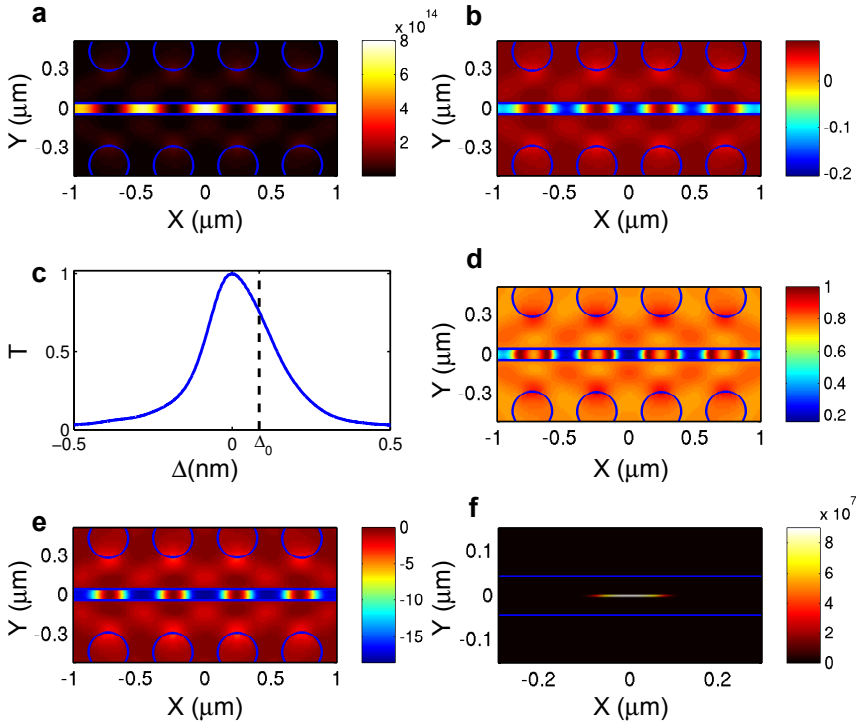

Figure 4.8: (a) The electric field intensity profile in the *x*-*y* plane (i.e. the plane that cuts through the middle of the silicon slab), from FDTD simulations with 0.3 mW of resonant modal power in the input ridge waveguide. The unit of the intensity is $(\frac{V}{m})^2$. (b) The profile of the $\Delta(\vec{r}_p)$ function, which is the detuning (units of nm) of the laser wavelength from the cavity resonance wavelength with a particle of diameter 30 nm located at $\vec{r}_p$, calculated using $\Delta(\vec{r}_p) = \Delta_0 - \delta\lambda(\vec{r}_p)$. (c) The transmission function $T(\vec{r}_p;\Delta_0)$ plotted versus Δ . The laser wavelength is detuned to 73% of the peak transmission wavelength of the empty-cavity, on the red side. (d) The transmission function $T(\vec{r}_p;\Delta_0)$ profile in *x*-*y* plane. Note that at the center of the cavity $T = 0.2$, showing when the particle of diameter 30 nm is located at the center of the cavity, the transmission of the device is expected to drop to 0.2 of its maximum because of the shift in the cavity resonance (backaction effect). (e) The trapping potential energy including the backaction in units of k_BT (Boltzmann factor) calculated using Equation 4.3. (f) The probability distribution calculated using Equation 4.4. This probability distribution is used in calculating the histogram shown in Fig. 4.5c.

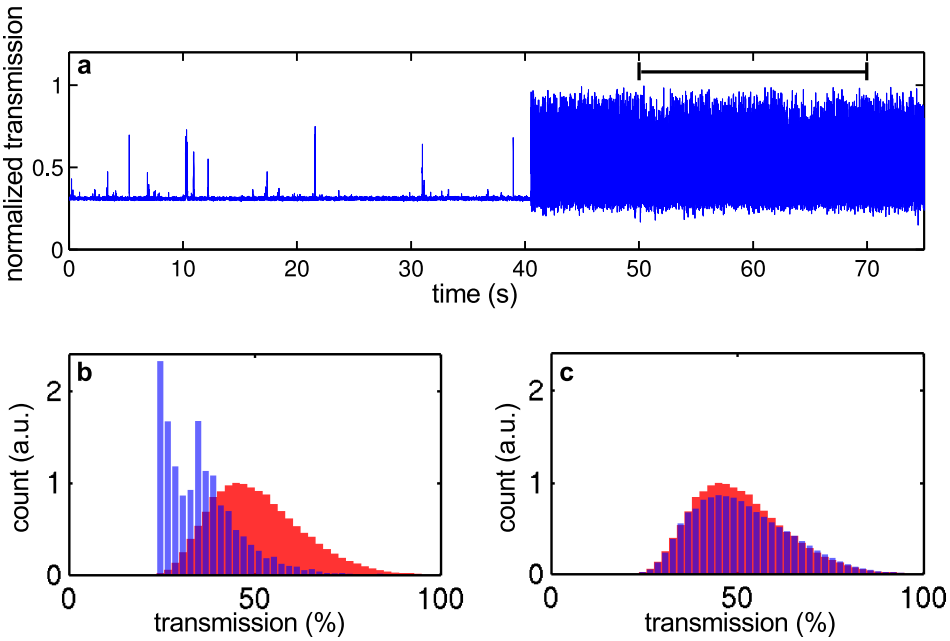

Figure 4.9: (a) Normalized transmission time series obtained at an input power in the waveguide of 0.3 mW at a red detuning set at 31% of the empty-cavity peak transmission. (b) Experimental (red) histogram of the time series data in the range indicated by the horizontal bar in (a), and the simulated histogram (blue), obtained using a fixed particle diameter of 33.8 nm. (c) The same experimental histogram as in (b) (red) is plotted with a histogram (blue) obtained by averaging over a normal (Gaussian) distribution of particle diameters centered at 32.6 nm with standard deviation of 3%. The total count number for the experimental histogram is 5×10^6.

cavity could be one contributing factor. The PVP coating on the outside of the particles (interpreted as being responsible for the difference between the Au diameter and the hydrodynamic diameter) is expected to be fluctuating in its configuration, which could also be contributing. The relatively small difference in dielectric properties of PVP and the solvent make us suspect that the non-spherical shape of the Au is most important. This issue is investigated in Chapter 5 by performing further trapping experiments on more anisotropic nanoparticles and generalizing our histogram analysis.

The two distinct TTE histograms simulated in Figs. 4.5b and 4.5c for fixed laser excitation conditions, agree well with the experimental histograms. The mean diameters of the particles in the two cases are 24.8 nm (with 3% standard deviation) and 30.0 nm (with 4% standard deviation). These and many similar simulations for a wide variety of histograms observed at different (red and blue) detunings, indicate that most distinct TTEs correspond to particles of different sizes that explore the full mode distribution in the slot. The best fitted histograms are selected based on minimization of the χ^2 as a goodness of the fit parameter, which is defined as

$$\chi^2 = \sum_{i=histogram\ bin} \frac{(ec_i - sc_i)^2}{sc_i}. \tag{4.5}$$

The sum in this equation runs over each bin of the histograms. ec_i denotes the count number of bin i of the experimental histogram and sc_i is the corresponding count number for the simulated histogram. Figure4.10 shows an example of the χ^2 function calculated for a TTE. The best fit histogram, calculated by minimization of χ^2, is shown in Fig. 4.11c and Fig. 4.12c. Along with the best fitted histogram in these two figures, the calculated histograms for slightly different nanosphere diameters and anisotropies are also plotted to demonstrate the extreme sensitivity of this histogram model. It is obvious that for even a small change of < 0.5 nm in the mean diameter of the trapped nanosphere, the calculated histogram changes significantly and the fit quality decreases. This is also true for the anisotropy of the particle. The model is quite sensitive to $< 1\%$ anisotropy variations. These estimates of the sensitivity of the fits to the fitting parameters are not yet based on rigorous χ^2 analysis, but rather on comparing plots as shown in Fig. 4.11 and Fig. 4.12 "*by eye*". More work along the lines reported in Ref. [133] is required to produced statistically significant uncertainties for these fit parameters.

4.3.4 Cavity Mode 2 and Size Sensing In Heterogeneous Solution

From many comparisons of model and experimental histograms similar to those shown in Figs. 4.5 and 4.9, the maximum diameters of modeled Au particles captured in the trap is ~ 34 nm, considerably smaller than the mean diameter in solution. To verify that the relatively small size (compared to the mean particle diam-

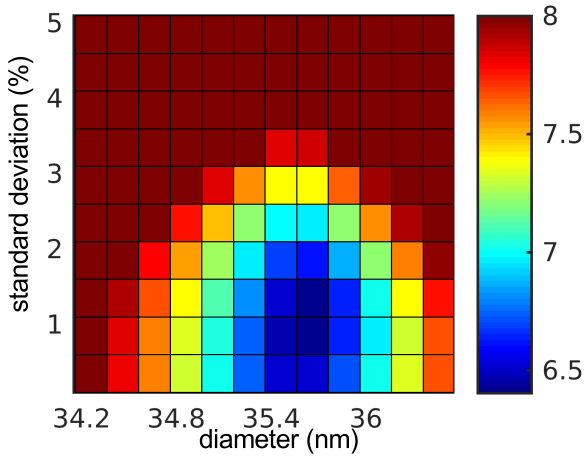

Figure 4.10: The graph of $log_{10}(\chi^2)$ as a function of particle diameter and Gaussian averaging standard deviation. The best fit histogram is determined by finding the minimum of the χ^2.

eter of 50 nm, or the most probable diameter of 56 nm) of the particles trapped in the slot cavity mode is indicative of some physical hindrance, rather than an artifact of the model, the same analysis is applied to trapping data obtained using the second mode supported by this type of microcavity [115]. Figure 4.13 shows the simulated mode profile and resonant transmission spectra associated with a device that is identical to the one discussed in the manuscript except that its slot width is 100 nm rather than 90 nm. The highest intensity regions for this mode, where trapping occurs, are not in the slot, but at the edges of the 300 nm diameter holes adjacent to the slot. There should be no hindrance for any of the particles in solution accessing these holes, and indeed, several simulations of various TTEs from this mode (examples of which are shown in Fig. 4.13c-h) yield particle sizes that are completely consistent with the average size of the nanoparticles reported by the manufacturer [130].

4.4 Conclusion

In this chapter, two applications of SC1 devices, as high-sensitivity tools, are demonstrated experimentally. Both of these applications exploit the strong light-

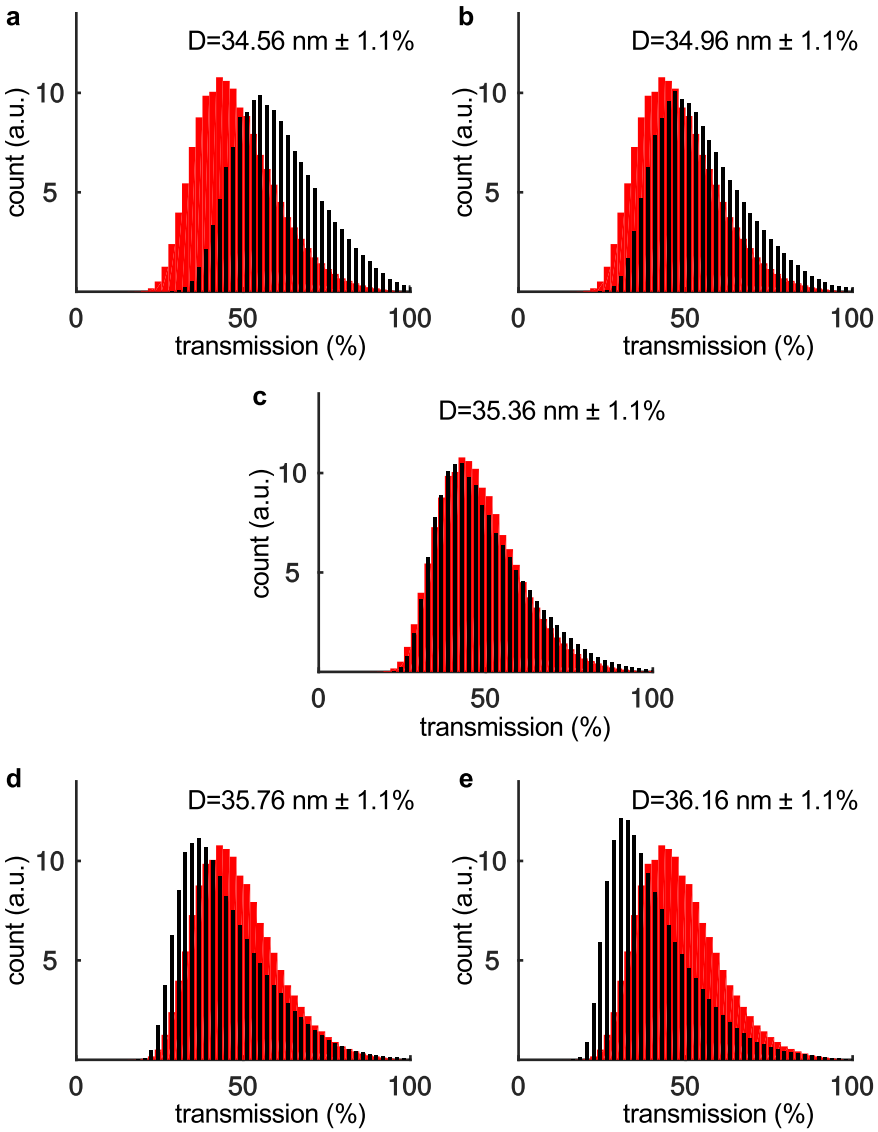

Figure 4.11: [(a)-(e)] An experimental histogram (red) versus simulated histograms (black) of particles with various average diameter (D) and a fixed standard deviation of 1.1% for Gaussian averaging. All histograms are obtained for an input power in the waveguide of 0.3 mW and a red detuning set at 31% of the empty-cavity peak transmission. The total count number for the experimental histogram is 15×10^6.

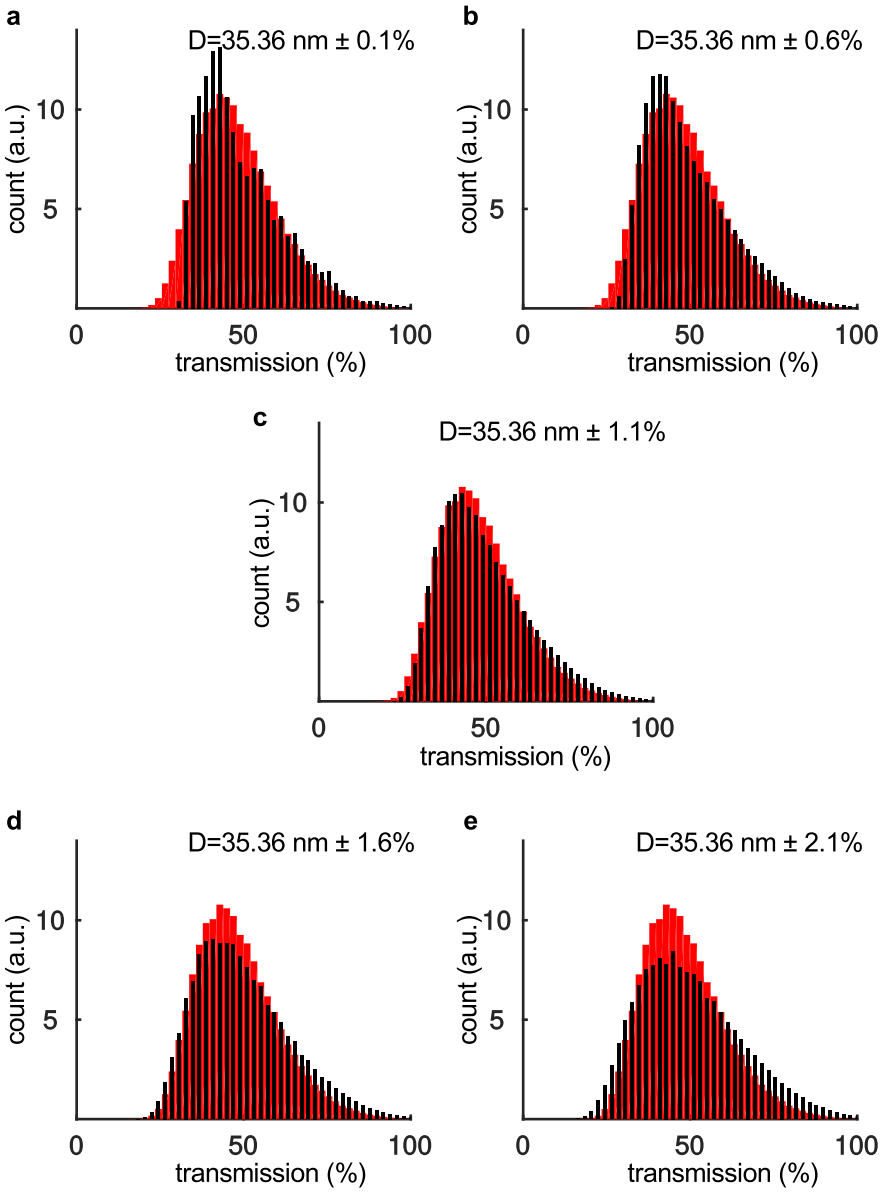

Figure 4.12: [(a)-(e)] Experimental histogram (red) versus simulated histograms (black) of Au nanospheres with a fixed average diameter (D) of 35.36 nm and various standard deviation for Gaussian averaging. All histograms are obtained for an input power in the waveguide of 0.3 mW and a red detuning set at 31% of the empty-cavity peak transmission.

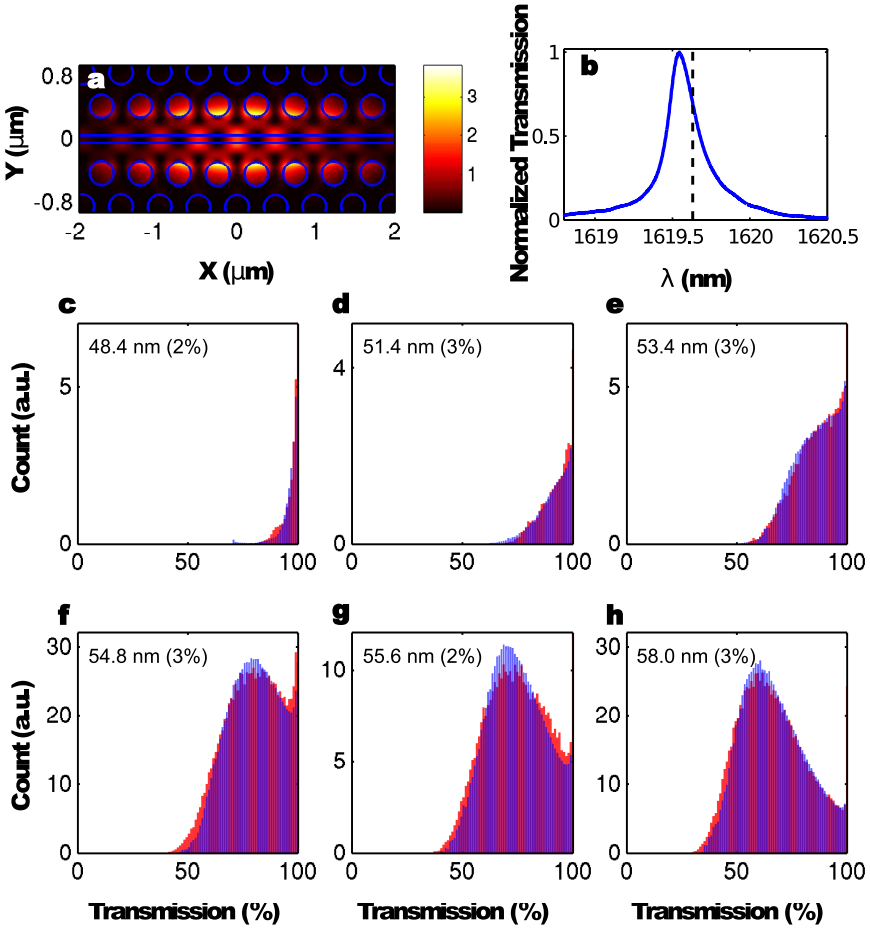

Figure 4.13: (a) The electric field intensity profile (in arbitrary units) of the second cavity mode in the *x*-*y* plane, calculated from a FDTD simulation. (b) The experimentally measured, normalized, empty-cavity transmission at the second cavity mode resonance of a device almost identical to the one discussed in the manuscript (see text for explanation of the difference); the guided power is 0.28 mW. The dashed line indicates the trapping laser wavelength used to obtain the 6 sets of experimental (red) and modelled (blue) histograms shown in (c)-(h) associated with 6 distinct TTEs. The estimated diameter (percent variation) of trapped Au particles extracted from these modelled histograms are shown in each plot.

matter interactions in these PCS cavities due to the fact that the majority of electric field intensity in this structure is located outside of the silicon slab. As nanotweezers, these devices require very low optical power for trapping sub-50 nm particles as demonstrated in Table 4.1. As a refractive index sensor, these un-optimized structures have a detection limit for refractive index change of $\sim 2 \times 10^{-5}$ RIU which is comparable with best photonic crystal cavity based sensors [114, 124, 126, 127]. Their performance can be further enhanced by undercutting the cavity (removing SiO_2 undercladding will increase the refractive index contrast and reduce out-of-plane loss by enhanced TIR) and using a butt-coupled geometry for exciting the cavity.

A self-consistent, quantitative model of optical backaction and optical gradient forces in a PC-based silicon slot waveguide microcavity quantitatively describes the dynamics of cavity transmission as influenced by Au nanoparticles as small as $\sim$ 24 nm diameter, transiently trapped using sub-mW CW excitation powers. The backaction footprint of trapped particles on cavity transmission dynamics can distinguish mean particle diameters at the single nanometer level, and polarizability anisotropies at the 1% level without requiring fluorescent tagging or ancillary imaging apparatus. This low-power, silicon-wafer-based device geometry, together with the sensitivity of the transmission analysis technique, present exciting opportunities for further advancing the science and application of nanoscale photonics [93].

Table 4.1: Summary of trapping performance of various tweezers.

Tweezer Type	Operating Wavelength (nm)	Particle Material	Particle Diameter (nm)	Trapping Power (mW)	Reference
Laser Tweezers	514.5	polystyrene	100	15	[68]
dipole antennas	808	gold	10	2	[12]
nanopillar	974	polystyrene	110	10	[11]
double nanoholes	975	silica	12	10	[13]
microring	1550	polystyrene	500	9	[15]
microdisk	1550	polystyrene	1000	7.6	[17]
PC nanobeam	1548	polystyrene	48	NA	[18]
PC nanobeam	1064	polymer	22	11	[19]
PC nanobeam	1585	polystyrene	1000	0.3	[101]
PC hollow cavity	1500	polystyrene	250	0.36	[106]
our PCS cavity	1570	gold	25	0.3	[3]

Chapter 5

Optical Trapping of Nanorods

5.1 Introduction

The results presented in the previous chapter strongly suggest that the time series histograms of TTEs are very sensitive to not only the overall size of the trapped particle but also any anisotropy in its shape. This chapter describes a generalization of the histogram model described in Chapter 4 to include particle anisotropy. Using this model, we validate the conjecture that the particle anisotropy was the reason that averaging over sphere size was required to get good agreement with experimental data in Chapter 4, and then demonstrate how this generalized model can also be used to extract the size and shape of highly anisotropic Au nanorods trapped in the same cavity as in Chapter 4. The corresponding experimental data represent the first, to our knowledge, report of using nanotweezers to trap sub-50 nm size nanorods. While the importance of including rotational potential energy of anisotropic particles in polarized laser beams has been recognized [76, 134–138], the closest work to that reported here involved the use of 1D photonic crystal nanotweezers to trap several micron long carbon nanotubes [139].

In Section 5.2, we first generalize our histogram-fitting model to explicitly account for nanoparticle anisotropy by considering the rotational motion introduced by optical torques on ellipsoidally-shaped trapped nanoparticles. The main difference in the new model is the use of a tensor-form polarizability and the inclusion of optical torques in addition to the Center Of Mass (C.O.M) optical forces, when eval-

uating the optical potential for a particle located at any point, and any orientation in the cavity. Then in Section 5.3, it is demonstrated that with this more generalized model, we obtain high-quality histogram fits for Au nanospheres without averaging over sphere sizes as was done in Chapter 4 (i.e. the new model predicts extreme sensitivity of the transmission histograms to slight particle asymmetries). In Section 5.4 we present new experimental optical trapping data obtained with solutions containing sub-50 nm long, $<$ 15 nm diameter Au nanorods and show that the histograms can be accurately fit with the generalized model to extract the size and aspect ratio of such particles. The qualitatively different nature of the anisotropic histograms is intuitively explained, and the future applications of this technique to identify the size and shape of nanoscale particles in solution is discussed in Section 5.5.

5.2 Self Consistent Model Including Anisotropic Particles

To simulate the trapping of anisotropic particles, both the rotational and c.o.m motion of a particle in the presence of an electric field must be accounted for. As is explained in Chapter 1, for small nanoparticles, the optical trapping force on the center of mass of the particle can be described using the dipole approximation:

$$\mathbf{F} = \frac{1}{2} Re[\sum_{i=x,y,z} p_i{}^* \nabla E_i]. \tag{5.1}$$

where p_i and E_i are the components of the complex valued dipole moment and external electric field respectively and * denotes the complex conjugate. Under the same approximation, the optical torque generated in the cavity electric field on a point dipole is:

$$\boldsymbol{\tau} = \frac{1}{2} Re[\mathbf{p}^* \times \mathbf{E}], \tag{5.2}$$

The induced dipole moment depends on the polarizability α of the trapped particles:

$$\mathbf{p} = \alpha \cdot \mathbf{E}, \tag{5.3}$$

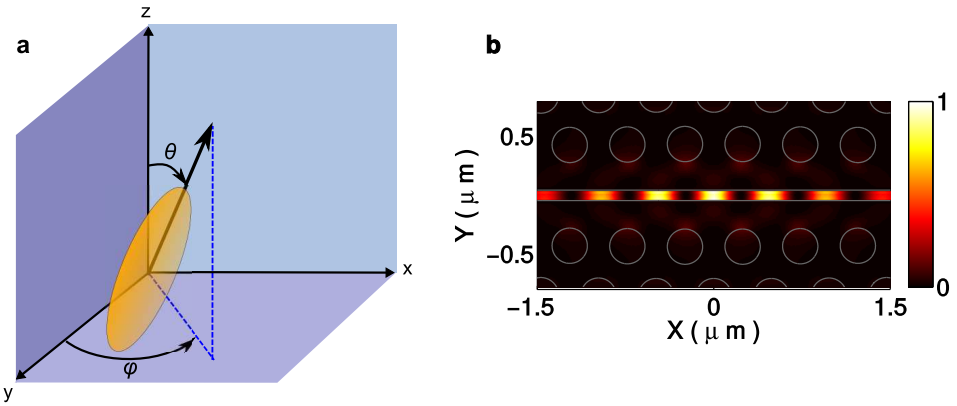

Figure 5.1: (a) A prolate spheroid in the cavity coordinate system. (b) The calculated normalized electric field intensity profile of Mode 1 of a SC1 cavity, which is used for trapping nanorods, with slot width of 90 nm and hole radius of 150 nm. The cavity mode is polarized along the y-axis at its center.

For anisotropic particles, the polarizability necessarily becomes a tensor. We assume that the particles can be approximated as prolate spheres in order to take advantage of analytical expressions for the polarizability tensor of prolate spheroids. Specifically, in the particle coordinate system ($x'y'z'$) with the particle's long axis parallel to z'-axis, the polarizability takes the form:

$$\alpha' = \begin{bmatrix} \alpha_S & 0 & 0 \\ 0 & \alpha_S & 0 \\ 0 & 0 & \alpha_L \end{bmatrix} \tag{5.4}$$

where $\alpha_{L,S}$ are the polarizabilities along the long and short axes of a prolate spheroid of radius R and length L with:

$$\alpha_{L,S} = \varepsilon_m \varepsilon_0 V_{Au} \frac{\varepsilon_{Au} - \varepsilon_m}{\varepsilon_m + x_{L,S}(\varepsilon_{Au} - \varepsilon_m)} \tag{5.5}$$

where ε_m and ε_{Au} are the dielectric constant of the background medium and the Au nanoparticles respectively, V_{Au} is the nanoparticle volume and x_L and x_S are the well-known ellipsoidal depolarization factors given in [140].

When the anisotropic particle is oriented in the cavity such that its long axis is at an angle θ to the z-axis and azimuthal angle of φ to the x-axis (see Fig. 5.1 for cavity coordinate system xyz), the polarizability tensor $\alpha(\theta,\varphi)$, in the cavity frame of reference, is calculated using two rotational transformations:

$$\alpha(\theta,\varphi) = R\alpha' R^{-1}, \tag{5.6}$$

where

$$R = \begin{bmatrix} cos(\varphi) & -sin(\varphi) & 0 \\ sin(\varphi) & cos(\varphi) & 0 \\ 0 & 0 & 1 \end{bmatrix} \begin{bmatrix} cos(\theta) & 0 & sin(\theta) \\ 0 & 1 & 0 \\ -sin(\theta) & 0 & cos(\theta) \end{bmatrix}. \tag{5.7}$$

Since the slot cavity mode has a small mode volume and high-Q factor, the presence of a single nanoparticle translating and rotating in the vicinity of the mode volume can significantly shift the resonance wavelength of the cavity and therefore change the amount of electromagnetic energy coupled to the cavity mode at the laser wavelength. In the previous chapter, we included this backaction effect in our model by renormalizing the electric field intensity of the cavity ($\mathbf{E}(\mathbf{r})$) by a transmission function ($T(\delta\lambda)$), where $\delta\lambda$ was the shift of the cavity resonance due to the backaction (see Chapter 4 for details). The shift $\delta\lambda$ can be approximated in terms of the nanoparticle's dipole moment (which now has a tensor form for polarizability) and cavity electric field as:

$$\delta\lambda(\mathbf{r},\theta,\varphi) = \frac{\lambda_0 Re[\{\alpha(\theta,\varphi)\mathbf{E}(\mathbf{r})\}^* \cdot \mathbf{E}(\mathbf{r})]}{m\int \varepsilon_0 \varepsilon(\mathbf{r}) |\mathbf{E}(\mathbf{r})|^2 d\mathbf{r}}, \tag{5.8}$$

λ_0 is the empty cavity resonance wavelength, $\varepsilon(\mathbf{r})$ denotes the dielectric function of the device and m is a prefactor that enhances the dipole approximation accuracy. Following the same steps as in Chapter 4, for modelling experimental histograms, the prefactor m in Equation 5.8 is found by fitting the result of simulations of cavity resonance wavelength, when different size and orientation nanoparticles are placed at cavity center. Figure 5.2 shows the best fitting results that happen for $m = 1.5$.

The total trapping potential energy $U(\mathbf{r},\theta,\varphi)$ of a spheroid inside the cavity is found by calculating the work done by both the optical force and torque on the spheroid located at the origin and aligned to z-axis (i.e. $\mathbf{r} = 0,\ \theta = 0,\ \varphi = 0$)

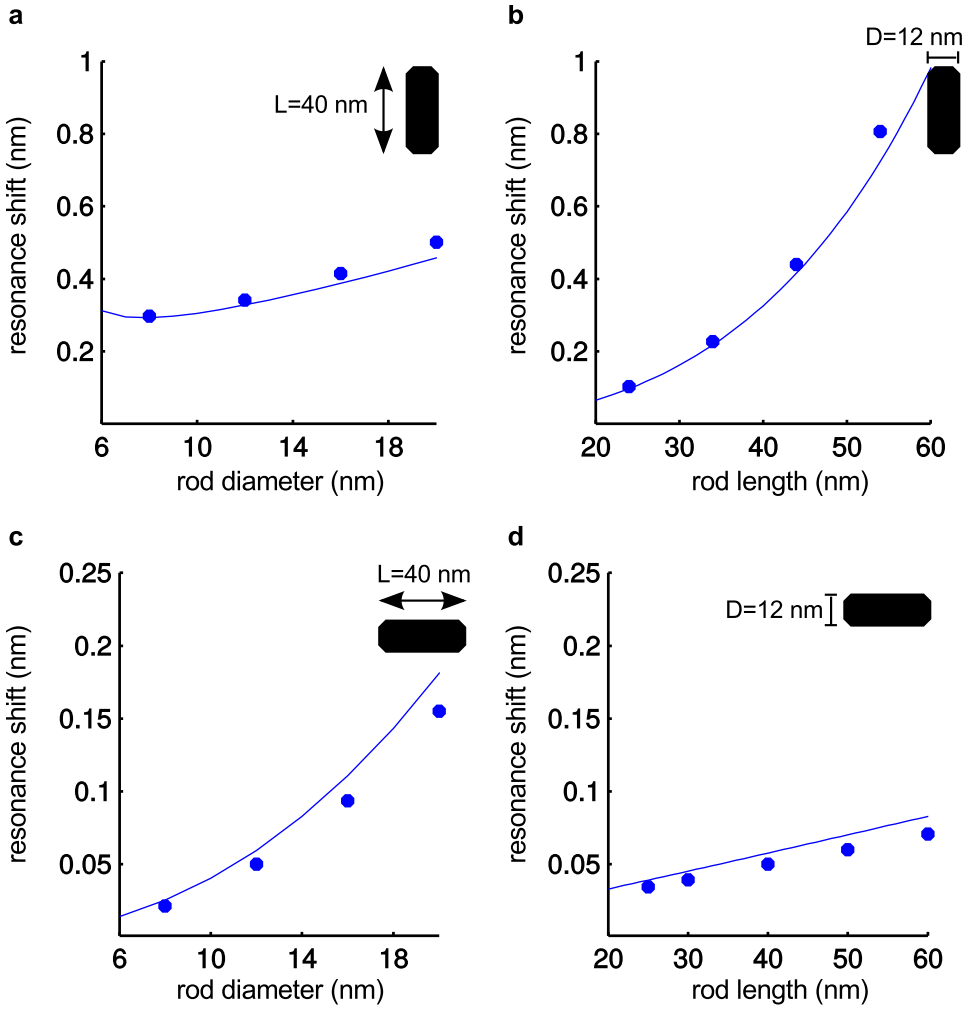

Figure 5.2: The amount of cavity resonance shift when different size and orientation nanorods are placed at the center of a SC1 cavity with slot width of 90 nm and hole radius of 150 nm. For (a)-(b) the nanorod is perpendicular to the slot ($\theta = \frac{\pi}{2}$, $\varphi = \frac{\pi}{2}$) and (a) is the resonance shift as a function of nanorod diameter (length of 40 nm) and (b) shows the dependance on nanorod length (diameter of 12 nm). (c) and (d) show the same relationships as (a) and (b) respectively, except that the rod is oriented along the slot (i.e. $\theta = \frac{\pi}{2}$, $\varphi = 0$) for these two plots. The filled circles are the result from simulations and the curves are calculated from Equation 5.8 with $m = 1.5$ and assumption of perfect cylindrical shape for the nanorods.

to a final center of mass location and orientation. From the trap potential energy map, a simulated transmission histogram for a certain laser power and detuning and particle geometry can be calculated following the same procedure as shown in Fig. 4.8 of Chapter 4.

As demonstrated in Fig. 5.3, the overall shapes of calculated histograms show distinct qualitative differences based on the particle's degree of anisotropy. High-aspect ratio spheroids will have a large impact on $\delta\lambda$ as they rotate in and out of alignment with the cavity mode polarization, which results in larger variation of device transmission (as shown in Fig. 5.4). Therefore, when comparing histograms of particles of similar diameters, but different anisotropy, the transmission distribution is expected to be larger in total range for nanoparticles that are relatively more anisotropic (as demonstrated in Fig. 5.3). As the aspect ratio increases from a perfect spherical shape to more anisotropic spheroids, the histograms shift to the left but maintain their long tail to higher transmissions. The shift to the left is due to the large $\delta\lambda$ when the long axis of the higher aspect ratio rods is aligned with the electric field at the cavity mode antinode.

5.3 Explaining the Need to Average Histograms for Imperfect Nanospheres

Another notable impact of including rotational motion in the model is that it naturally yields smooth simulated histograms without requiring averaging. As discussed in Chapter 4, a model accounting only for translational degrees of freedom (which was appropriate for isotropic particles) can only match the smoothness of experimental histograms of nominally, but not precisely spherical particles, by averaging simulated histograms over a narrow distribution of nanosphere diameters. This is illustrated in Fig. 5.5a-b where the relatively poor fit of an experimental transmission histogram of a gold nanosphere TTE using the isotropic particle model without averaging is shown. It was posited that the averaging requirement was because the Au nanospheres are not actually perfectly spherical but possess shape irregularities and surface corrugation that give the particle's polarizability a slight anisotropy. These irregular spheres rotate in the cavity mode, which effectively samples different size spheres, averaging out the transmission histograms.

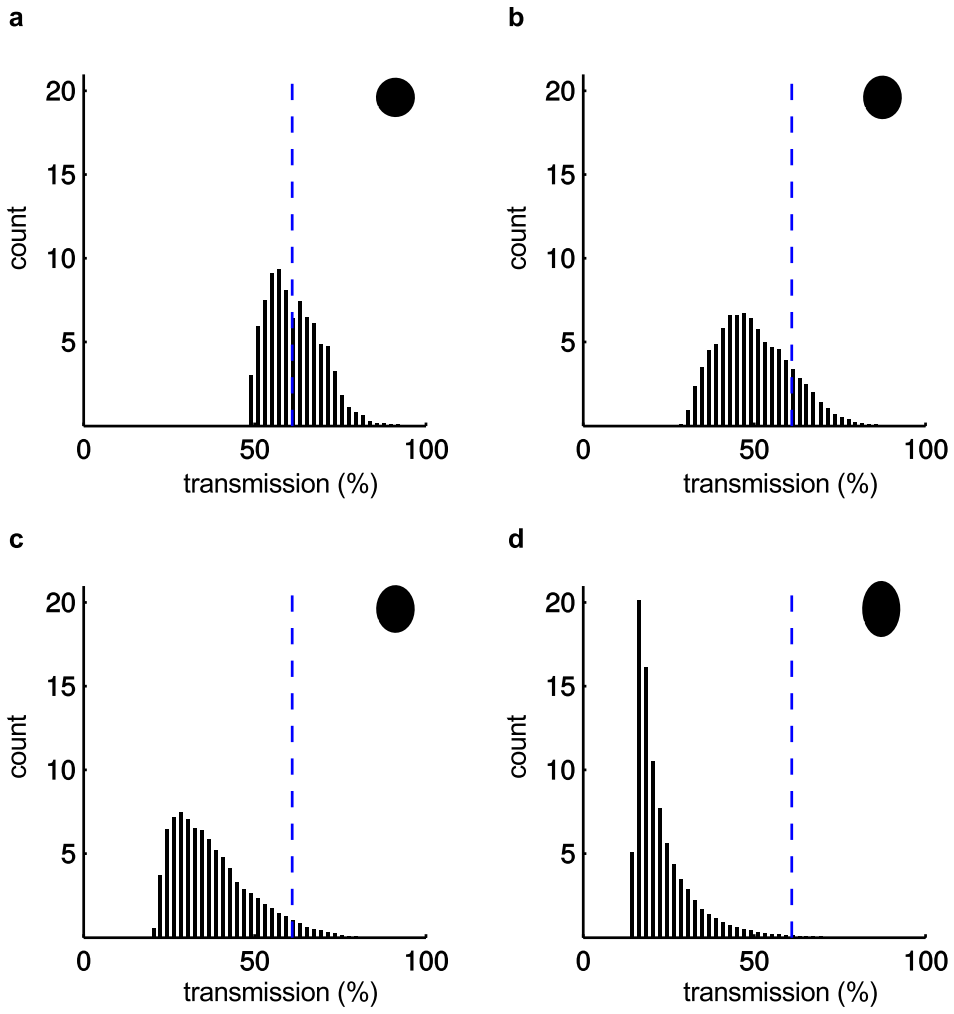

Figure 5.3: [(a)-(d)] Histogram of 4 different spheroids with same short diameter of 32 nm and different aspect ratios calculated with the anisotropic trap model including torques. The aspect ratios are 1 (a), 1.1 (b), 1.2 (c), and 1.4 (d), respectively. The empty cavity transmission (i.e. without any particle in the cavity) is shown with blue dashed line in all graphs.

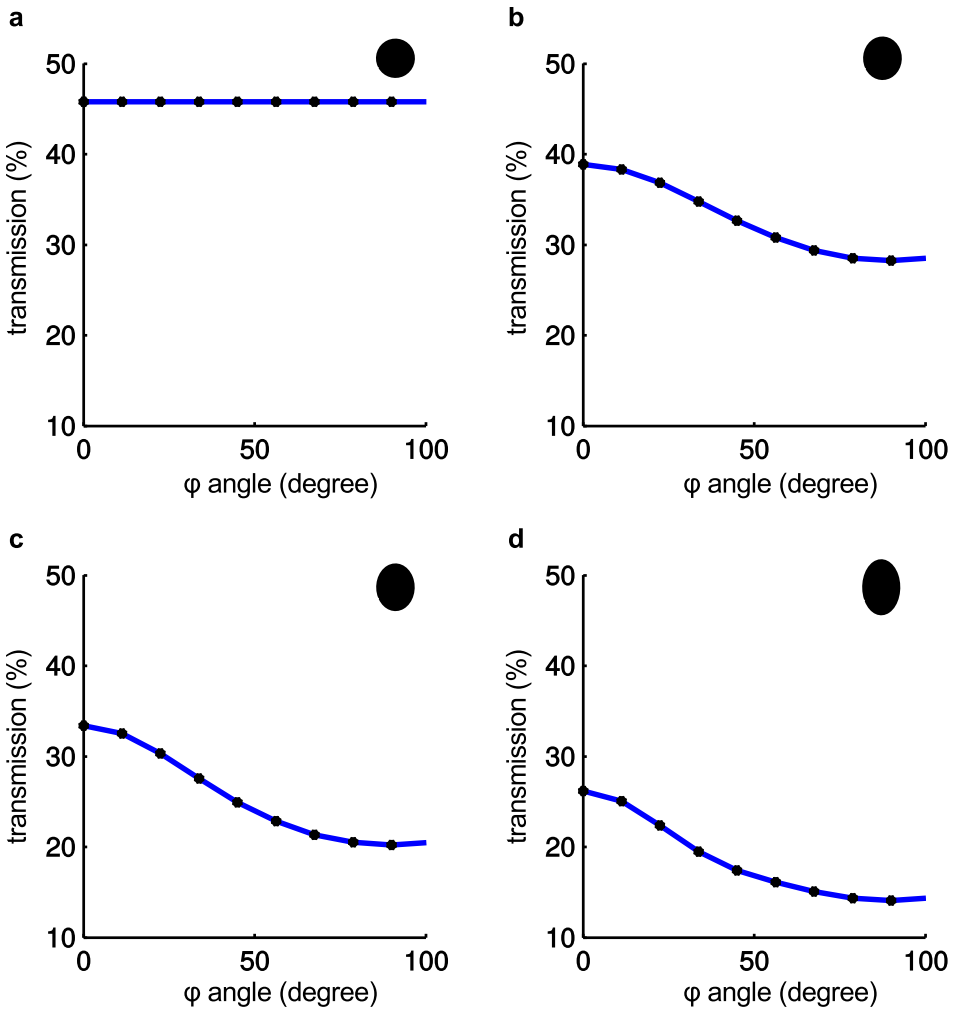

Figure 5.4: [(a)-(d)] The dependence of the device transmission on the φ orientation of 4 different spheroids with same shorter diameter of 32 nm and different aspect ratios. The aspect ratios are 1 (a), 1.1 (b), 1.2 (c), and 1.4 (d), respectively and their θ angle for all 4 particles is 90 degrees. All particles are located at the intensity antinode of the cavity mode.

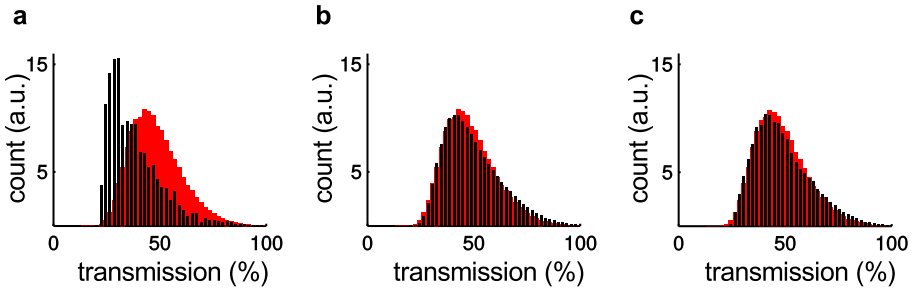

Figure 5.5: (a) Experimental histogram (red) during trapping of Au nanosphere along with fitted histogram (black) assuming a perfectly spherical shape of diameter 36.4 nm. (b) Same experimental (red) histogram as in (a), with the simulated histogram (black), using a normal distribution of sizes of mean diameter 35.36 nm and 1.1% standard deviation. (c) The same experimental histogram (red) is fitted (black) assuming a spheroid shape for the trapped nanoparticle. The extracted size of the spheroid is 34.4 nm $\times$37.1 nm.

Figure 5.5c shows how this explanation is supported by including rotation in the trap potential model. The same nanosphere TTE transmission data is fit with the new model, which naturally yields the slight anisotropy of the imperfect sphere and the consequently smooth histograms (the nanoparticle size extracted from both histograms in Fig. 5.5b-c agree very well, which confirms both models predict similar amount of anisotropy for the trapped particle.). This highlights the importance of including optical torques in the trap potential calculations even for nominally spherical Au particles due to the impressive sensitivity of the trapping devices to even the slightest particle non-uniformity.

5.4 Trapping Gold Nanorods

The trapping experiments are accomplished in Mode 1 of a SC1 PCS cavity (device EB355R1C1(2,2)) with a 90 nm wide slot and hole diameter of 300 nm that is immersed in a methanol solution of polyvinylpyrrolidone (PVP) coated gold nanorods with average size of 44 nm $\times$12 nm [1]. Figure 5.6 shows the SEM images

[1] These nanorods are synthesized by Jonathan Massey-Allard based on a procedure described in Ref. [141]

of the cavity and nanorods. The slot-cavity structure is designed to support a cavity mode with a relatively high-Q (~ 5200) (when immersed in methanol) and with antinodes located in the slot where they are easily accessible to the nanoparticles. These characteristics of the PCS cavity result in trapping sub-50 nm nanorods at coupled laser power as small as only 0.2 mW (this is the estimated power in the input channel waveguide).

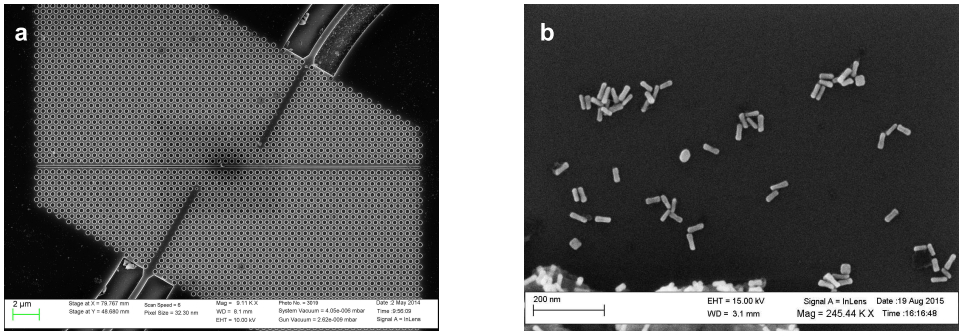

Figure 5.6: (a) Scanning electron microscope (SEM) image of a 90nm wide slot cavity [1] used for trapping. (b) SEM image of the Au nanorods used in the trapping experiments. The average size of the rods, extracted from SEM images, is 44 nm $\times$12 nm with 15% standard deviation.

Similar to nanosphere trapping in previous chapter, TTEs of nanorods are clearly evident as sudden high-amplitude fluctuations in the transmission signal through the photonic circuit (shown in insets of Fig. 5.7), which are due to backaction effect.

The distribution of transmission signal amplitudes during a TTE are arranged in histograms that provide a rich description of the dynamics associated with that trapping event. Histograms corresponding to various nanorod trapping events are shown (in red) in Fig. 5.7a-f. Best fits to the experimentally obtained histograms using the above described model are shown in black in Fig. 5.7a-f. The extracted sizes agree well with the average size of the nanorods as measured from SEM images (Fig. 5.6b). Among these histograms, Fig. 5.7c has significantly narrower distribution, which by looking at the extracted size, it is noticed that this particle is very low-aspect ratio, which explains its histogram shape and indeed SEM images of these nanorods confirm that there are some low-aspect ratio nanorods in the

solution (some of them are observable in Fig. 5.6b).

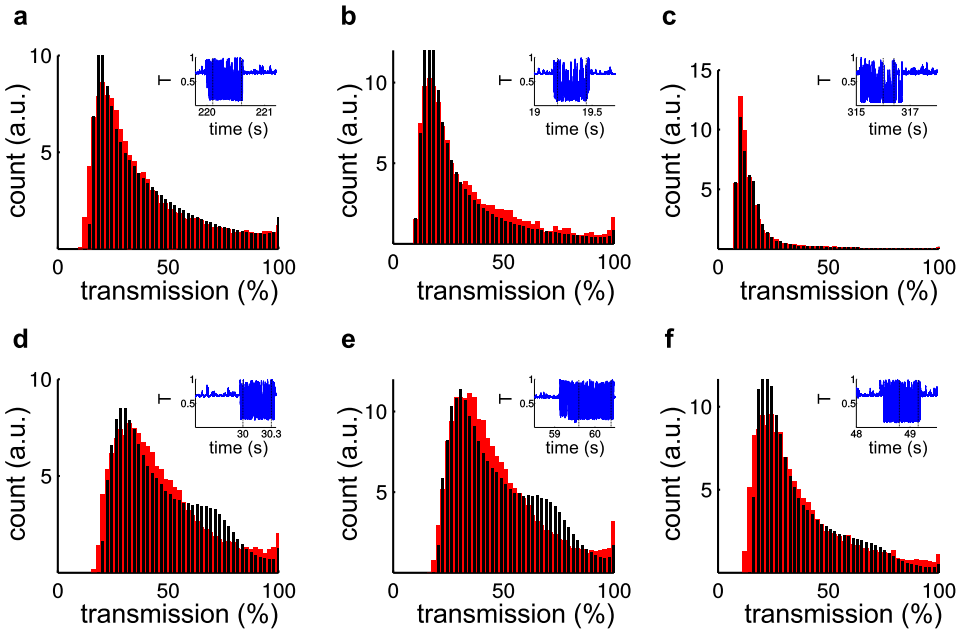

Figure 5.7: [(a)-(f)] 6 different nanorod experimental (red) histograms are illustrated along with the calculated (black) histograms fits based on theory accounting for the nanoparticles' anisotropy. The insets show the corresponding normalized transmission time series collected during the trapping experiment and the dashed black lines show the range for which the experimental histogram is collected. (a)-(c) are for laser power of 0.2 mW in the waveguide and the estimated nanorod size based on the fits are 14 nm $\times$46 nm, 14 nm $\times$50 nm and 38 nm $\times$39 nm respectively. The actual total count number for the experimental histograms in these three plots are 10^5, 6.25×10^4, and 1.25×10^5 respectively. (d)-(f) are at 0.25 mW power and the estimated sizes based on the fits are 13 nm $\times$42.5 nm, 12 nm $\times$43 nm and 12 nm $\times$46 nm. The total count number for the experimental histograms in these three plots are 2×10^5, 8.75×10^4, and 7.5×10^4 respectively.

Another fact about these fitted histograms is that although the fits are acceptable, they are not as good as sphere histogram fits in the previous chapter. The main reason for the lower quality of fitting is the shape of the nanorods that do not have uniform uniform diameters along their lengths. As is shown in Fig. 5.6b,

the ends of the nanorods have a larger diameter compared to their waists. This makes their polarizability tensor different than a perfect cylindrical shape, which results in inaccurate resonance shift estimation based on FDTD simulations of perfect cylinders and fits to the tensor-polarizability function of an ellipsoid. To solve this issue, it is important to find the average shape of the nanorods in the solution and try to use FDTD simulations to estimate the resonance shift of the cavity when this shape nanorod is placed in it and from that find a more accurate value for the prefactor m in Equation 5.8.

5.5 Conclusion

This chapter reports the recent advances in trapping sub-50 nm gold nanorods using an SOI cavity-based nanotweezers at sub-mW injected power. It is demonstrated that the strong sensitivity of the PCS cavity to the presence of a single trapped particle can be utilized to study the size and shape of the trapped particles simply from the device's transmission signal during a trapping event by modeling the linear and rotational motion of a nanorod in the trapping potential of the cavity and including the backaction of the nanorod on the cavity resonance. Using this statistical model to fit the transmission histograms during a trapping event we are able to estimate the dimensions of trapped nanorods in the solution. Distinct signatures in the transmission histograms of different aspect ratio particles suggest that our imaging-free method can be used to differentiate the shapes of the trapped particles in heterogeneous solutions.

Chapter 6

Conclusions and Outlook

6.1 Conclusions

Two slightly different and unique planar photonic circuits made using silicon-on-insulator wafers were designed and characterized. Both were intended to serve as robust chips that could be immersed in a solvent containing small dielectric nanoscale particles that would be attracted to and trapped within sub-micron sized microcavities using the optical gradient forces available when < 1 mW of $\sim 1.5\,\mu$m laser radiation was coupled into the circuits. The microcavities in both cases were based on locally modified slot photonic crystal waveguides, and the differences in the two designs were in how light was coupled to the cavities via a series of grating couplers and waveguides.

A series of samples based on the first design (SC1), that used photonic crystal waveguides to couple at a 60 degree angle to microcavities with cavity-defining hole shifts of 12, 8, and 4 nm in 3 rings of PC holes adjacent to the cavity, exhibited *Q* factors and overall transmission values in reasonable agreement with simulations when deviations of the fabricated patterns from the designs were taken account of. To our knowledge, the highest *Q*s of 7500, are one of the best reported for supported PC cavity structures operating in solvent. By comparing the transmission spectra from one of the best samples using hexane and IPA solvents, a detection limit for sensing refractive index changes in the environment of 2.3×10^{-5} RIU was determined, which is comparable to other optical-chip based sensor structures

reported in the literature.

Despite this design suffering scattering losses in the coupling waveguides and their connections to each other and the microcavity, both Au spheres of diameters down ~ 20 nm, and Au nanorods as small as 13 nm $\times$42 nm were successfully trapped using less than 0.5 mW of CW laser power coupled into the channel waveguides. The experimental results from a series of samples fabricated based on the second design (i.e. SC2), which used in-line butt-coupling between channel and PC slot waveguides, and cavity-defining hole shifts of 6, 4, and 2 nm in 3 rings adjacent to the cavity, were less satisfactory. While transmission results from test structures that did not include the microcavity, but did include the butt-coupled channel/PC waveguides, agreed quite well with the design specifications, only a few cavities exhibited the desired transmission characteristics. The reason is most likely due to the fact that with the small hole-shifts defining the cavity, its resonant frequency is very close to the photonic band-edge of the slot waveguide mode from which it derives, so even small fabrication imperfections can be expected, in retrospect, to "*lose*" the cavity mode. Nevertheless, the one sample that came closest to the design specifications did in fact exhibit a 3 fold improvement in net transmission over the best of the first designed samples (theoretically it should have been 5 fold better), and its Q value was 4400. Preliminary trapping experiments with this one sample based on the second design proved that it was capable of trapping Au spheres with diameters down to 15 nm with < 0.5 mW of power launched in the input channel waveguide.

The most significant and interesting results of the work came from developing a fully self-consistent model for the statistics of the laser transmission during individual transient trapping events. This novel approach to analyzing the transmission histograms of individual trapped particle took into account the backaction of the particle on the cavity resonance spectrum while undergoing Brownian motion (both translation and rotation), leaving the particles size and shape (assuming the functional dependence of a particles polarizability to be that of a ellipsoid) to be fit by comparison to the experimental transmission data, plotted as a histogram. Several experiments with both nominally spherical and high aspect ratio Au (~ 8) nanorods convincingly demonstrated that the histogram shapes are sensitive to the overall size and shape of the trapped particle, with approximately single nanometer

sensitivity.

6.2 Future Work

The advances in this work in building nanotweezers and exploiting them for trapping and sensing tiny particles holds great promises in terms of applications. For instance it is possible to use these high-Q, small mode volume nanotweezers to permanently trap and self-assemble tiny photon emitters like colloidal quantum dots and quantum rods for increasing their spontaneous emission rates and creating on-chip single photon sources for quantum communication circuitry. Similarly because of their enhanced electric field, single molecule cavity-enhanced spectroscopic analysis and low-threshold single quantum dot lasers can be demonstrated in this platform.

Based on these applications, the main goal of future works is to push down the size of the particles that can be trapped in these tweezers (to a few nanometers) and find a controllable way to permanently localize trapped particles in the cavity. Some of the challenges that need to be faced along the way, are discussed below.

1. To increase the trapping forces, the first thing to try is repeating butt-coupling geometry as SC2 design, but with the larger hole-shift cavities, and test the fabricated devices by trapping few-nm Au particles to indicate how much smaller particles they can trap with up to 1 mW of coupled power. Also more work can be done on optimizing structure parameters like under-cladding thickness, slot width, cavity hole location and radii. Undercutting the cavity would also improve the Q factor because of better vertical confinement.

2. Upon confirmation of trapping smaller Au particles, it is possible to use the new devices for trapping other particles like colloidal quantum dots. Switching the particles requires totally different chemistry which in its own is a big challenge. Solvents and stabilization methods for new types of particles are different. For instance, we tried SC1 and SC2 devices for trapping PbSe quantum dots without successful results. One of the main issues is the Oleic acid molecules that are used for functionalization of quantum dots to make them stable in solvents. These Oleic acid can easily cover the surface of the

PC and stops dots from reaching to the cavity center. New functionalization methods in different solvents needs to be developed to solve this issue.

3. It is crucial to develop controllable ways to integrate single nanoparticles into the cavity. In our nanosphere trapping, it was observed that by increasing the laser power it is possible to permanently localize single trapped particles. This power dependence needs to be further investigated in detail. Also it is important to find a way to flush out the rest of nanoparticles in the solution without removing the trapped particle or cover the surface of the cavity with contamination. Developing microfluidic channels or working with syringe pumps to create a controlled flow of solvent might be a solution. Another benefit of microfluidic channels, is that it enables creating a reservoir of nanoparticles and then have a slot waveguide passing through it and delivering nanoparticles to the cavity in a controlled way.

4. As it is mentioned in Chapter 3, after each round of trapping experiments, the chip needs to be cleaned. One of the reasons is having particle trapped away from the cavity at locations like coupling holes, adapters etc. which interferes with the transmission efficiency of devices. Increasing the optical forces for a given input power is crucial to reduce these incidents as increasing the laser power will cause more trapping in unwanted areas. Also developing microfluidic channels will help solving this issue because it can eliminate exposure of nanoparticles to unwanted areas of the chip.

5. To improve the theory of backaction and the accuracy of the self-consistent histogram analysis, the first thing to do is include Q factor changes associated with particle motion/orientation in our model, specially when the trapped particle has a dielectric resonance near the cavity resonance. Under these conditions it is not possible to ignore the impact of the particle field on the cavity mode field and a more general theory is needed to accurately describe particle-cavity optomechanical interactions.

6. The strong size-dependent backaction in this system, allows one to develop size-selective tweezers. By fully investigating the influence of different parameters (e.g. laser detuning, power, location of trapped particles) on the

depth of trapping potential, one can exploit these tweezers to specifically trap a certain size/shape particles in a heterogeneous solution.

Bibliography

[1] S. Hamed Mirsadeghi, Ellen Schelew, and Jeff F. Young. Photonic crystal slot-microcavity circuit implemented in silicon-on-insulator: High q operation in solvent without undercutting. *Applied Physics Letters*, 102(13):131115, April 2013.

[2] S. H. Mirsadeghi, E. Schelew, and J. F. Young. Compact and efficient silicon nanowire to slot waveguide coupler. In *2013 13th International Conference on Numerical Simulation of Optoelectronic Devices (NUSOD)*, pages 31–32, 19-22 Aug. 2013.

[3] S. Hamed Mirsadeghi and Jeff F. Young. Ultrasensitive diagnostic analysis of au nanoparticles optically trapped in silicon photonic circuits at sub-milliwatt powers. *Nano Lett.*, 14(9):5004–5009, September 2014.

[4] Richard J. Bojko, Jing Li, Li He, Tom Baehr-Jones, Michael Hochberg, and Yukinori Aida. Electron beam lithography writing strategies for low loss, high confinement silicon optical waveguides. *Journal of Vacuum Science & Technology B*, 29(6):06F309, October 2011.

[5] Charles A. Foell. *Luminescent properties of Pb-based (PbX) colloidal quantum dots (CQDs) in vacuum, on silicon and integrated with a silicon-on-insulator (SOI) photonic integrated circuit (PIC)*. PhD thesis, The University Of British Columbia, 2016.

[6] Gatien Cosendey, Jean-Franois Carlin, Nils A. K. Kaufmann, Raphal Butt, and Nicolas Grandjean. Strain compensation in alinn/gan multilayers on gan substrates: Application to the realization of defect-free bragg reflectors. *Applied Physics Letters*, 98(18):181111, May 2011.

[7] U. Gruning, V. Lehmann, S. Ottow, and K. Busch. Macroporous silicon with a complete two-dimensional photonic band gap centered at 5 μm. *Applied Physics Letters*, 68(6):747–749, June 1996.

[8] S. Y. Lin, J. G. Fleming, D. L. Hetherington, B. K. Smith, R. Biswas, K. M. Ho, M. M. Sigalas, W. Zubrzycki, S. R. Kurtz, and Jim Bur. A three-dimensional photonic crystal operating at infrared wavelengths. *Nature*, 394(6690):251–253, July 1998.

[9] David G. Grier. A revolution in optical manipulation. *Nat Photon*, 424(6950):810–816, August 2003.

[10] Mathieu L. Juan, Maurizio Righini, and Romain Quidant. Plasmon nano-optical tweezers. *Nat Photon*, 5(6):349–356, June 2011.

[11] Kai Wang, Ethan Schonbrun, Paul Steinvurzel, and Kenneth B. Crozier. Trapping and rotating nanoparticles using a plasmonic nano-tweezer with an integrated heat sink. *Nature Communications*, 2:469, September 2011.

[12] Weihua Zhang, Lina Huang, Christian Santschi, and Olivier J. F. Martin. Trapping and sensing 10 nm metal nanoparticles using plasmonic dipole antennas. *Nano Lett.*, 10(3):1006–1011, March 2010.

[13] Yuanjie Pang and Reuven Gordon. Optical trapping of 12 nm dielectric spheres using double-nanoholes in a gold film. *Nano Lett.*, 11(9):3763–3767, September 2011.

[14] Judith Su, Alexander F. G. Goldberg, and Brian M. Stoltz. Label-free detection of single nanoparticles and biological molecules using microtoroid optical resonators. *Light Sci Appl*, 5:e16001, January 2016.

[15] Shiyun Lin, Ethan Schonbrun, and Kenneth Crozier. Optical manipulation with planar silicon microring resonators. *Nano Lett.*, 10(7):2408–2411, July 2010.

[16] Haotian Wang, Xiang Wu, and Deyuan Shen. Localized optical manipulation in optical ring resonators. *Opt. Express*, 23(21):27650–27660, October 2015.

[17] Hong Cai and Andrew W. Poon. Optical manipulation of microparticles using whispering-gallery modes in a silicon nitride microdisk resonator. *Opt. Lett.*, 36(21):4257–4259, November 2011.

[18] Sudeep Mandal, Xavier Serey, and David Erickson. Nanomanipulation using silicon photonic crystal resonators. *Nano Lett.*, 10(1):99–104, January 2010.

[19] Yih-Fan Chen, Xavier Serey, Rupa Sarkar, Peng Chen, and David Erickson. Controlled photonic manipulation of proteins and other nanomaterials. *Nano Lett.*, 12(3):1633–1637, March 2012.

[20] Nicolas Descharmes, Ulagalandha Perumal Dharanipathy, Zhaolu Diao, Mario Tonin, and Romuald Houdre. Single particle detection, manipulation and analysis with resonant optical trapping in photonic crystals. *Lab Chip*, 13(16):3268–3274, May 2013.

[21] V. R. Almeida, Q. Xu, C. A. Barrios, and M. Lipson. Guiding and confining light in void nanostructure. *Optics letters*, 29(11):1209–1211, June 2004.

[22] Ellen N. Schelew. Characterization of photonic crystal based silicon-on-insulator optical circuits fabricated by a cmos foundry. Master's thesis, The University Of British Columbia, 2011.

[23] Dirk Englund, David Fattal, Edo Waks, Glenn Solomon, Bingyang Zhang, Toshihiro Nakaoka, Yasuhiko Arakawa, Yoshihisa Yamamoto, and Jelena Vuckovic. Controlling the spontaneous emission rate of single quantum dots in a two-dimensional photonic crystal. *Phys. Rev. Lett.*, 95(1):013904, July 2005.

[24] Z. G. Xie, S. Gtzinger, W. Fang, H. Cao, and G. S. Solomon. Influence of a single quantum dot state on the characteristics of a microdisk laser. *Phys. Rev. Lett.*, 98(11):117401, March 2007.

[25] Andrea M. Armani, Rajan P. Kulkarni, Scott E. Fraser, Richard C. Flagan, and Kerry J. Vahala. Label-free, single-molecule detection with optical microcavities. *Science*, 317(5839):783, August 2007.

[26] James E. Baker, Rashmi Sriram, and Benjamin L. Miller. Two-dimensional photonic crystals for sensitive microscale chemical and biochemical sensing. *Lab Chip*, 15(4):971–990, December 2015.

[27] Ahmed A. Al Balushi, Ana Zehtabi-Oskuie, and Reuven Gordon. Observing single protein binding by optical transmission through a double nanohole aperture in a metal film. *Biomedical Optics Express*, 4(9):1504–1511, July 2013.

[28] Ahmed A. Al Balushi and Reuven Gordon. Label-free free-solution single-molecule protein-small molecule interaction observed by double-nanohole plasmonic trapping. *ACS Photonics*, 1(5):389–393, May 2014.

[29] Keir C. Neuman and Steven M. Block. Optical trapping. *The Review of scientific instruments*, 75(9):2787–2809, September 2004.

[30] Charles A. Foell, Ellen Schelew, Haijun Qiao, Keith A. Abel, Stephen Hughes, Frank C. J. M. van Veggel, and Jeff F. Young. Saturation behaviour of colloidal pbse quantum dot exciton emission coupled into silicon photonic circuits. *Opt. Express*, 20(10):10453–10469, May 2012.

[31] E. Knill, R. Laflamme, and G. J. Milburn. A scheme for efficient quantum computation with linear optics. *Nature*, 409(6816):46–52, January 2001.

[32] J. W. Silverstone, R. Santagati, D. Bonneau, M. J. Strain, M. Sorel, J. L. OBrien, and M. G. Thompson. Qubit entanglement between ring-resonator photon-pair sources on a silicon chip. *Nature Communications*, 6:7948, August 2015.

[33] Pieter Kok, W. J. Munro, Kae Nemoto, T. C. Ralph, Jonathan P. Dowling, and G. J. Milburn. Linear optical quantum computing with photonic qubits. *Rev. Mod. Phys.*, 79:135–174, January 2007.

[34] R. Soref and J. Larenzo. All-silicon active and passive guided-wave components for λ = 1.3 and 1.6 μm. *IEEE Journal of Quantum Electronics*, 22(6):873–879, June Jun 1986.

[35] R. Soref and B. Bennett. Electrooptical effects in silicon. *IEEE Journal of Quantum Electronics*, 23(1):123–129, January 1987.

[36] B. Schuppert, J. Schmidtchen, and K. Petermann. Optical channel waveguides in silicon diffused from gesi alloy. *Electronics Letters*, 25(22):1500–1502, September 1989.

[37] R. A. Soref, J. Schmidtchen, and K. Petermann. Large single-mode rib waveguides in gesi-si and si-on-sio$_2$. *IEEE Journal of Quantum Electronics*, 27(8):1971–1974, August 1991.

[38] B. Jalali and S. Fathpour. Silicon photonics. *Journal of Lightwave Technology*, 24(12):4600–4615, January 2006.

[39] E. Schelew, G. Rieger, and J. Young. Characterization of integrated planar photonic crystal circuits fabricated by a cmos foundry. *Journal of Lightwave Technology*, 31(2):239–248, November Jan.15, 2013.

[40] M. G. Banaee, A. G. Pattantyus-Abraham, M. W. McCutcheon, G. W. Rieger, and Jeff F. Young. Efficient coupling of photonic crystal

microcavity modes to a ridge waveguide. *Applied Physics Letters*, 90(19):193106, May 2007.

[41] F. Van Laere, T. Claes, J. Schrauwen, S. Scheerlinck, W. Bogaerts, D. Taillaert, L. O'Faolain, D. Van Thourhout, and R. Baets. Compact focusing grating couplers for silicon-on-insulator integrated circuits. *IEEE Photonics Technology Letters*, 19(23):1919–1921, November 2007.

[42] G. Roelkens, D. Vermeulen, D. Van Thourhout, R. Baets, S. Brision, P. Lyan, P. Gautier, and J.-M. Fdli. High efficiency diffractive grating couplers for interfacing a single mode optical fiber with a nanophotonic silicon-on-insulator waveguide circuit. *Applied Physics Letters*, 92(13):131101, March 2008.

[43] Gnther Roelkens, Dries Van Thourhout, and Roel Baets. High efficiency grating coupler between silicon-on-insulator waveguides and perfectly vertical optical fibers. *Opt. Lett.*, 32(11):1495–1497, 2007.

[44] Regis Orobtchouk, Abdelhalim Layadi, Hamid Gualous, Daniel Pascal, Alain Koster, and Suzanne Laval. High-efficiency light coupling in a submicrometric silicon-on-insulator waveguide. *Appl. Opt.*, 39(31):5773–5777, November 2000.

[45] G. Roelkens, D. Vermeulen, S. Selvaraja, R. Halir, W. Bogaerts, and D. Van Thourhout. Grating-based optical fiber interfaces for silicon-on-insulator photonic integrated circuits. *IEEE Journal of Selected Topics in Quantum Electronics*, 17(3):571–580, October 2011.

[46] Frederik Van Laere, Gunther Roelkens, Jonathan Schrauwen, Dirk Taillaert, Pieter Dumon, Wim Bogaerts, Dries Van Thourhout, and Roel Baets. Compact grating couplers between optical fibers and silicon-on-insulator photonic wire waveguides with 69 In *Optical Fiber Communication Conference and Exposition and The National Fiber Optic Engineers Conference*, Technical Digest (CD), page PDP15, Anaheim, California, 2006. Optical Society of America.

[47] Wim Bogaerts, Pieter Dumon, Dries Van Thourhout, and Roel Baets. Low-loss, low-cross-talk crossings for silicon-on-insulator nanophotonic waveguides. *Opt. Lett.*, 32(19):2801–2803, October 2007.

[48] D. Vermeulen, S. Selvaraja, P. Verheyen, G. Lepage, W. Bogaerts, P. Absil, D. Van Thourhout, and G. Roelkens. High-efficiency fiber-to-chip grating

couplers realized using an advanced cmos-compatible silicon-on-insulator platform. *Opt. Express*, 18(17):18278–18283, August 2010.

[49] A. G. Rickman, G. T. Reed, and Fereydoon Namavar. Silicon-on-insulator optical rib waveguide loss and mode characteristics. *Journal of Lightwave Technology*, 12(10):1771–1776, August 1994.

[50] M. A. Webster, R. M. Pafchek, G. Sukumaran, and Thomas L. Koch. Low-loss quasi-planar ridge waveguides formed on thin silicon-on-insulator. *Applied Physics Letters*, 87(23):1–3, November 2005.

[51] Wim Bogaerts, Roel Baets, Pieter Dumon, Vincent Wiaux, Stephan Beckx, Dirk Taillaert, Bert Luyssaert, Joris Van Campenhout, Peter Bienstman, and Dries Van Thourhout. Nanophotonic waveguides in silicon-on-insulator fabricated with cmos technology. *Journal of Lightwave Technology*, 23(1):401–412, January 2005.

[52] S. Lardenois, D. Pascal, L. Vivien, E. Cassan, S. Laval, R. Orobtchouk, M. Heitzmann, N. Bouzaida, and L. Mollard. Low-loss submicrometer silicon-on-insulator rib waveguides and corner mirrors. *Optics letters*, 28(13):1150–1152, July 2003.

[53] M. Gnan, S. Thoms, D. S. Macintyre, R. m. D. La Rue, and M. Sorel. Fabrication of low-loss photonic wires in silicon-on-insulator using hydrogen silsesquioxane electron-beam resist. *Electronics Letters*, 44(2):115–116, January 2008.

[54] Kevin K. Lee, Desmond R. Lim, Lionel C. Kimerling, Jangho Shin, and Franco Cerrina. Fabrication of ultralow-loss si/sio 2 waveguides by roughness reduction. *Optics letters*, 26(23):1888–1890, December 2001.

[55] Eli Yablonovitch. Inhibited spontaneous emission in solid-state physics and electronics. *Phys. Rev. Lett.*, 58(20):2059–2062, May 1987.

[56] Sajeev John. Strong localization of photons in certain disordered dielectric superlattices. *Phys. Rev. Lett.*, 58(23):2486–2489, June 1987.

[57] E. M. Purcell. Spontaneous emission probabilities at radio frequencies. *Physical Review*, 69:681, 1946.

[58] Jonathan P. Dowling, Michael Scalora, Mark J. Bloemer, and Charles M. Bowden. The photonic band edge laser: A new approach to gain enhancement. *Journal of Applied Physics*, 75(4):1896, August 1994.

[59] J. OBrien, Oskar Painter, R. Lee, Chuan-Cheng Cheng, A. Scherer, and A. Yariv. Lasers incorporating 2d photonic bandgap mirrors. *Electronics Letters*, 32(24):2243–2244, June 1996.

[60] O. Painter, R. K. Lee, A. Scherer, A. Yariv, J. D. O'Brien, P. D. Dapkus, and I. Kim. Two-dimensional photonic band-gap defect mode laser. *Science*, 284(5421):1819, June 1999.

[61] Attila Mekis, J. C. Chen, I. Kurland, Shanhui Fan, Pierre R. Villeneuve, and J. D. Joannopoulos. High transmission through sharp bends in photonic crystal waveguides. *Phys. Rev. Lett.*, 77(18):3787–3790, October 1996.

[62] Thomas F. Krauss. Why do we need slow light? *Nat Photon*, 2(8):448–450, August 2008.

[63] J. D. Joannopoulos, S. G. Johnson, J. N. Winn, and R. D. Meade. *Photonic Crystals: Molding the Flow of Light, Second Edition*. Princeton University Press, 2008.

[64] Solomon Assefa, Sharee J. McNab, and Yurii A. Vlasov. Transmission of slow light through photonic crystal waveguide bends. *Opt. Lett.*, 31(6):745–747, March 2006.

[65] Philip Trost Kristensen and Stephen Hughes. Modes and mode volumes of leaky optical cavities and plasmonic nanoresonators. *ACS Photonics*, 1(1):2–10, January 2014.

[66] P. N. Lebedev. Experimental examination of light pressure. *Ann. der Physic.*, 6:433, 1901.

[67] Richard A. Beth. Mechanical detection and measurement of the angular momentum of light. *Physical Review*, 50(2):115, July 1936.

[68] A. Ashkin, J. M. Dziedzic, J. E. Bjorkholm, and Steven Chu. Observation of a single-beam gradient force optical trap for dielectric particles. *Opt. Lett.*, 11(5):288–290, May 1986.

[69] K. Dholakia and T. Cizmar. Shaping the future of manipulation. *Nat Photon*, 5(6):335–342, June 2011.

[70] Miles Padgett and Richard Bowman. Tweezers with a twist. *Nat Photon*, 5(6):343–348, June 2011.

[71] Steven M. Block, Lawrence S. B. Goldstein, and Bruce J. Schnapp. Bead movement by single kinesin molecules studied with optical tweezers. *Nature*, 348(6299):348–352, November 1990.

[72] M. E. J. Friese, T. A. Nieminen, N. R. Heckenberg, and H. Rubinsztein-Dunlop. Optical alignment and spinning of laser-trapped microscopic particles. *Nature*, 394(6691):348–350, July 1998.

[73] Elio A. Abbondanzieri, William J. Greenleaf, Joshua W. Shaevitz, Robert Landick, and Steven M. Block. Direct observation of base-pair stepping by rna polymerase. *Nature*, 438(7067):460–465, November 2005.

[74] Euan Mcleod and Craig B. Arnold. Subwavelength direct-write nanopatterning using optically trapped microspheres. *Nat Nano*, 3(7):413–417, July 2008.

[75] Carlos Bustamante, Jed C. Macosko, and Gijs J. L. Wuite. Grabbing the cat by the tail: manipulating molecules one by one. *Nat Rev Mol Cell Biol*, 1(2):130–136, November 2000.

[76] L. Allen, M. W. Beijersbergen, R. J. C. Spreeuw, and J. P. Woerdman. Orbital angular momentum of light and the transformation of laguerre-gaussian laser modes. *Phys. Rev. A*, 45(11):8185–8189, June 1992.

[77] N. B. Simpson, K. Dholakia, L. Allen, and M. J. Padgett. Mechanical equivalence of spin and orbital angular momentum of light: an optical spanner. *Opt. Lett.*, 22(1):52–54, January 1997.

[78] Jennifer E. Curtis, Brian A. Koss, and David G. Grier. Dynamic holographic optical tweezers. *Optics Communications*, 207(1-6):169–175, June 2002.

[79] David G. Grier and Yael Roichman. Holographic optical trapping. *Appl. Opt.*, 45(5):880–887, February 2006.

[80] Steven B. Smith, Yujia Cui, and Carlos Bustamante. Overstretching b-dna: The elastic response of individual double-stranded and single-stranded dna molecules. *Science*, 271(5250):795, February 1996.

[81] Arnau Farre, Astrid van der Horst, Gerhard A. Blab, Benjamin P. B. Downing, and Nancy R. Forde. Stretching single dna molecules to demonstrate high-force capabilities of holographic optical tweezers. *J. Biophoton.*, 3(4):224–233, February 2010.

[82] Miklos S. Z. Kellermayer, Steven B. Smith, Henk L. Granzier, and Carlos Bustamante. Folding-unfolding transitions in single titin molecules characterized with laser tweezers. *Science*, 276(5315):1112, May 1997.

[83] L. Tskhovrebova, J. Trinick, J. A. Sleep, and R. M. Simmons. Elasticity and unfolding of single molecules of the giant muscle protein titin. *Nature*, 387(6630):308–312, May 1997.

[84] Naghmeh Rezaei, Benjamin P. B. Downing, Andrew Wieczorek, Clara K. Y. Chan, Robert Lindsay Welch, and Nancy R. Forde. Using optical tweezers to study mechanical properties of collagen. In *Proc. SPIE*, volume 8007, pages 80070K–80070K–10, 2011.

[85] Jeffrey T. Finer, Robert M. Simmons, and James A. Spudich. Single myosin molecule mechanics: piconewton forces and nanometre steps. *Nature*, 368(6467):113–119, March 1994.

[86] J. Jackson. *Classical electrodynamics*. JOHN WILEY AND SONS (New York), 1962.

[87] Lumerical solutions, inc.

[88] Comsol multiphysics.

[89] L. Novotny and B. Hecht. *Principles of nano-optics*. Cambridge Univeristy Press, 2006.

[90] T. Iida and H. Ishihara. Nano-optical manipulation using resonant radiation force. In *Progress in Nano-Electro-Optics VI: Nano-Optical Probing, Manipulation, Analysis, and Their Theoretical Bases*, pages 115–168. Springer Berlin Heidelberg, Berlin, Heidelberg, 2008.

[91] Stephen M. Barnett. Optical angular-momentum flux. *Journal of Optics B: Quantum and Semiclassical Optics*, 4(2):S7, December 2002.

[92] Yasuhiro Harada and Toshimitsu Asakura. Radiation forces on a dielectric sphere in the rayleigh scattering regime. *Optics Communications*, 124(5):529–541, March 1996.

[93] Onofrio M. Marago, Philip H. Jones, Pietro G. Gucciardi, Giovanni Volpe, and Andrea C. Ferrari. Optical trapping and manipulation of nanostructures. *Nat Nano*, 8(11):807–819, November 2013.

[94] Mathieu L. Juan, Reuven Gordon, Yuanjie Pang, Fatima Eftekhari, and Romain Quidant. Self-induced back-action optical trapping of dielectric nanoparticles. *Nat Phys*, 5(12):915–919, December 2009.

[95] Shiyun Lin and Kenneth B. Crozier. Trapping-assisted sensing of particles and proteins using on-chip optical microcavities. *ACS Nano*, 7(2):1725–1730, February 2013.

[96] Lukas Novotny, Randy X. Bian, and X. Sunney Xie. Theory of nanometric optical tweezers. *Phys. Rev. Lett.*, 79(4):645–648, July 1997.

[97] Maurizio Righini, Anna S. Zelenina, Christian Girard, and Romain Quidant. Parallel and selective trapping in a patterned plasmonic landscape. *Nat Phys*, 3(7):477–480, July 2007.

[98] Yuanjie Pang and Reuven Gordon. Optical trapping of a single protein. *Nano Lett.*, 12(1):402–406, January 2012.

[99] Lina Huang, Sebastian J. Maerkl, and Olivier J. F. Martin. Integration of plasmonic trapping in a microfluidic environment. *Opt. Express*, 17(8):6018–6024, April 2009.

[100] David Erickson, Xavier Serey, Yih-Fan Chen, and Sudeep Mandal. Nanomanipulation using near field photonics. *Lab Chip*, 11(6):995–1009, January 2011.

[101] C. Renaut, J. Dellinger, B. Cluzel, T. Honegger, D. Peyrade, E. Picard, F. de Fornel, and E. Hadji. Assembly of microparticles by optical trapping with a photonic crystal nanocavity. *Appl. Phys. Lett.*, 100(10):101103, March 2012.

[102] C. Renaut, B. Cluzel, J. Dellinger, L. Lalouat, E. Picard, D. Peyrade, E. Hadji, and F. de Fornel. On chip shapeable optical tweezers. *Scientific Reports*, 3:2290, July 2013.

[103] Michael Barth and Oliver Benson. Manipulation of dielectric particles using photonic crystal cavities. *Appl. Phys. Lett.*, 89(25):253114, December 2006.

[104] Adel Rahmani and Patrick C. Chaumet. Optical trapping near a photonic crystal. *Opt. Express*, 14(13):6353–6358, June 2006.

[105] Juejun Hu, Shiyun Lin, Lionel C. Kimerling, and Kenneth Crozier. Optical trapping of dielectric nanoparticles in resonant cavities. *Phys. Rev. A*, 82(5):053819, November 2010.

[106] Nicolas Descharmes, Ulagalandha Perumal Dharanipathy, Zhaolu Diao, Mario Tonin, and Romuald Houdr. Observation of backaction and self-induced trapping in a planar hollow photonic crystal cavity. *Phys. Rev. Lett.*, 110(12):123601, March 2013.

[107] Abhay Kotnala and Reuven Gordon. Double nanohole optical tweezers visualize protein p53 suppressing unzipping of single dna-hairpins. *Biomed. Opt. Express*, 5(6):1886–1894, June 2014.

[108] Shiyun Lin, Juejun Hu, Lionel Kimerling, and Kenneth Crozier. Design of nanoslotted photonic crystal waveguide cavities for single nanoparticle trapping and detection. *Opt. Lett.*, 34(21):3451–3453, November 2009.

[109] M. Tonin, F. M. Mor, L. Forr, S. Jeney, and R. Houdr. Thermal fluctuation analysis of singly optically trapped spheres in hollow photonic crystal cavities. *Appl. Phys. Lett.*, 109(24):241107, December 2016.

[110] Francesco DellOlio and Vittorio M. N. Passaro. Optical sensing by optimized silicon slot waveguides. *Opt. Express*, 15(8):4977–4993, April 2007.

[111] Carlos A. Barrios, Kristinn B. Gylfason, Benito Snchez, Amadeu Griol, H. Sohlstrm, M. Holgado, and R. Casquel. Slot-waveguide biochemical sensor. *Opt. Lett.*, 32(21):3080–3082, November 2007.

[112] Jacob T. Robinson, Christina Manolatou, Long Chen, and Michal Lipson. Ultrasmall mode volumes in dielectric optical microcavities. *Phys. Rev. Lett.*, 95(14):143901, September 2005.

[113] Takayuki Yamamoto, Masaya Notomi, Hideaki Taniyama, Eiichi Kuramochi, Yutaka Yoshikawa, Yoshio Torii, and Takahiro Kuga. Design of a high-q air-slot cavity based on a width-modulated line-defect in a photonic crystal slab. *Opt. Express*, 16(18):13809–13817, September 2008.

[114] A. Di Falco, L. OFaolain, and T. F. Krauss. Chemical sensing in slotted photonic crystal heterostructure cavities. *Applied Physics Letters*, 94(6):063503, February 2009.

[115] Jie Gao, James F. McMillan, Ming-Chung Wu, Jiangjun Zheng, Solomon Assefa, and Chee Wei Wong. Demonstration of an air-slot mode-gap confined photonic crystal slab nanocavity with ultrasmall mode volumes. *Applied Physics Letters*, 96(5):051123, February 2010.

[116] Eiji Miyai and Susumu Noda. Structural dependence of coupling between a two-dimensional photonic crystal waveguide and a wire waveguide. *J. Opt. Soc. Am. B*, 21(1):67–72, January 2004.

[117] Z. Wang, N. Zhu, Y. Tang, L. Wosinski, D. Dai, and S. He. Ultracompact low-loss coupler between strip and slot waveguides. *Optics letters*, 34(10):1498–1500, May 2009.

[118] Robert Palmer, Luca Alloatti, Dietmar Korn, Wolfgang Heni, Philipp Schindler, Jens Bolten, Matthias Karl, Michael Waldow, Thorsten Wahlbrink, Wolfgang Freude, Christian Koos, and Juerg Leuthold. Highly efficient strip-to-slot mode converters. In *Conference on Lasers and Electro-Optics 2012*, OSA Technical Digest (online), page CM4M.1, San Jose, California, 2012. Optical Society of America.

[119] J. Blasco and C. A. Barrios. Compact slot-waveguide/channel-waveguide mode-converter. In *CLEO/Europe. 2005 Conference on Lasers and Electro-Optics Europe, 2005.*, pages 607–607, 2005.

[120] N. N. Feng, R. Sun, L. C. Kimerling, and J. Michel. Lossless strip-to-slot waveguide transformer. *Optics letters*, 32(10):1250–1252, May 2007.

[121] Yun Wang, Jonas Flueckiger, Charlie Lin, and Lukas Chrostowski. Universal grating coupler design. *Proc. SPIE*, 8915:89150Y–89150Y–7, October 2013.

[122] Yun Wang, Xu Wang, Jonas Flueckiger, Han Yun, Wei Shi, Richard Bojko, Nicolas A. F. Jaeger, and Lukas Chrostowski. Focusing sub-wavelength grating couplers with low back reflections for rapid prototyping of silicon photonic circuits. *Opt. Express*, 22(17):20652–20662, August 2014.

[123] Labview system design software.

[124] M. G. Scullion, A. Di Falco, and T. F. Krauss. Slotted photonic crystal cavities with integrated microfluidics for biosensing applications. *Biosensors and Bioelectronics*, 27(1):101–105, September 2011.

[125] Ian M. White and Xudong Fan. On the performance quantification of resonant refractive index sensors. *Opt. Express*, 16(2):1020–1028, January 2008.

[126] Bowen Wang, Mehmet A. Dndar, Richard Ntzel, Fouad Karouta, Sailing He, and Rob W. van der Heijden. Photonic crystal slot nanobeam slow light

waveguides for refractive index sensing. *Applied Physics Letters*, 97(15):151105, October 2010.

[127] E. Chow, A. Grot, L. W. Mirkarimi, M. Sigalas, and G. Girolami. Ultracompact biochemical sensor built with two-dimensional photonic crystal microcavity. *Opt. Lett.*, 29(10):1093–1095, May 2004.

[128] Wei-Cheng Lai, Swapnajit Chakravarty, Yi Zou, and Ray T. Chen. Silicon nano-membrane based photonic crystal microcavities for high sensitivity bio-sensing. *Opt. Lett.*, 37(7):1208–1210, April 2012.

[129] Kaiyuan Yao and Yaocheng Shi. High-q width modulated photonic crystal stack mode-gap cavity and its application to refractive index sensing. *Opt. Express*, 20(24):27039–27044, November 2012.

[130] Nanocomposix, inc.

[131] S. Arnold, M. Khoshsima, I. Teraoka, S. Holler, and F. Vollmer. Shift of whispering-gallery modes in microspheres by protein adsorption. *Opt. Lett.*, 28(4):272–274, February 2003.

[132] E.-L. Florin, A. Pralle, E. H. K. Stelzer, and J. K. H. Hrber. Photonic force microscope calibration by thermal noise analysis. *Applied Physics A*, 66(1):S75–S78, March 1998.

[133] N. D. Gagunashvili. Chi-square tests for comparing weighted histograms. *Nuclear Instruments and Methods in Physics Research Section A: Accelerators, Spectrometers, Detectors and Associated Equipment*, 614(2):287–296, March 2010.

[134] A. Ashkin. Acceleration and trapping of particles by radiation pressure. *Phys. Rev. Lett.*, 24:156, January 1970.

[135] A. Ashkin, J. M. Dziedzic, and T. Yamane. Optical trapping and manipulation of single cells using infrared-laser beams. *Nature*, 330:769, December 1987.

[136] A. Ashkin and J. M. Dziedzic. Optical trapping and manipulation of viruses and bacteria. *Science*, 235:1517, March 1987.

[137] R. D. Miller and T. B. Jones. Electro-orientation of ellipsoidal erythrocytes–theory and experiment. *Biophys. J.*, 64:1588, May 1993.

[138] M. E. J. Friese, J. Enger, H. Rubinsztein-Dunlop, and N. R. Heckenberg. Optical angular-momentum transfer to trapped absorbing particles. *Phys. Rev. A*, 54:1593, August 1996.

[139] Pilgyu Kang, Xavier Serey, Yih-Fan Chen, and David Erickson. Angular orientation of nanorods using nanophotonic tweezers. *Nano Lett.*, 12(12):6400–6407, December 2012.

[140] M. Washizu, M. Shikida, S. i. Aizawa, and H. Hotani. Orientation and transformation of flagella in electrostatic field. *IEEE Transactions on Industry Applications*, 28(5):1194–1202, August 1992.

[141] Idah C. Pekcevik, Lester C. H. Poon, Michael C. P. Wang, and Byron D. Gates. Tunable loading of single-stranded dna on gold nanorods through the displacement of polyvinylpyrrolidone. *Anal. Chem.*, 85(20):9960–9967, October 2013.